NONLINEAR THERMO-ELECTRO-MECHANICAL BEHAVIORS OF AG/BATIO$_3$ COMPOSITES

A Dissertation

by

JUNWEI XING

Submitted to the Office of Graduate and Professional Studies of
Texas A&M University
in partial fulfillment of the requirements for the degree of

DOCTOR OF PHILOSOPHY

Chair of Committee,	Anastasia Muliana
Co-Chair of Committee,	Miladin Radovic
Committee Members,	Tahir Cagin
	Sevan Goenezen
Head of Department,	Andreas Polycarpou

December 2016

Major Subject: Mechanical Engineering

ABSTRACT

The focus of this study is to understand the influences of blending silver (Ag) phase into barium titanate ($BaTiO_3$) ceramic on its thermal, mechanical and dielectric properties. Silver-barium titanate ($Ag/BaTiO_3$) active composites with varying silver composition were fabricated using powder metallurgy method. Coefficient of thermal expansion (CTE) and heat capacity were measured by thermal mechanical analyzer (TMA) and differential scanning calorimetry (DSC), respectively. Hot disk technique was employed to determine the thermal conductivity. Addition of silver did not change the phase transformation temperatures. CTE stays constant at each crystalline phase, but increases as $BaTiO_3$'s crystal structure changes from orthorhombic to tetragonal phase and further to cubic. Increase of silver content significantly enhances the thermal conductivity. Elastic and dielectric constants were determined using resonant ultrasound spectroscopy (RUS) and dielectric (impedance) spectroscopy, respectively. Young's modulus decreases as the increase of silver composition, while the dielectric constant was significantly improved by blending silver. Two peaks were observed on dielectric constant around the transformation temperatures, with a larger magnitude at the Curie point.

Micromechanics models based on detailed microstructures, either generated randomly by computer algorithm or created by converting scanning electron microscope (SEM) images, were created to numerically study the effects of microstructures on the effective properties of $Ag/BaTiO_3$ composite. Numerical results showed that microstructure induced anisotropy is negligible and the effective properties are insensitive to loading directions. Effective CTE is insensitive to the yielding of silver particles, porosity, and the elastic modulus of $BaTiO_3$. The predictions of CTE and elastic constants were pretty close to the experiment results, while the effective thermal conductivity and dielectric constant predictions underestimated the measured values.

The hysteretic mechanical behavior of $Ag/BaTiO_3$ composite was measured under cyclic uniaxial compressive loading using materials test system (MTS). Specimens with 5 vol% and 13 vol% silver composition were broken before the maximum stress was reached. The fractured specimens showed a fracture angle of approximate 45 ^{o}C. Furthermore, a one-dimensional constitutive model based on the thermodynamics of irreversible process was presented to model the hysteretic response from experiment.

DEDICATION

To my parents

ACKNOWLEDGEMENTS

I would like to thank my advisors Dr. Muliana and Dr. Radovic for their continuous help and support for the last five years in my study and research. Without their patient and knowledgeable guidance this dissertation would have not been possible.

My great appreciation also extends to my committee members Professor Cagin and Professor Goenezen for serving in my committee and for their insightful comments and suggestions. I would also like to thank Texas A&M Supercomputing Facility for providing computing resources useful in conducting this research.

Many thanks to Pradeep Gudlur, Liangfa Hu, Ankush Kothalkar, Frank Gardea, and Dr. Brankovic for training and helping me to use various testing equipment. Without their help many of the measurements in this work would be, if possible, delayed. Thanks also go to my friends and colleagues in the research group and in Texas A&M University, who made my stay and study more enjoyable. My gratitude also goes to the faculty and staff in Mechanical Engineering Department for making my time at Texas A&M University a great experience.

Most of all, I would like to express my deepest gratitude to my family for their understanding, continuous encouragement, and love for all these years. Thank you that you have always been there.

NOMENCLATURE

2D	Two Dimensional
3D	Three Dimensional
4PB	Four Point Bending
Ag	Silver
$BaTiO_3$	Barium Titanate
$Ag/BaTiO_3$	Silver-Barium Titanate Composite
BC	Boundary Condition
CIP	Cold Isostatic Pressing
CSM	Combined Sintering Method
CTE	Coefficient of Thermal Expansion
DSC	Differential Scanning Calorimetry
EDS	Energy Dispersive X-ray Spectroscopy
FE	Finite Element
HPS	High-Pressure Sintering
IC	Integrated Circuit
IE	Impulse Excitation
MLCC	Multilayer Ceramic Capacitor
MTS	Materials Test System
NI	Nanoindentation
OOF	Object Oriented Finite Element Method

PZT	Lead Zirconate Titanate
RCS	Rate-Controlled Sintering
RMS	Root Mean Sqaure
RUS	Resonant Ultrasound Spectroscopy
RVE	Representative Volume Element
SEM	Scanning Electron Microscope
SPS	Spark Plasma Sintering
TMA	Thermal Mechanical Analyzer
VF	Volume Fraction
XRD	X-Ray Diffraction

TABLE OF CONTENTS

Page

LIST OF FIGURES

Page

LIST OF TABLES

CHAPTER I

INTRODUCTION AND LITERATURE REVIEW

1.1 Problem statement

Barium titanate ($BaTiO_3$) based ceramics have found many applications in electronic industry like multilayer ceramic capacitors (MLCCs) because of its relatively high dielectric constants [1-3]. They are also preferred for actuator and sensor applications because they do not contain lead as some other piezoelectric ceramics [4, 5]. Due to the large heat generation during cycling service, good thermal management is a key issue for the integrity and reliability of such devices. However, $BaTiO_3$ is extremely brittle which greatly impedes its further applications. Furthermore, lack of enough ductility and fracture resistance also reduces the performance and reliability of devices made of $BaTiO_3$ ceramics. In order to improve the durability of $BaTiO_3$ ceramic based devices under harsh environment, metal phase were doped in $BaTiO_3$ matrix in order to fabricate ceramic/metal composite [6-12]. The benefits of adding metal phase are multiple. Firstly, it provides a possibility to engineer the properties of the composites by controlling the volume fraction of metal phase. Secondly, the mechanical properties, such as fracture strength and fracture toughness, of the composite containing metallic phase were greatly enhanced. Thirdly, the introduction of metal phase into $BaTiO_3$ ceramics also can significantly increase its dielectric constants, which is beneficial to the miniaturization of MLCC [1].

In this study, a specific metal/$BaTiO_3$ composite, i.e. silver-barium titanate (Ag/$BaTiO_3$) composite, was fabricated and investigated. The reason for using silver as the blending metal phase is that it would not react with $BaTiO_3$. In addition, since the sinter temperature are very high, the metal phase is not expected to get oxidized during the sintering process. Silver is preferred candidate in this respect because silver oxide would deoxidized above certain elevated temperature. After fabrication and microstructural characterization, various thermal, mechanical and dielectric properties of Ag/$BaTiO_3$ composite were examined both experimentally and numerically. The influences of silver composition on the effective properties of the composite were investigated

1.2 Objectives

The objective of this study is to fabricate, characterize and model Ag/$BaTiO_3$ composite. Both experimental techniques and numerical analysis were employed to investigate the influences of blending silver phase into barium titanate on the various effective properties of the composite. The specific research objectives are:

1. Fabricate Ag/$BaTiO_3$ composite with varying silver composition using powder metallurgy method and characterize its microstructural profiles, existing phases, density and porosity.
2. Experimentally measure various thermal, mechanical and dielectric properties of Ag/$BaTiO_3$ composite, such as CTE, thermal conductivity, thermal diffusivity, heat capacity, Young's modulus, Poisson's ratio, relative permittivity and dielectric loss.

3. Build micromechanics models to numerically investigate the effects of microstructures and predict the various effective thermal, mechanical and dielectric properties of Ag/$BaTiO_3$ composite.
4. Experimentally test the ferroelastic hysteric response of Ag/$BaTiO_3$ composite and develop constitutive model to numerically simulate such nonlinear behavior.

1.3 Literature review

1.3.1 Crystalline structure

Barium titanate has a perovskite type crystalline structures which is adopted by many oxides with the chemical formula ABO_3 [13, 14]. The larger cation Ba is located in the corner, while the smaller cation Ti and the anion O are located in the middle of the cube and at the center of faces, respectively [15]. The coordination number for cation Ba is 12, while 6 for cation Ti [16]. Three phase transformations exist for $BaTiO_3$. The Curie temperature T_c for $BaTiO_3$ is around 120 ^{o}C [17]. Above the Currie temperature the perovskite crystalline structure is cubic with a side length a_0 where the center of the positive and negative charges coincide. Consequently, in cubic state $BaTiO_3$ exhibits no spontaneous polarization and is no polar. As a result, piezoelectricity effect cannot be observed, and only electrostriction might happen. The cubic phase is also called paraelectric phase. Above 120 ^{o}C the cubic phase is stable up to 1460 ^{o}C above which a hexagonal structure is stable [18]. Below its Currie temperature, the cubic structure becomes unstable and $BaTiO_3$ undergoes a phase transformation to a tetragonal phase with side lengths $a \times a \times c$. During this phase transformation the cubic structure is elongated in on direction and contracted in the other two directions. The ratio of elongated and contracted side lengths at room temperature is roughly [17]

$$\frac{c-a}{a} \approx 1\% \tag{1.1}$$

In tetragonal phase, the center of positive and negative charges no longer coincide. As a result, spontaneous polarization was formed in the unit cell. This phase is also called ferroelectric phase and piezoelectricity can be observed. Upon further cooling $BaTiO_3$ under around 0 ^{o}C another phase transformation occurs at which the crystalline structure changes to orthorhombic [17, 19-21]. The orthorhombic phase exhibits polarization and is ferroelectric. The third phase transformation happens around -90 ^{o}C where the orthorhombic structure becomes unstable and changes to a rhombohedral structure [18].

The spontaneous polarization in tetragonal phase can be switched or rotated to the directions opposite or perpendicular to its original direction by either electric field or mechanical stress. Upon the application of electric field opposite to the original polarization direction an 180^{o} switching will happen, while it experiences a 90^{o} reorientation for an electrical loading perpendicular to the original polarization direction [17]. Furthermore, the 90^{o} polarization switching direction coincides with the electrical loading direction. On the contrary, mechanical loadings can only induce 90^{o} polarization switching [22]. When a compressive mechanical stress is applied parallel to the spontaneous polarization it reoriented to the plane perpendicular to the loading direction. No specific direction on this plane is preferred during this process. On the other hand, a tensile mechanical stress perpendicular to the spontaneous polarization will randomly switch it to the two directions parallel with the loading direction.

Bulk $BaTiO_3$ ceramic is fabricated by sintering at high temperature far above the Curie temperature. During the sintering process when cooling down to below the Curie temperature the cubic crystal structure changes to tetragonal with the spontaneous polarization direction randomly distributed [17]. As a result, the bulk material exhibits no net polarization. Within each grain there are subregions of unit cells with equally oriented spontaneous polarization directions, which are called domains. The interfaces between domains with antiparallel polarization directions are called 180^o domain wall, while called 90^o domain wall for those with perpendicular polarization directions. To introduce piezoelectricity to the bulk $BaTiO_3$ ceramics an electric filed above certain threshold (coercive electric filed) is applied to reorient the spontaneous directions, which is the poling process [23]. The poling usually is carried out at temperatures slightly above the Curie temperature, for the dipoles are easier to be reoriented [23]. After poling bulk ceramic exhibits net polarizations and piezoelectricity.

1.3.2 Specimen fabrication

Several sintering techniques have been considered to obtain bulk and dense $BaTiO_3$ ceramics with desired microstructures. The most widely used technique is the conventional powder metallurgy method [17], which is a relatively easy and inexpensive way to produce bulk ceramics with good density. The disadvantage of this method is that it is difficult to control the grain size, which significantly influences the macroscopic properties of $BaTiO_3$, especially its dielectric properties [24]. This is due to the relative slow heating rate (2~15 ^oC/min) during the sintering. Before finally reaching the sintering temperatures (~1250 °C) several hours have already been spent which suffices for significant particle coarsening by surface diffusion [25]. As a result, partial densification of nanocrystalline powders may be resulted from conventional sintering techniques [26-30]. To inhibit the coarsening of nanoparticles during sintering a faster heating rate was used in [31, 32] based on the rate equation of densification and grain growth. Other sintering methods used in literature include rate-controlled sintering (RCS) [33-37], high-pressure sintering (HPS) [38-42], and combined sintering method (CSM) [43, 44]. The effects of these sintering techniques were investigated in [45] to fabricate barium titanate ceramics with nano grain size. Fully densified ceramic (99.9%) with an average grain size of 350 nm was obtained by rate-controlled sintering. The grain boundary is clean and perfect. The relative density of the samples fabricated by high-pressure sintering is around 95%, with a mean grain size of 60 nm. However, deviation from stoichiometry in oxygen sublattice of $BaTiO_3$ was observed, which is evidenced by the dark color of the samples. Nanocrystalline ceramic with relative density of 98.6% and mean grain size of 90 nm was fabricated by combined sintering method.

In another approach to overcome the drawback of conventional sintering, Chen and Wang [46] introduced a novel two-step sintering technique, in which the mechanisms of grain boundary controlled densification and grain boundary controlled grain growth were exploited to suppress the rapid grain growth in the final stage of sintering [47-50]. Several authors successfully utilized this technique to fabricate dense $BaTiO_3$ ceramics with nano grain size [5, 51-53]. Fully dense barium titanate ceramic with average grain size of 108 nm was fabricated by using two-step sintering technique under controlled atmosphere [52]. Very slow grain growth factor, i.e. 3.5, was observed, which is three and 17 times smaller than rate-controlled and conventional sintering methods, respectively. By suppressing grain growth in the final stage of densification in two-step sintering, high density (>96%) with unprecedentedly fine grain size (35 nm) barium titanate ceramic was sintered in [53]. The densification temperature was as low as 900 ^oC, which is much lower than conventional sintering techniques. Distortions from cubic to various low-temperature ferroelectric structures were observed for dense $BaTiO_3$ ceramic with a grain size of 35 nm. Large dielectric constants and good piezoelectric properties were reported for $BaTiO_3$ ceramic with a relative density of 98% and average grain size of 1.6 μm in [5, 51]. The Curie and orthorhombic to tetragonal phase transformation temperatures were found to be 126 and 24 ^oC, respectively.

Another method to obtain dense $BaTiO_3$ ceramic with small grain size is spark plasma sintering (SPS) [54-58]. Spark plasma sintering combines hot-pressing and electrical current. Compared with the conventional sintering, in SPS process the powder can be sintered at a lower temperature and in a much shorter sintering time, which is favorable for suppressing the undesired grain growth [59-61]. 36 nm $BaTiO_3$ particles was used in [62] to sinter 97% dense ceramic with 50nm grain size. The specimen was sintered at 50 MPa and 820 ^oC for 3 min with a heating rate of 200 ^oC/min. Li et al. [63, 64] studied the effects of different sintering conditions on the microstructure of SPS sintered $BaTiO_3$ specimens. The heating rate ranged from 50 to 400 ^oC/min while the pressure from 20 to 40 MPa. The as-sintered pellets were annealed in air at 900 ^oC for 2 h to remove the carbon contamination. It was found the final grain size of ~ 300 nm in the samples sintered for 1 min at 40 MPa and 920 ^{o}C was not affected by the heating rate between 50 and 250 ^{o}C/min. Increasing the heating rate to 400 ^{o}C/min, however, led to finer grain size of 250 nm. It was also found that partially dense specimens with nano grain size of smaller than 50 nm were sintered at temperature below 1050 ^{o}C, while sub-micrometer grain size obtained above 1050 ^{o}C. Various properties, such as phase transition, Curie temperature, heat of transition, and dielectric properties, of SPS sintered $BaTiO_3$ ceramics were examined in [64-66].

1.3.3 Effects of blending metal phase

Metal phase doped ferroelectric ceramics, such as $BaTiO_3$ and lead zirconate titanate (PZT), were extensively studied by researchers. The doping of metal phase can lower the starting temperature of densification and enhance the densification rate. The improved densification of silver doped $BaTiO_3$ ceramic has been attributed to the dissolution of Ag into the ceramic matrix, which either increases the defect concentration or decrease the formation temperature of liquid phase [7, 10]. However, it was shown that the solubility of Ag in $BaTiO_3$ ceramic is limited [9, 67]. The introduction of Ag phase decreases the relative density compared to the monolithic ceramic, because Ag phase inclusions increase the inter-diffusion distance between $BaTiO_3$ grains and thus reduce the connectivity of $BaTiO_3$ particles [7, 10]. However, small amount of silver would increase the relative density, since they can fill the pores within the ceramic [68]. Since the sintering temperature is well above the melting temperature of silver, Ag phase could evaporate near the surface of the sample, which reduces its relative density and changes the color of the surface [67]. Ceramic grain size was reduced by the increase of silver content, while the size of silver inclusion was increased [9, 10, 69]. This has significant implication on its dielectric property because it depends strongly on the grain size [24]. It was reported the Curie temperature would decrease as silver content increase due to the substitution of silver in A-site of the perovskite crystal structure [6, 70]. However, as reported in [71], the addition of silver increases the Curie temperature of PZT. They attribute it to the relaxation of transformation-induced internal stress due to silver phases. Since silver is much softer than $BaTiO_3$ the hardness and stiffness are reduced by adding silver phase [10]. Silver particles are located either at $BaTiO_3$ grain boundary junctions or within individual $BaTiO_3$ grains [7, 10]. They can increase the toughness of the ceramic by crack bridging or crack deflection mechanisms [10, 69]. On the other hand, addition of silver phase may introduce more defects and pores, which reduces the fracture toughness. It was reported that when silver content is low the toughness enhancement mechanism would overweigh the effect of porosity, while high silver content usually decrease the fracture toughness [7]. Fracture strength can also be improved due to the increase of fracture toughness. Silver inclusion in the ceramic will form conductive phase and increase electric field intensity, which significantly increases its dielectric constants [6, 11, 72].

1.3.4 Thermal, mechanical and dielectric properties

In general, two main categories of experiment techniques exist in literature to measure the thermal conductivity of materials, i.e. steady state techniques and transient techniques. Steady state techniques include the radial heat flow method and the guarded hotplate method [73], while transient methods include the hot wire, laser flash [73], 3ω method [74, 75], the differential photoacoustic method [76], the thermal-wave technique [77], and so on. One advantage of transient technique is that the measurement of thermal conductivity is rapid. The thermal properties of monolithic $BaTiO_3$ ceramics have been studied in several literatures [78-81]. The specific heat and coefficient of thermal expansion (CTE) measured in Sawada et al. [78] were conducted between room temperature and 250 °C to include the Curie temperature. Anomalies were observed around phase transformation temperature. λ-type anomalies exists at the Curie temperature for heat capacity, while contraction in the transition region and a negative peak at the Curie temperature were found for thermal expansion coefficient. In another test conducted in [79] the measurement temperature was selected to lie within -120 °C to 150 °C. Three phase transformations, at -73 °C, at 16 °C, and at 127 °C, were identified, and the transition energies and volume changes at these transitions were calculated. Abnormal peaks at all the phase transformation temperatures were observed with the largest magnitude happened at the Curie temperature. Heat capacity, CTE and thermal conductivity and diffusivity of two different $BaTiO_3$-based ceramic materials were measured in [81] by using differential scanning calorimetry (DSC), thermomechanical analysis (TMA), and hot disk technique. However, anomalies were not observed at the phase transition temperature from orthorhombic to tetragonal, which was ascribed to the addition of dopants and modified microstructures that extended the stability range of the tetragonal phase. In literatures limited studies are available on the influence of silver reinforcement on the thermal properties of the composites.

Techniques to measure the elastic properties of materials also can be classified into two categories: static techniques and dynamics techniques. A detailed comparison of dynamic methods (resonant ultrasound spectroscopy (RUS) and impulse excitation (IE)) to static methods (nanoindentation (NI) and four-point bending (4PB)) were reported in [82]. Compared to NI and 4PB superior precision and repeatability were observed for RUS and IE. Using resonant method the elastic constants of poled polycrystal barium titanate ceramic was measured in [83]. In the test, by piezoelectrically exciting length extensional modes of small bars and contour extensional modes of square and circular plates a series of resonant frequencies of the material was recorded. Mechanical resonance and antiresonance frequencies were measured in [84] to obtain the elastic constants of barium titanate single crystal. Measurements shown that longitudinal compliance in orthorhombic state is much larger than that in tetragonal state which substantially deviated from cubic symmetry. However, experiment data on the elastic properties of unpoled barium titanate ceramic were rarely published in literature. To obtained the elastic constants of unpoled barium titanate ceramic various numerical methods were put forward based on some directional average of the single crystal elastic constants, such as self-consistent effective medium method [85, 86] and micromechanical finite element (FE) method [87, 88]. Furthermore, elastic constants of unpoled ceramics can also be calculated from those of poled polycrystal ceramics [89].

Dielectric constants at room and Curie temperature were reported in [90-97] for $BaTiO_3$ ceramics fabricated with different synthesis route. The experimental measurements show great scattering where values range from 950 to 1740 [23, 24] with a typical value of 1500 [72]. Dielectric properties are significantly influenced by its microstructures, such as defects, purity, density, and grain size [24, 98]. Zhao et al. [66] investigated the grain size effect on the dielectric constants of SPS sintered $BaTiO_3$ ceramics. They found, in contrast to coarse grain ceramics, the dielectric constant of nanocrystalline samples is remarkably less sensitive to temperature. Furthermore, the permittivity peak was significantly broadened and rounded, and the dielectric losses are very small in the whole frequency range. Barium titanate ceramic with grain size range from 0.86 to 10 μm was sintered in [99] by using powder synthesized by Pechini process. It was found that at most of the studied temperature the dielectric constants increased as the decrease of grain size and that specimens with grain size of 0.86 μm exhibited the highest dielectric constant. Dielectric constants as high as 5000 was measured in [51] for two-step sintered $BaTiO_3$ ceramics with an average grain size of 1.6 μm. Dielectric properties of silver reinforced barium titanate composite were studied in [72] which shows that the increase of relative permittivity by adding silver content can be best described by a power law function. Ren et al. [100] shown that addition of silver in $BaTiO_3$ ceramic with a composition lower than 10 mol% can increase its dielectric permittivity, improve the temperature stability and decrease the dielectric loss and dc conductivity.

1.3.5 Micromechanics models

Many micromechanics methods have been put forward to predict the effective properties of composite materials, which, in general, falls into two main categories [101]. The first kind of methods assumes ideally geometry of the reinforcement phases such that the micro stress or strain field can be analytically calculated, from which the effective properties can be obtained [102-104]. For example, an early development of micromechanics models for effective CTE and thermal conductivity (K_{eff}) considers idealized microstructures, such as spherical or ellipsoidal inclusions dispersed in homogeneous matrix, linear thermo-elastic behaviors of the constituents, perfect bonding at the interfaces, etc. Based on such simplifications analytical formulas can be derived for the effective CTE and K_{eff}, for example [105-109] for CTE and [110-116] for K_{eff}. The effect of thermal barrier at phase boundaries was considered in [117, 118].

Another type of micromechanics models were based on detailed microstructures of the composite. The detailed microstructures can either be randomly generated by computer algorithms [119-122], or obtained from the experiments using SEM [123-129]. Finite element (FE) methods are often employed to solve a boundary value problem, from which the effective properties can be calculated. Advantages of such model are nonlinear constituents and complex reinforcement shapes can be easily incorporated. It can simulate the detailed local field fluctuations, such as thermal residual stresses, stress concentrations, and heat flux path. However, to accurately represent the phase boundaries very fine finite element meshes are need, which make it computationally expensive. The micromechanics model developed in [130-134], though assuming simplified geometries, can be applied to composites consisting of nonlinear constituent with field dependent material properties.

With respect to the predictions of effective thermal conductivity, when the reinforcement volume fraction and the ratio of thermal conductivity of the particles to the matrix are relatively small the above micromechanics model can give reasonable predictions of K_{eff}. However, as the volume fraction of reinforcement and differences between the properties of the constituents increase significant mismatches in micromechanics predictions and experiments were observed as shown by [133]. This is due to the formation of thermal conductivity chains by the reinforcement particles with high thermal conductivity [135-137]. Heat can flow following such high conductivity chains much easier compared to other parts of the composites, which significantly increases the effective thermal conductivity [138]. Since the mathematical description of dielectric problem has the same form as that for steady state heat transfer problem [139], plus that the metal phase is conductive, the effective dielectric constants of metal reinforced composite would also be underestimated by the above micromechanics models. An empirical model based on self-consistent theory is proposed in [140] to predict the effective dielectric constant of polymer-ceramic composite. Bergman et al. [141] developed a Fourier expansion method to estimate the bulk effective dielectric constant of a two-component composite with periodic structure. They claim high precision predictions can be obtained even for high material contrast and large reinforcement volume fraction.

1.3.6 Nonlinear hysteresis behavior

There have been several experimental studies on understanding responses of ferroelectric ceramics under compressive stresses. Subbarao et al. [142] observed a strong anelastic effect in $BaTiO_3$ ceramic that leads to permanent strain below Curie temperature and they associated it to the domain reorientation. Such permanent strain is absent above the Curie temperature. Munoz-Saldana et al. [143] investigated the lateral domain wall motion in unpoled $BaTiO_3$ single crystal under compressive unidirectional mechanical stress. The deformation was explained by the 90° domain switching from *a*- to *c*-domains by measuring a compressive stress versus domain width curve. It was found that under compressive loading domain switching in hard PZT appears at higher stress level than in soft PZT [144]. The deformations of piezoelectric ceramics under compression and tension are not the same, because the available dipoles that can be reoriented are different under compression and under tension [145-147]. By simulating the behavior of 100000 crystalline unit cells with randomly distributed initial polar axis orientation it was shown that the maximum remnant strain under tension is slightly larger than the one under compression [148]. The Poisson ratio was found to be of 0.5 during loading period leading to large remnant strain [149], which indicates such deformation is volume preserving. This also confirms that such macroscopic irreversible deformation is due to the microscopic domain wall movement.

The hysteric response of ferroelectric/ferroelastic material under mechanical and electrical loading has been modeled using different approaches, such as thermodynamically consistent models, micromechanical models, and phenomenological models using hysteresis operators. The decomposition of free energy into reversible and irreversible parts was first proposed by Bassiouny et al. [150-153]. The reversible part represents the energy stored in the material, while the irreversible part characterizes the energy dissipation. Adopting this idea Landis developed a general fully coupled, multi-axial constitutive model by assuming a specific form of the Helmholtz free energy [154]. The remnant strain and polarization were used as the internal state variables and the corresponding driving forces were identified to ensure nonnegative energy dissipation. This model was simplified in [155] by assuming that the remnant strain is a quadratic function of the remnant polarization. One drawback of such simplification is that the influence of mechanical loading on the formation of remnant strain cannot be directly incorporated. To explicitly distinguish the effects of electrical and mechanical loadings in [156] the remnant strain was further decomposed into two parts; one part assumed to be functional dependent of the remnant strain and the other part induced by mechanical stress. There have been micromechanical constitutive models formulated for polarization switching responses in which the development of remnant strain and polarization was governed by the transformation of crystal invariant [157, 158]. In the model developed in [157] a local coordinate system was defined for each domain and the domain pattern was described by an orientation distribution function, which was further simplified by Reuss average. Huber et al. [158] envisaged that the polycrystal material consists of a set of bonded crystals and each crystal was characterized by a set of crystal invariants. The development of remnant strain and polarization was governed by the transformation of crystal invariant from one to another. Preisach mathematical function, which is suitable for capturing hysteretic responses, has been used to model the ferroelectric hysteretic responses, for example [159-161]. In these models the Preisach operator was directly used to model the relations between the output strain and electric displacement and the input stress and electric field.

CHAPTER II

FABRICATION AND CHARACTERIZATION*

2.1 Fabrication of Ag/BaTiO$_3$ composite samples

Powder metallurgy method was used to prepare Ag/BaTiO$_3$ composite samples. 99.95% pure BaTiO$_3$ powder (Inframat Advanced Materials) with an average particle size of 100 nm and 99.9% pure silver power (Alfa Aesar) with an average 4-7μm particle size were used as starting powders. Two different fabrication procedures were employed to manufacture samples for various testing. For thermal expansion and heat capacity testing samples (procedure A), 0.5 wt% of polyvinyl alcohol binder was added to the Ag/BaTiO$_3$ powder mixture to avoid cracking during cold-pressing. To uniformly mix the binder with Ag/BaTiO$_3$ powder, polyvinyl alcohol was first dissolved into distilled water, then added to Ag/BaTiO$_3$ powder mixture that was subsequently ball-milled for 30 min. The ball-milled powder was dried in a heating oven and further grinded in a mortar. The final powder was poured into a cylindrical die of 1/2 inch in diameter and a hydraulic press was used to cold-press the powders at room temperature under a pressure of 100 MPa. The binder was burned out at 600 ^{o}C for 2 hours. For thermal conductivity, elastic and dielectric properties testing samples (procedure B), firstly the mixture of Ag/BaTiO$_3$ powder was shaped by cold-pressing at 20 MPa using a split sleeve pressing die (Across International) of 1 inch in diameter. Secondly, the shaped cylindrical body was pressed

---

* Reprinted from Composites Part B: Engineering, 90, Xing J, Radovic M, Muliana A, Thermal properties of BaTiO$_3$/Ag composites at different temperatures, 287-301, Copyright (2016), with permission from Elsevier.

under hydrostatic pressure using cold isostatic pressing (CIP, American Isostatic Presses, Inc.) with a pressure of 200 MPa. The cold-pressed cylindrical green bodies were sintered at 1250 ^{o}C for 6 hours in air atmosphere. The heating/cooling rates were 3 ^{o}C/min.

2.2 Phase composition and microstructural characterization

SEM images of typical Ag/$BaTiO_3$ composite samples with 10 vol% silver are shown in Figure 2.1. It is clear that the silver particles are randomly distributed within the barium titanate matrix for both samples made from different procedures. Furthermore, the particle shapes are irregular and the particle sizes are comparable. Consequently, it is safe to conclude that the microstructures of the samples made from procedure A and procedure B are comparable.

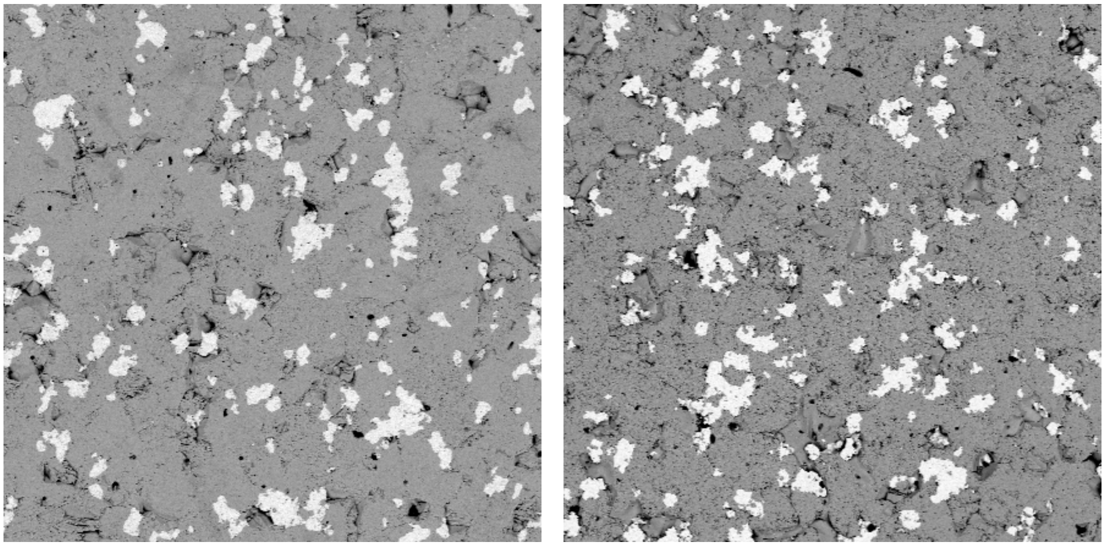

Figure 2.1 SEM images of typical 10 vol% Ag/$BaTiO_3$ composite samples from different fabrication procedures: left, procedure A; right, procedure B.

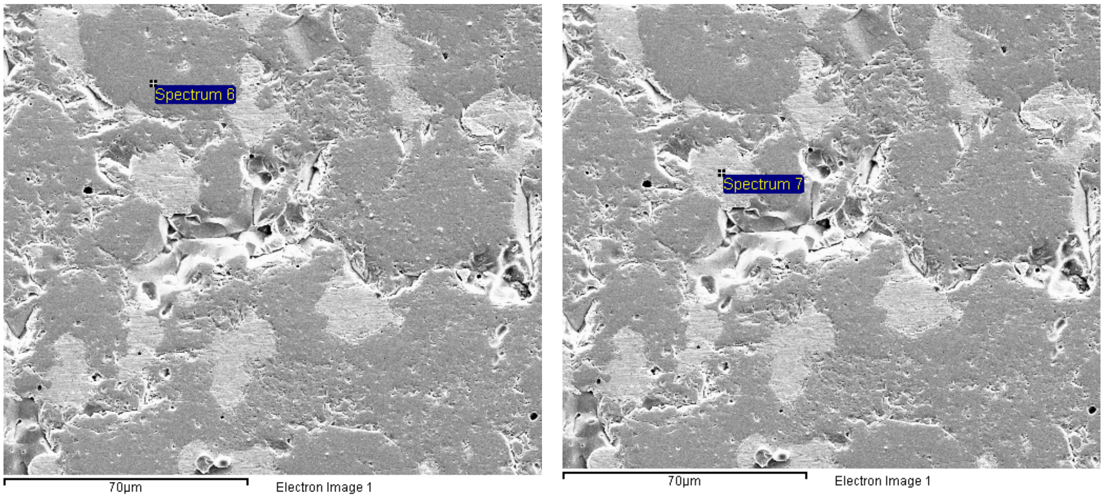

Figure 2.2 SEM images of a typical composite sample used for EDS analysis to characterize the phase compositions at different locations.

Table 2.1 Atomic percentages from EDS analysis at different locations (refer to Figure 2.2).

Spectrum 6	Element	O	Ti	Ba
	Atomic %	60.91	18.15	20.94
Spectrum 7	Element	Ag	C	-
	Atomic %	91.81	8.19	-

To improve its mechanical and dielectric properties silver phase was blended to $BaTiO_3$ ceramics. However, chemical reactions between silver and barium titanate were undesirable. Furthermore, silver oxide might be formed during sintering at high temperature, which is neither desirable. To characterize the existing phases within the composite samples energy-dispersive x-ray spectroscopy (EDS) and x-ray diffraction (XRD) analysis were conducted. Figure 2.2 shows the SEM images of a typical composite sample used for EDS analysis to characterize the phase compositions at different locations. The gray spot (Spectrum 6) was expected to be barium titanate phase, while the white spot (Spectrum 7) was expected to be silver phase. The elements and their atomic percentages at each of these two spots are listed in Table 2.1. At spot "Spectrum 6" three elements exist, namely O, Ti, Ba, and their atomic ratio is approximately 3:1:1, which confirms that it is $BaTiO_3$. The slight percentage of carbon at spot "Spectrum 7", which was expected to be silver phase, might be due to the polishing process and the precision of the EDS technique. The XRD spectrums for Ag/$BaTiO_3$ composites with varying silver composition is shown in Figure 2.3. Only two phases were identified, i.e. $BaTiO_3$ phase and silver phase. In summary, EDS and XRD analysis confirms that no chemical reactions happen between silver and barium titanate and silver did not get oxidized.

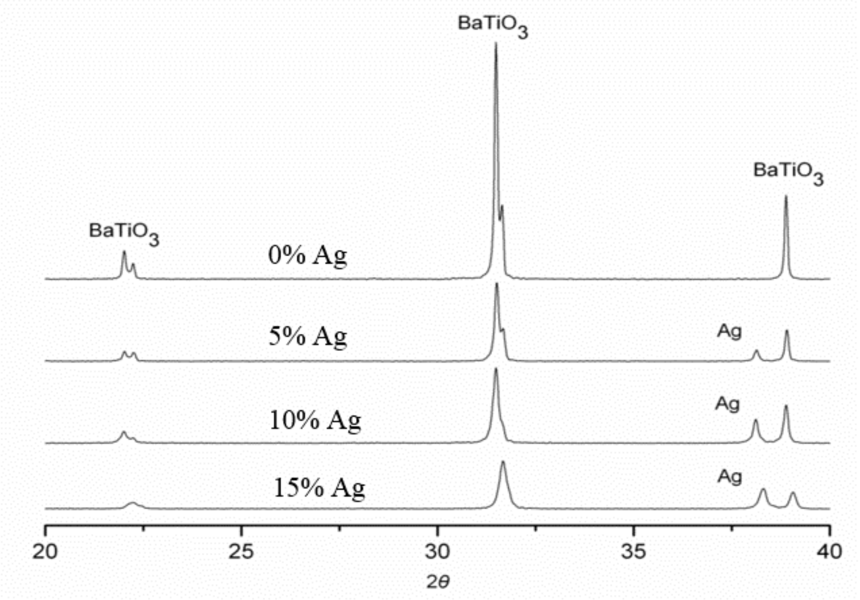

Figure 2.3 XRD spectrums for Ag/$BaTiO_3$ composites with varying silver composition.

2.3 Density

Density was measured by Archimedes' principle, and more details can be found in ASTM standard. 200% proof ethanol was used as the immersion liquid. The density ρ of the sample is given by the following equation:

$$\rho_{sample} = \frac{m_{dry}\rho_{ethanol}}{m_{wet} - m_{suspended} + m_{wire}} \tag{2.1}$$

where m_{dry} is the mass of the sample before immersed in ethanol liquid, $m_{suspended}$ is the mass of the sample measured when suspended in ethanol liquid, m_{wet} is the mass of the sample after soaking in the ethanol, m_{wire} is the mass of suspending system, and $\rho_{ethanol}$ is the density of the ethanol at certain temperature which was measured during the testing. The relative density of the sample is then determined by

$$\text{Relative density} = \frac{\rho_{sample}}{\text{Theoretical density}} \tag{2.2}$$

In addition, the open and closed porosity of the sample can be calculated by the following:

$$\text{Open porosity} = \frac{m_{wet} - m_{dry}}{m_{wet} - m_{suspended} + m_{wire}} \tag{2.3}$$

$$\text{Closed porosity} = 100\% - \text{Relative density} - \text{Open porosity} \tag{2.4}$$

The density of composite samples made using procedures A and B are shown in Table 2.2. The relative density, open porosity and closed porosity were also calculated. There is no significant difference in relative densities between samples made using procedure A and procedure B, which means the final density is more controlled by sintering process rather than cold compaction. The relative density almost stays unchanged for different silver compositions.

Table 2.2 Density and porosity of Ag/$BaTiO_3$ composites from procedure A and B.

	Procedure A				Procedure B		
Volume Fraction	0 vol%	5 vol%	10 vol%	15 vol%	0 vol%	5 vol%	10 vol%
Density ρ (g/cm^3)	5.75 ±0.02	6.03 ±0.01	6.18 ±0.01	6.42 ±0.01	5.80 ±0.01	6.03 ±0.01	6.22 ±0.01
Relative density (%)	95.44	96.61	95.56	96.01	96.39	96.57	96.11
Open porosity (%)	1.83	0.13	0.31	0.21	0.26	0.06	0.09
Closed porosity (%)	2.73	3.26	4.13	3.78	3.35	3.36	3.80

CHAPTER III

THERMAL PROPERTIES OF AG/BATIO3 COMPOSITES AT DIFFERENT TEMPERATURES[*]

3.1 Introduction

Due to its relatively high dielectric constants $BaTiO_3$ based ceramics have found many applications. For example, it can be used as reinforcement to improve the dielectric constant of the composite [162, 163]. It is also widely used in electronic industry like multilayer ceramic capacitors (MLCCs) [1-3]. MLCCs nowadays are widely used in electronic industry because of their high capacitance, relatively small size, and good reliability. For instance, MLCCs are key parts of integrated circuit (IC), which are either embedded in or bonded to the surface of a substrate [164]. The key challenge in such applications is the thermal management because large amount of heat would be generated during service. The mismatch in the thermal properties between MLCC materials and substrates would introduce thermal stresses, which, if large enough, would lead to debonding at the interface or crack in the materials during cycling operations [81]. $BaTiO_3$ based ceramics are also preferred for actuator and sensor applications because they do not contain lead [4, 51]. Due to the large heat generation during cycling service, good thermal management is also a key issue for the integrity and reliability of those devices. In order to improve the durability of $BaTiO_3$ ceramic based devices under harsh thermal

---

[*] Reprinted from Composites Part B: Engineering, 90, Xing J, Radovic M, Muliana A, Thermal properties of $BaTiO_3$/Ag composites at different temperatures, 287-301, Copyright (2016), with permission from Elsevier.

environment, metal phase were doped in $BaTiO_3$ matrix in order to fabricate ceramic/metal composite [6-12, 72]. Compared to monolithic ceramics, the mechanical properties, such as fracture strength and fracture toughness, of the composite containing metallic phase were also greatly enhanced. On the other hand, the introduction of metal phase to $BaTiO_3$ ceramics also can increase its dielectric constants, which is beneficial to the miniaturization of MLCC [1].

In this chapter, we investigated the influence of silver phase on the thermal properties of the $Ag/BaTiO_3$ composite, both experimentally and numerically. The thermal properties that were experimentally measured include CTE, heat capacity, thermal conductivity and thermal diffusivity. Two micromechanics models based on detailed microstructures were constructed to predict the effective CTE and thermal conductivity. One model is 2D based on experimental obtained microstructures from SEM images and the other is 3D based on randomly generated microstructure using random sequential addition algorithm. The influence of microstructural morphologies, such as particle shapes, distribution, and pores, on the effective thermal properties were also investigated. The numerical predictions were compared with the experimentally measured values.

3.2 Experimental procedures

3.2.1 Thermal expansion

The coefficient of thermal expansion of $Ag/BaTiO_3$ composite was measured using a thermal mechanical analyzer (TA Q400, TA instruments, UT), within a temperature range from -50 to 250 °C. The height of the cylindrical samples was between 7 and 10 mm and the diameter was about 9 mm. The top and bottom surfaces were carefully polished to make them parallel. A preload of 0.1 N was applied to ensure perfect contact between the probe and the sample surfaces. To ensure repeatability of the tests two samples were tested for each composition in three heating/cooling cycles each. The heating and cooling rates were 5 ^{o}C/min and 4.6 ^{o}C/min, respectively, according to ASTM standard E831 [165]. Changes in height of the specimen were recorded as a function of temperature. The thermal strain was calculated by dividing the change of height by the original height of the specimen at room temperature. The slope of thermal strain versus temperature curve gives the CTE of the composite.

3.2.2 Heat capacity

The specific heat at constant pressure, C_p, was measured by a differential scanning calorimetry (DSC; TA Q20, TA Instrument, DE). The composite samples were machined into small disk to fit them into the specimen holder, i.e. alumina pan. A synthetic sapphire disk (α-aluminum oxide, TA Instruments) was used as the standard reference material. The scanning was conducted within a temperature range from -50 to 200 ^{o}C with a heating/cooling rate of 10 ^{o}C/min. The heat flow of Ag/BaTiO$_3$ composite during heating/cooling cycles was monitored and recorded as a function of temperature, from which the heat capacity can be calculated. To ensure repeatability of the tests two samples were tested for each composition and two heating/cooling cycles were carried out for each specimen. To accurately determine the heat capacity the recommended procedure given by ASTM standard E1269 [166] was followed. First, the heat flow curve of an empty aluminum pan was measured which would be used as a baseline. Then, the standard sapphire sample was put in the aluminum pan and a reference heat flow curve was measured. Finally, the heat flow curve of the composite was measured using the same aluminum pan. The specific heat of the composite can be determined by the following formula:

$$C_p\left(s\right)=C_p\left(st\right)\cdot\frac{D_s\cdot W_{st}}{D_{st}\cdot W_s} \tag{3.1}$$

where $C_p(s)$ and $C_p(st)$ are the specific heat of the specimen and sapphire sample, respectively; D_s and D_st are the net heat flow of the specimen and sapphire sample at a given temperature; W_s and W_st are the mass of the specimen and sapphire sample.

3.2.3 Thermal conductivity and thermal diffusivity

Hot disk technique (TPS 2500 S, Hot Disk AB), a transient plane source technique, was used to measure the thermal conductivity of the composites at ambient and elevated temperature up to 175 $^\circ$C. During the measurement, a hot disk sensor made of double spiral of nickel wire embedded in Kapton polyimide film was used to generate heat and, at the same time, monitor the temperature changes. It was sandwiched between two cylindrical samples with diameter of 20 mm and height of 9 mm. The recorded temperature change ΔT determined from the electrical resistance change of the nickel sensor is related to the thermal properties of surrounding samples by the following equation [167, 168]:

$$\Delta T\left(t\right)=\frac{F\left(\tau\right)}{K} \tag{3.2}$$

where K is the thermal conductivity of surrounding samples, F is a function depending on $\tau = \sqrt{\kappa t / r^2}$ and other parameters, κ is the thermal diffusivity of surrounding samples, and r is the radius of the nickel sensor. Thermal conductivity, K, of the samples can be calculated by fitting Eq. (3.2). Since thermal diffusivity is related to thermal conductivity by $K = \rho C_p \kappa$, once we know the density and specific heat of the sample, we can also obtain its thermal diffusivity. To arrive Eq. (3.2) infinite domain was assumed, since our samples have finite size we need to make sure that the ambient atmosphere would not affect the transient heat transfer in the nickel sensor, which can be achieved by setting the measurement time $t < r^2/(4\kappa)$ [169]. In this study, the measurement time was set between 2.5 to 7 seconds depending on the sample size and thermal diffusivity. The radius of nickel sensor is 3.189 mm and the output power to the sensor was 0.2 W. To ensure the repeatability four measurements were conducted for each silver composition.

3.3 Experimental results

3.3.1 Thermal expansion

The engineering thermal strain as a function of temperature is shown in Figure 3.1 for different silver compositions. Both heating and cooling curves were drawn from the second running cycle. Thermal hysteresis exits during each heating/cooling cycle, which is due to the energy dissipated during phase transformations. Within the temperature range from -50 to 250 ^{o}C two phase transitions occur around 0 ^{o}C and 120 ^{o}C, i.e. orthorhombic phase to tetragonal phase and tetragonal phase to cubic phase. Around phase transformation temperatures there are obvious shrinkage during the heating cycles and expansion during the cooling cycles, which can be attributed to the contractions or elongations of crystalline lattices. Phase transformation temperatures obtained from the thermal expansion measurement are listed in Table 3.1. The phase transformation temperatures are slightly lower during the cooling cycles (T-O and C-T) than those in the heating cycles (O-T and T-C). The reason for this is that the thermal sensor in TMA measures the ambient temperature. However, the actual temperature in the sample might show certain lag with the ambient temperature. As a result, the actual temperature in the sample might be slightly lower than the recorded one during heating, while slightly higher during cooling. We noticed that the two phase transformation temperatures are slightly different from the previous reported values, namely 0 ^{o}C and 120 ^{o}C [81]. The slope of the thermal strain versus temperature curve gives the CTE of Ag/$BaTiO_3$ composite. Within each phase the thermal strain versus temperature curve shows a nearly straight line, which means the CTE of Ag/$BaTiO_3$ composites is constant at each individual phase. However, as shown in Figure 3.2 the CTE significantly increases from the orthorhombic phase to the tetragonal phase and from the tetragonal phase to the cubic phase. The CTEs calculated during heating and cooling are slightly different. The relative difference, however, is no more than 10.24%. The CTE slightly increases with the increase of silver content because the CTE of silver is significantly higher than that of $BaTiO_3$. Table 3.2 compares the CTE of $BaTiO_3$ ceramic at different crystalline phases with reported data in literature. For all crystalline phases the CTE of $BaTiO_3$ measured in this work is slightly higher than the value previously reported in [79]. In the work of [81] the phase transformation around 0 °C was not detected and the CTE of monolithic $BaTiO_3$ ceramic calculated between 0 and 50 °C is 6×10^{-6} K^{-1} which is between the CTE values measured at orthorhombic phase and tetragonal phase in this work. The CTE of $BaTiO_3$ at cubic phase is 10.51×10^{-6} K^{-1}, which is close to the value of 11.35×10^{-6} K^{-1} reported in [81]. The CTEs of $Ag/BaTiO_3$ composites with different silver content for each individual phase are listed in Table 3.3.

Table 3.1 Phase transformation temperatures obtained from TMA tests and DSC tests, respectively.

Volume fraction	TMA results (°C)				DSC results (°C)			
	O-T	T-O	T-C	C-T	O-T	T-O	T-C	C-T
0 %	33.0	3.5	120.7	102.8	20.6	6.5	126.8	122.6
5 %	27.7	1.3	119.7	104.1	18.7	9.4	129.1	125.6
10 %	27.8	3.2	117.9	103.9	17.5	9.8	128.3	124.7
15 %	31.2	6.9	122.7	106.7	18.9	10.6	128.6	124.4

O-T: orthorhombic to tetragonal
T-O: tetragonal to orthorhombic
T-C: tetragonal to cubic
C-T: cubic to tetragonal

Table 3.2 Comparison of CTE for $BaTiO_3$ with literature data.

Crystalline phases	$BaTiO_3$ (10^{-6} K^{-1})		
	Present work	He[a]	Shirane et al.[b]
Orthorhombic phase	5.30	-	4.60
Tetragonal phase	7.52	6.00	6.50
Cubic phase	10.51	11.35	9.80

[a]: [81]
[b]: [79]

Table 3.3 Coefficient of thermal expansion (CTE) for Ag/BaTiO$_3$ composite.

Crystalline phases	CTE for different silver VF (10^{-6} K^{-1})			
	0 vol%	5 vol%	10 vol%	15 vol%
Orthorhombic phase	5.30	6.23	6.76	7.19
Tetragonal phase	7.52	8.35	9.04	9.65
Cubic phase	10.51	11.03	11.52	11.79

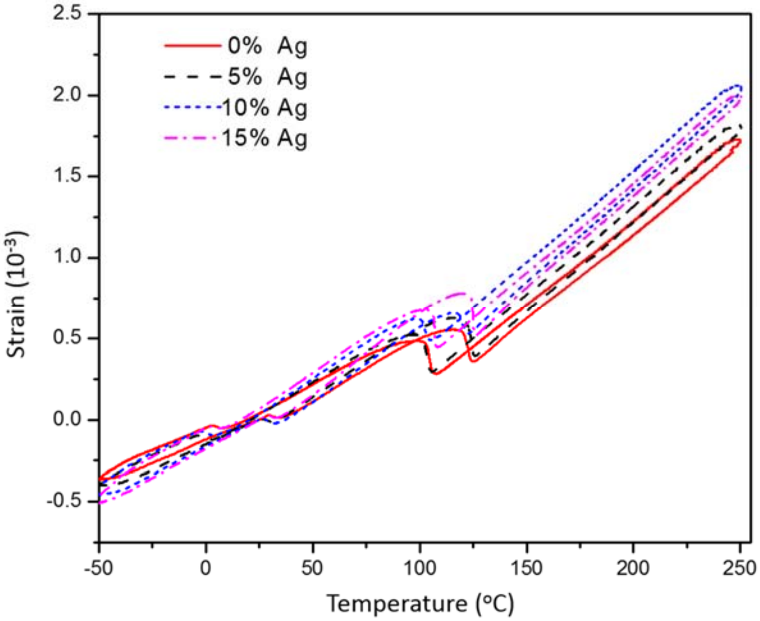

Figure 3.1 Engineering thermal strain as a function of temperature for Ag/BaTiO$_3$ composites.

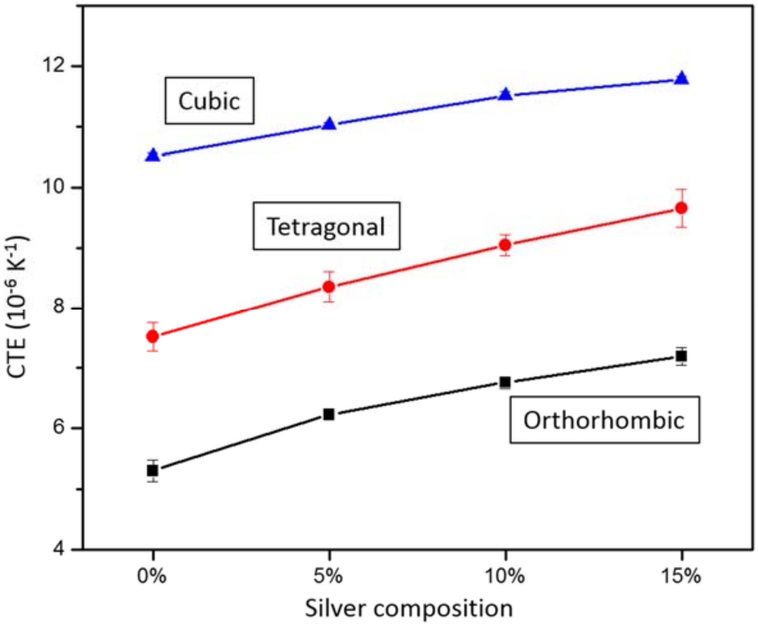

Figure 3.2 Coefficients of thermal expansion for Ag/BaTiO$_3$ composites.

3.3.2 Heat capacity

Typical heat flow curves for Ag/BaTiO$_3$ composite obtained from differential scanning calorimetry are shown in Figure 3.3. It consists of one baseline curve of an empty aluminum pan, one reference curve of a standard sapphire sample and one heat flow curve of a Ag/BaTiO$_3$ specimen. The specific heat capacity of the composite can be calculated by using the vertical distances from the heat flow curves of sapphire sample and BaTiO$_3$ specimen to the baseline curve. The phase transformation temperatures obtained by DSC measurement are listed in Table 3.1. They do not change as the silver content increases, similar to what has been observed in the results of thermal expansion. The phase transformation temperatures measured during heating are slightly higher than those measured during cooling, though such discrepancy is smaller compared with the one from the thermal expansion test. Phase transformation temperatures obtained by DSC measurement are slightly different from those by TMA measurement most likely due to different heating/cooling rate. The heat capacities of Ag/$BaTiO_3$ composite as a function of temperature for each individual phase are shown in Figure 3.4. In contrast with CTE, the heat capacity continuously increases as the temperature increases. An increase in silver contents slightly decreases the heat capacity due to its relatively smaller content in the composites. The large standard deviation in the measurements may be due to the fact the sample used in the testing is very small. As a result it cannot adequately represent the macroscopic property of the composites due to its inhomogeneity. In this study the measured heat capacity for pure $BaTiO_3$ at room temperature is 0.456 J/g.K which is consistent to previously reported values, 0.434 J/g.K in [81] and 0.439 J/g.K in [170].

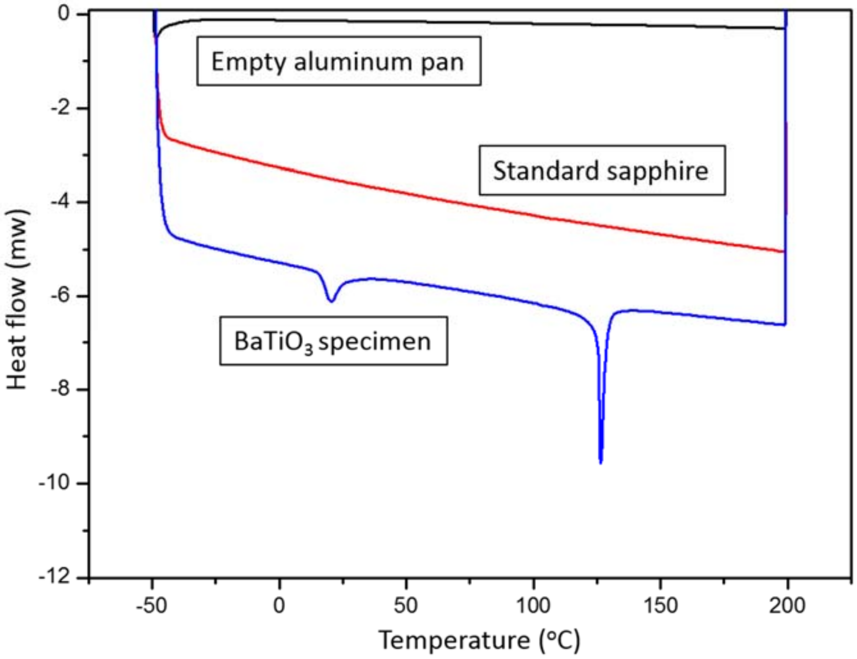

Figure 3.3 Heat flow curves for empty pan, sapphire standard and $BaTiO_3$ specimen.

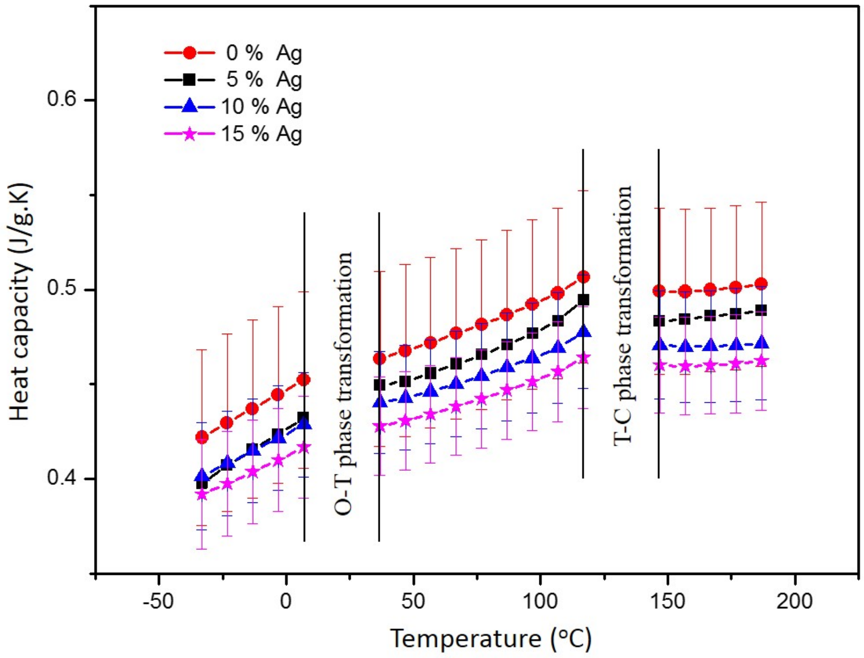

Figure 3.4 Heat capacity of Ag/BaTiO$_3$ composites as a function of temperature.

3.3.3 Thermal conductivity and thermal diffusivity

The thermal conductivity of Ag/BaTiO$_3$ composite at room and elevated temperatures was measured by Hot Disk technique, as shown in Figure 3.5. For a fixed silver composition the thermal conductivity of the composite remains nearly constant below its tetragonal to cubic transformation temperature, which is around 120 °C, then slightly decreases and stays constant after that up to 175 °C. As the silver content increases, the thermal conductivity of the composite is greatly enhanced due to the formation of conductive particle chains [135, 136], which is enhanced by the high contrast of the thermal conductivities between silver and BaTiO$_3$. Heat can flow easily following such conductive chains which greatly enhances the effective thermal conductivity. The measured thermal conductivity of monolithic BaTiO$_3$ ceramic at room temperature is

3.672 W/(mK) which is larger than the value of 2.85 W/(mK) previously reported in [81] but is within the range of 1.3 to 6 W/(mK) reported in [170]. Possible reasons for the variation of thermal conductivity are due to different manufacturing procedures, different dopants added to the material and different measurement techniques used. The thermal diffusivity decreases with an increase of silver content, as shown in Figure 3.6. In this work the room-temperature value of monolithic $BaTiO_3$ ceramic is 1.438 mm^2/s, which is higher than 1.03 mm^2/s and 1.18 mm^2/s reported in [81]. Thermal conductivity and thermal diffusivity of $Ag/BaTiO_3$ composites at ambient and elevated temperatures are listed in Table 3.4 for reference.

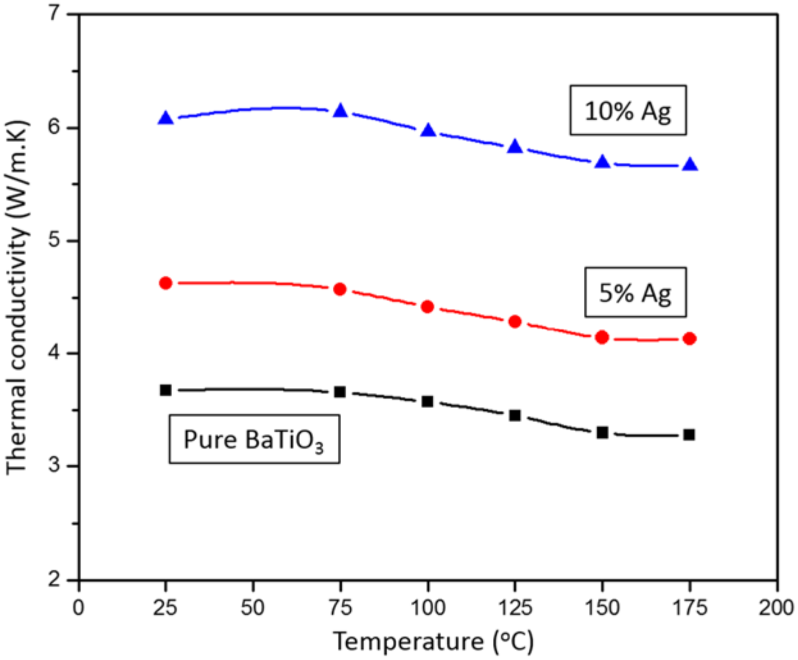

Figure 3.5 Thermal conductivity of $Ag/BaTiO_3$ composite as a function of temperature.

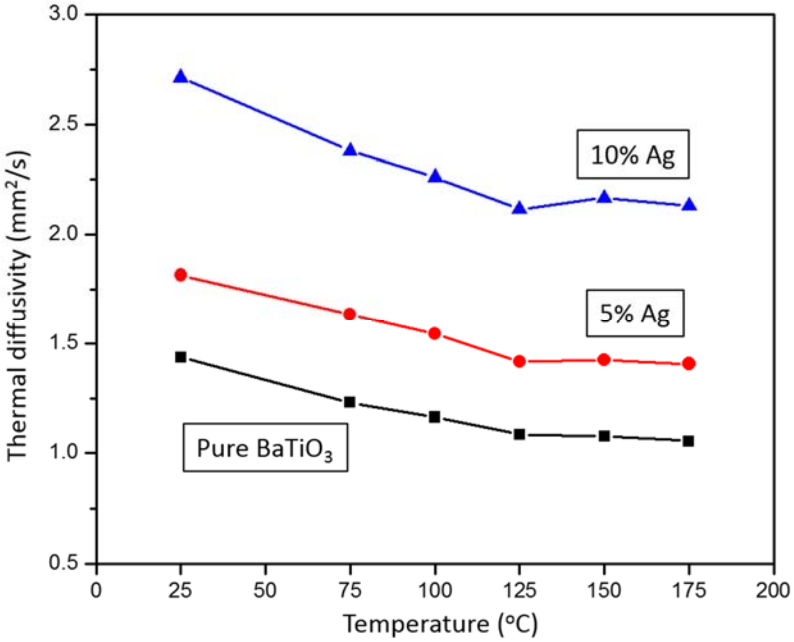

Figure 3.6 Thermal diffusivity of Ag/BaTiO$_3$ composite as a function of temperature.

Table 3.4 Thermal conductivity and thermal diffusivity of Ag/BaTiO$_3$ composites at elevated temperatures.

		Temperature					
		25 °C	75 °C	100 °C	125 °C	150 °C	175 °C
Thermal conductivity (W/mK)	0 vol%	3.672	3.657	3.572	3.450	3.297	3.277
	5 vol%	4.623	4.569	4.417	4.283	4.140	4.129
	10 vol%	6.077	6.142	5.969	5.825	5.688	5.664
Thermal diffusivity (mm^2/s)	0 vol%	1.438	1.231	1.164	1.085	1.076	1.055
	5 vol%	1.814	1.635	1.545	1.418	1.426	1.408
	10 vol%	2.713	2.380	2.261	2.116	2.167	2.132

3.4 Finite element analyses and discussion

Numerical analyses based on micromechanical models were carried out to determine the effective thermal properties of Ag/BaTiO$_3$ composites. Two types of microstructural models implemented in finite element were considered. The first model was constructed from 2D microstructural of the composite obtained using scanning electron microscope images that were further converted into finite element meshes using OOF software as it is described in more details in [127-129]. The second model was based on 3D representative volume element (RVE) of randomly generated solid spherical inclusions dispersed in homogeneous matrix. An advantage of micromechanical models is that it allows investigating the influence of detailed microstructures (particle shape, size, and distribution) on local field fluctuations, such as thermal residual stresses and heat fluxes, on the overall performance of composites. The overall properties of the thermal properties determined from the two different models were compared to each other, as well as to experimental results.

3.4.1 Finite element microstructural models

For the 2D microstructural models of the composite samples, four FE models (FE model #1-4) were generated for each composition to study the reliability of the microstructural representation. The SEM images of these four FE models were taken at different locations of the same sample. The physical sizes of the SEM images range from 415 μm to 547 μm, which were selected based on the following reasons: (1) big enough to represent the overall behavior of the composites; (2) different constituents can be clearly identified; (3) considerations of computational costs. The meshes were generated using the open source software OOF [125] and the finite element analyses were carried out using ABAQUS.

Typical microstructures and FE models for 10 vol% Ag/$BaTiO_3$ composite are shown in Figure 3.7. Figure 3.7 (a) shows the SEM images, in which white colored phase is silver, while gray colored phase is $BaTiO_3$. Pores can be seen as black areas on the same figure. To study the influence of pores on the effective thermal behaviors, FE models with and without pores were created. A FE mesh generated by OOF2 is shown on Figure 3.7 (b)-(c). Inside of each phase the meshes are relatively uniform while at the phase boundaries it is refined to generate a more accurate representation. The meshes for different FE models contain 70,000 to 100,000 elements depending on their detailed microstructures. Silver and pore volume fractions for various FE models are listed in Table 3.5. The listed values for each composition are averaged from four different models. The standard deviations for these four models are also included.

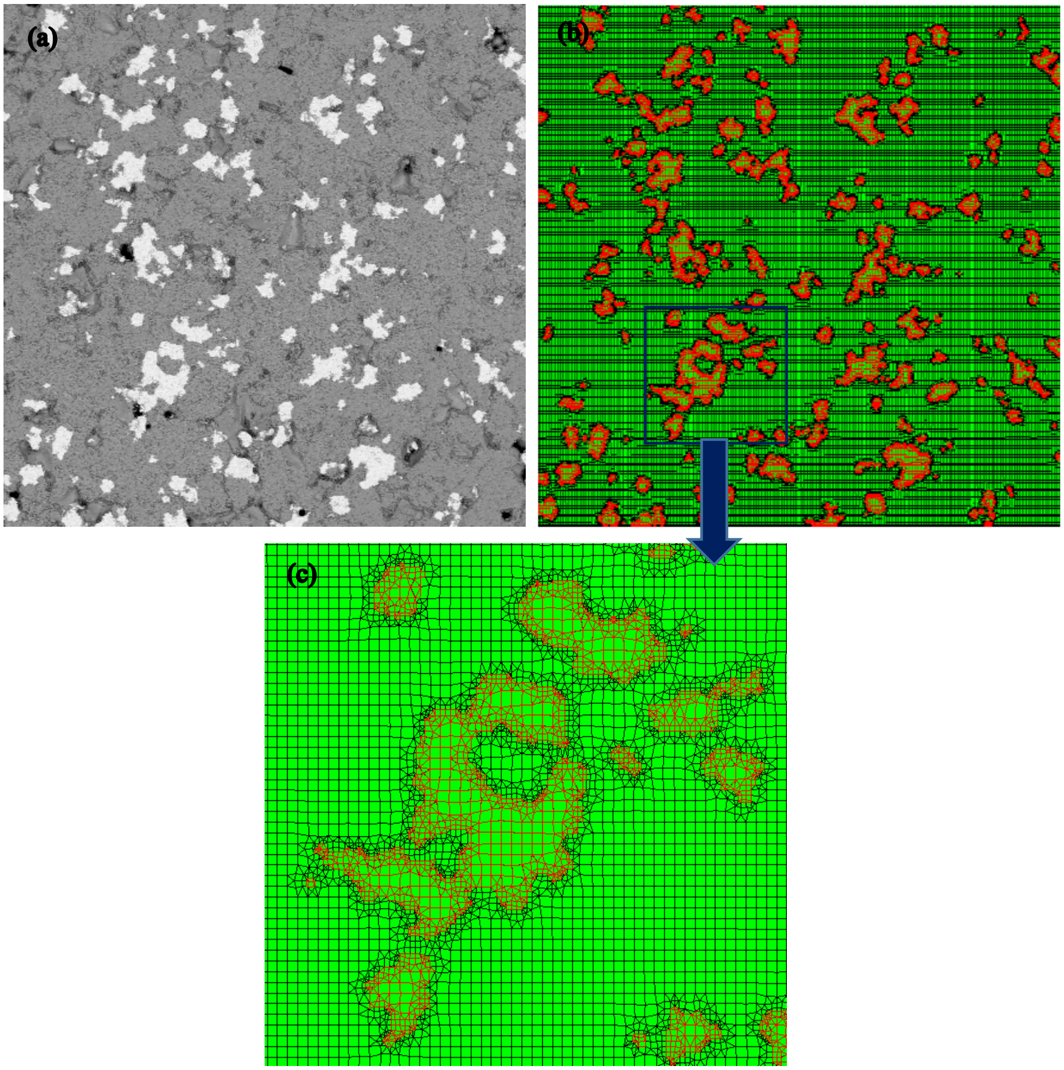

Figure 3.7 Selected but typical microstructure and 2-D FE models for 10 vol% Ag/BaTiO$_3$ composites: (a) SEM image with size 547 x 547 µm; (d) FE meshes; (c) Enlarged meshes of part of the model.

Table 3.5 Silver and pore volume fractions of 2D FE models for effective CTE and K_{eff} analysis

	Phase volume fraction in 2D FE models for effective CTE analysis		Phase volume fraction in 2D FE models for effective K_{eff} analysis	
Samples	Silver VF (vol%)	Pores VF (vol%)	Silver VF (vol%)	Pores VF (vol%)
0 vol%	—	—	—	1.01±0.06
5 vol%	5.02±0.29	—	5.41±0.25	0.87±0.10
10 vol%	10.20±0.47	0.93±0.14	12.26±0.61	0.53±0.02
15 vol%	16.11±0.27	—	—	—

A 3D finite element microstructural model was created by modified random sequential addition algorithm, which can generate statistically isotropic spatial dispersion of particles [171]. The model consists of a cubic volume that contains 30 random and homogeneous distributed identical spherical particles. The radius *r* of each spherical particle can be calculated by the volume fraction of reinforcement particles and the number of particles generated within the cube. Overlapping between particles was excluded by the method of separating axis [172]. A minimum distance between different particles and between particles and surfaces was enforced to avoid distortion of finite element meshes. The minimum distance was selected to make sure that at least two layers of elements were generated between particles. The particles intersecting with side surfaces of the cube were copied to appropriate opposite surfaces to make the unit cell symmetric. Since the number of randomly generated spherical particles in the cube is large enough, it is safe to treat the unit cell model as RVE. A typical 3D model with the finite element meshes is shown in Figure 3.8.

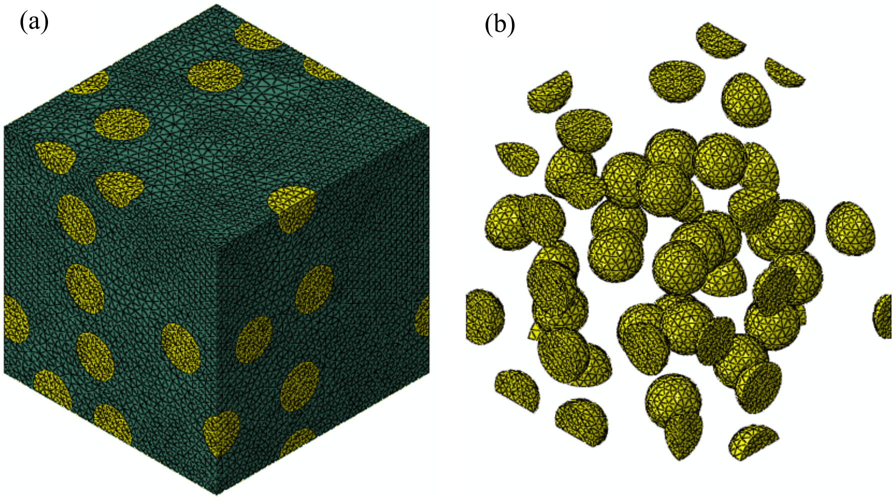

Figure 3.8 3D FE model and meshes for typical 10 vol% Ag/BaTiO$_3$ composites: (a) FE meshes of the composite; (b) FE meshes of silver particles.

Commercial software ABAQUS is used to perform the analyses of heat conduction and deformation due to temperature changes. The effective CTE is calculated from the thermal expansion analysis, while the effective thermal conductivity is calculated from a steady state heat transfer analysis. Boundary conditions and constrains applied to the 2D FE model are given bellow, and those for the 3D model can be derived similarly. For the thermal expansion analysis the following boundary conditions were employed,

$$\begin{aligned} u_x(0,y)&=0; \qquad 0\le y\le L \\ u_y(x,0)&=0; \qquad 0\le x\le L \end{aligned} \tag{3.3}$$

Multipoint constraints were applied as follows to other edges to ensure their straightness after deformation,

$$\begin{aligned} u_x(L,y)&=u_{right}; \qquad 0\le y\le L \\ u_y(x,L)&=u_{top}; \qquad 0\le x\le L \end{aligned} \tag{3.4}$$

In ABAQUS thermal expansion analysis is implemented by defining temperature as a predefined field. If the initial temperature is T_i and the final temperature is T_f, the effective CTE was calculated by

$$\begin{aligned} &\alpha_x = \frac{\bar{\varepsilon}_{xx}}{\Delta T}, \quad \bar{\varepsilon}_{xx} = \frac{u_{right}}{L}, \quad \Delta T = T_f - T_i \\ &\alpha_y = \frac{\bar{\varepsilon}_{yy}}{\Delta T}, \quad \bar{\varepsilon}_{yy} = \frac{u_{top}}{L} \end{aligned} \tag{3.5}$$

To calculate the effective thermal conductivity in the x direction the following boundary condition and loading were employed,

$$\begin{aligned} &T(0, y) = 0; \qquad 0 \le y \le L \\ &q_x(L, y) = q_{right}; \quad 0 \le y \le L \end{aligned} \tag{3.6}$$

where q_x is the external heat flux applied on the right edge.

A multipoint constraint was apply to enforce uniform temperature on the right edge during the analysis,

$$T(L, y) = T_{right}; \qquad 0 \le y \le L \tag{3.7}$$

The thermal conductivity in x direction was given by

$$\lambda_x = \frac{q_x}{\bar{\beta}_x}, \quad \bar{\beta}_x = \frac{T_{right}}{L} \tag{3.8}$$

In addition to the above mixed boundary conditions (BCs) various other boundary conditions, such as constant temperature gradient, uniform flux and periodic BCs, are considered to understand their influence on the effective thermal conductivity. With respect to periodic BCs, since our microstructures and meshes are not periodic, polynomial functions are used to approximate the field fluctuations on the boundaries [173]. In ABAQUS polynomial functions and reference points are used as constraints to the boundaries. For example, the 2nd order polynomial approximation is defined by the following equations:

$$\begin{aligned} &T(0,y)=T_{x0}+T_{x1}\left(\frac{y}{L}\right)+T_{x2}\left(\frac{y}{L}\right)^2, \quad T(L,y)=T(0,y)+\langle\vec{g}\rangle\cdot\vec{p}_x; \\ &T(x,0)=T_{y0}+T_{y1}\left(\frac{x}{L}\right)+T_{y2}\left(\frac{x}{L}\right)^2, \quad T(x,L)=T(x,0)+\langle\vec{g}\rangle\cdot\vec{p}_y \end{aligned} \tag{3.9}$$

where $T_{x0},\cdots,T_{y2}$ are the temperatures at reference points; $\vec{p}_x=(L,0)^T$ and $\vec{p}_y=(0,L)^T$; and $\langle\vec{g}\rangle$ are the applied macroscopic temperature gradients. It was shown [174] that the effective thermal conductivities obtained by applying periodic BCs are bounded between those obtained from applying uniform flux and constant temperature gradient BCs, where the uniform flux BC leads to a lower bound and the constant temperature gradient BC leads to an upper bound. In addition, they showed that if the thermal conductivity of the particulate reinforcement is larger than that of the matrix, which is the case in this study, then the convergence rate of uniform flux BC is similar to that of periodic BC and is much faster than that of constant temperature gradient BC. The mixed BC gives a close prediction to the lower bound (uniform flux BC), see section 3.4.4. A constraint (Eq. (3.7)) in the mixed BC was applied to impose constant temperature on the edges. Then the corresponding temperature gradient is calculated from Eq. (3.8) instead of determining the volume average by numerical integration, which significantly reduces the computational cost. The predictions from the mixed BC are very close to uniform flux BC because such a constraint is very weak. As a result, in the following simulations the mixed BC are employed except a comparison of various BCs in section 3.4.4.

The finite element simulations for determining the overall thermal properties were conducted by prescribing fixed temperatures, discussed in Eqs. (3.5)-(3.8). For example, to calculate the effective thermal conductivity of the composite at 25 °C, the inputs are the thermal conductivities of the two constituents ($BaTiO_3$ and Ag) at 25 °C, while the thermal conductivities of the two constituents at 100 °C serve as the inputs for the predictions at 100 °C. The mechanical and thermal properties of $BaTiO_3$ and Ag used in this study are listed in Table 3.6. In the temperature range we studied (-50 to 250 °C) the elastic constants, CTE and thermal conductivity of silver only slightly change [175-177]. For example, the thermal conductivity is 428 W/mK at 0 °C, while it slightly reduces to 413W/mk at 227 °C. So in the simulation we employed those values at ambient temperature. The CTE and thermal conductivity of $BaTiO_3$ at ambient and elevated temperatures are listed in Table 3.3 and Table 3.4, respectively. Its elastic constants significantly change with temperatures even within each phase [178]. However it only slightly affects the effective CTE of the composites as shown later.

Table 3.6 Material properties of $BaTiO_3$ and Ag at room temperature.

	Modulus (GPa)	Poisson's ratio	Yield Strength (MPa)	CTE (10^{-6} K^{-1})	Thermal conductivity (W/mK)
$BaTiO_3$[a]	119.86	0.323	—	—[b]	—[c]
Ag[d]	76.0	0.370	55.0	19.6	419.0

[a]: This work
[b]: See table 3.3
[c]: See table 3.4
[d]: [175-177]

3.4.2 Effects of microstructures and material properties

In this section we examine the significance of possible microstructure-introduced anisotropy and inhomogeneity, and also the influence of porosity and material properties on the effective CTE and thermal conductivity. In the 2D real microstructure based FE models, four FE models were created for each composition to study the influence of microstructural dispersion. Table 3.7 shows examples of variations in silver contents for different FE models with around 10 vol% silver content, which were calculated from the pixel fraction of silver phase in the SEM images. The calculated effective CTE and thermal conductivity are plotted in Figure 3.9 (a)-(b). By comparing Table 3.7 with Figure 3.9 (a)-(b) it is seen that the calculated effective CTE and thermal conductivity increased with the increase of silver content, which is expected since silver has higher CTE and thermal conductivity than $BaTiO_3$. For all FE models and both loading directions, the effective CTE varies between 8.52 to 8.77 μm/mK and the thermal conductivity varies between 4.960 to 5.401 W/mK. The relative difference for the effective CTE is 2.87%, while 8.17% for the thermal conductivity. This suggests that thermal conductivity is more sensitive to microstructure of the composite than the CTE. One possible reason is that the elastic moduli of $BaTiO_3$ and Ag are comparable which introduces small internal stresses between these two phases. Thermal conductivity of Ag, however, is much larger than that of $BaTiO_3$, which leads to significant local heat flux concentration between phases, and large differences in thermal conductivity of the composites with only slight differences in phase compositions. While this investigation shows the dispersion of effective thermal properties is relatively small, it also validates the necessity of statistical treatment of results. Figure 3.9 (c)-(d) shows the effective CTE and thermal conductivity averaged from four FE models as a function of silver composition. It is clear that the averaged values are less sensitive to loading directions.

Figure 3.10 shows the effect of porosity on the effective CTE and thermal conductivity. The volume fractions of silver and pores are given in Table 3.5. While the influence of pores on CTE is negligible, porosity reduces the effective thermal conductivity. The reason is due to the small thermal conductivity of the pores, which serve as thermal barriers and interrupt the heat-flow path in the composite. For the thermal expansion analysis, the mismatch of the CTE for different phases introduces thermal residual stresses within each phase. The magnitude of such thermal stress depends on the differences in CTEs between individual phases, the mechanical property of each phase, and the geometry of the reinforcements. For Ag/$BaTiO_3$ composite the thermal residual stress may even exceed the yield limit of the silver phase. Furthermore, as shown in [178] the Young's modulus of $BaTiO_3$ increases significantly from tetragonal phase to cubic phase, which may influence the effective CTE of the composite. The effects of yielding of silver phase and the increase of Young's modulus of $BaTiO_3$ from tetragonal to cubic phase on the effective CTE of the composite were examined in this study, as shown in Table 3.8. The yielding stress of silver is 55.0 MPa and the Young's modulus of $BaTiO_3$ in cubic phase is 189.357 GPa [178]. The yielding of silver phase decreases the calculated effective CTE, and so as the increase of the Young's modulus of the $BaTiO_3$. However, the relative difference is small. For example the largest relative difference due to the increase of Young's modulus is 2.17%, while only 0.81% due to the yielding of silver phase. At high temperatures silver may experience creep. However, based on data available in literature [179], creep strain under stress 77.2 MPa at 250 ^{o}C increases by less than 2% for a loading period of about 30 minutes. In this study, the thermal expansion test is conducted up to the highest temperature is 250 ^{o}C. The time period when the samples experienced a temperature change between 150 ^{o}C and 250 ^{o}C is approximately 30 minutes, and it is expected that the creep strain due to this period of temperature increase is much smaller than 2%. It is noted that the thermal stresses developed in the composites gradually increase with increasing temperatures, and the maximum thermal stresses occur at 250 ^{o}C and these stresses decrease when the temperature is immediately brought back to the initial temperature. Thus, we neglected the creep behavior of silver at elevated temperatures during thermal expansion analysis.

Table 3.7 Silver volume fraction of 2D FE model for 10 vol% Ag/BaTiO$_3$ composite.

	FE Model #1	FE Model #2	FE Model #3	FE Model #4
Silver VF in effective CTE analysis (vol%)	10.13	11.55	9.54	9.59
Silver VF in effective K_{eff} analysis (vol%)	12.25	11.16	11.70	13.95

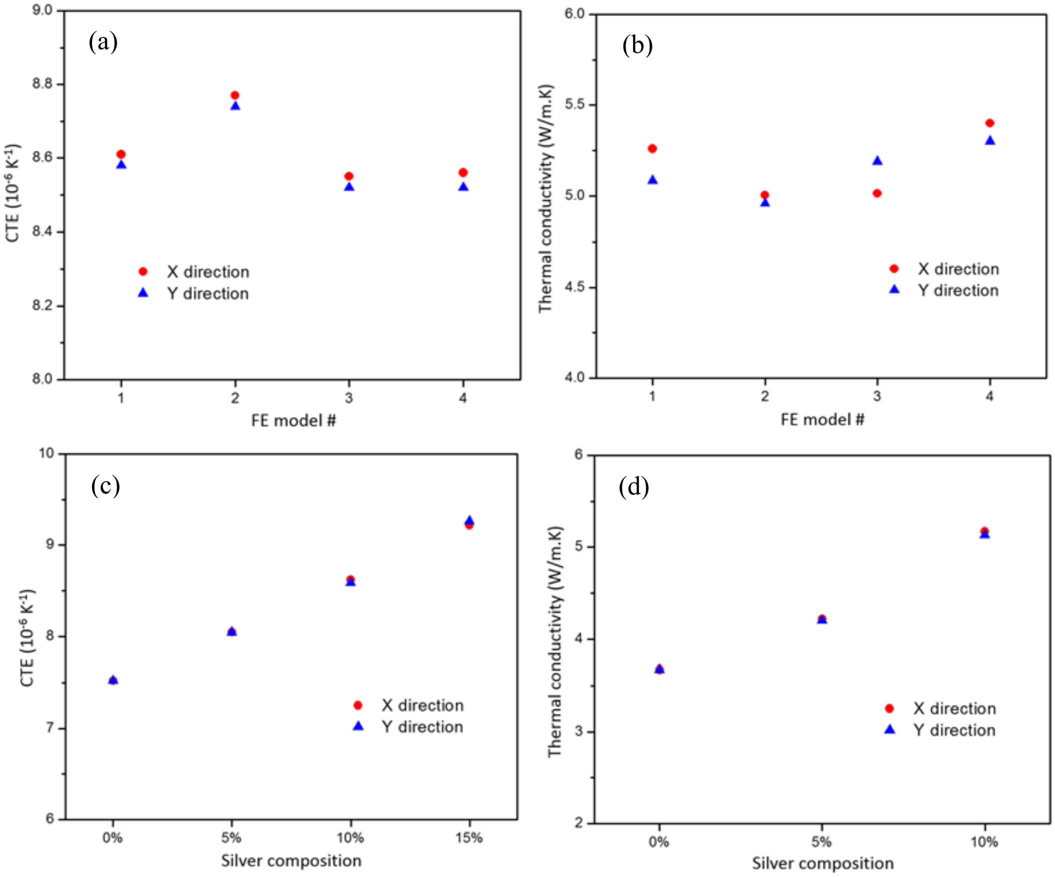

Figure 3.9 Effects of microstructure and loading direction on effective CTE and λ_{eff}: (a) CTE for 10 vol% Ag/$BaTiO_3$; (b) λ_{eff} for 10 vol% Ag/$BaTiO_3$; (c) CTE at tetragonal phase; (d) λ_{eff} at room temperature.

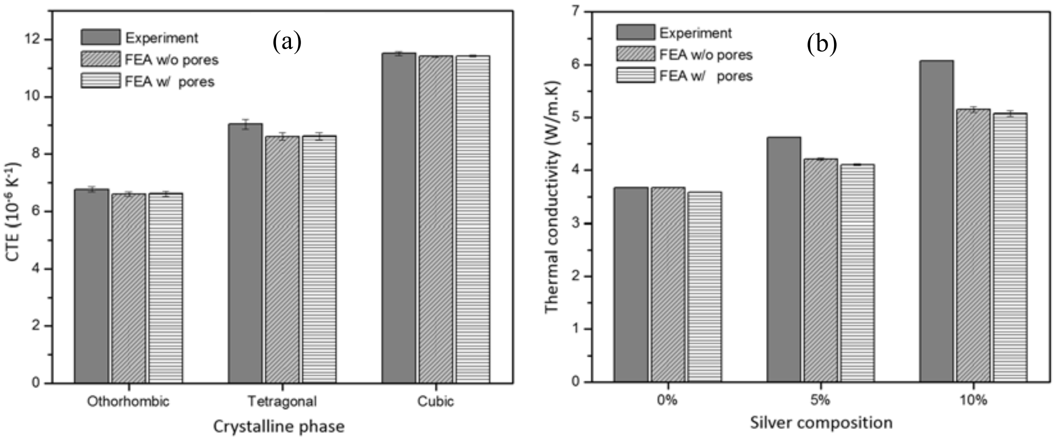

Figure 3.10 Effects of pores on effective CTE and λ_{eff}: (a) CTE for 10 vol% Ag/$BaTiO_3$; (b) λ_{eff} at room temperature.

Table 3.8 Effects of silver yielding and temperature dependent Young's modulus on the effective CTE (10^{-6} K^{-1}).

FE model	Effect of Ag yielding		Difference	Effect of *E*		Difference
	Elastic	Elastoplastic		Room temp. E	High temp. E	
#1	8.60	8.53	0.76%	8.60	8.43	1.98%
#2	8.76	8.68	0.81%	8.76	8.57	2.17%
#3	8.54	8.47	0.74%	8.54	8.38	1.88%
#4	8.54	8.48	0.72%	8.54	8.38	1.92%

3.4.3 The effective CTE

The effective CTEs are averaged from the predictions of four FE models to reduce the dispersion of microstructures. Firstly we will investigate the dispersion of simulated effective CTEs. The highest recorded standard deviation of the effective CTEs is 0.06 μm/mK, which is very small compared to the magnitude of average CTEs (approximately two orders of magnitude lower than the average CTEs). Furthermore, the values of standard deviations are comparable for all cases, suggesting that the chosen 2D FE models can reasonably represent the microstructures of composites in terms of thermal behaviors. In other words, for the thermal expansion analysis the microstructural models are statistically homogeneous and can represent the homogenized macroscopic behavior of the composite. In addition, among all phases and compositions the largest relative difference between effective CTEs in *x* and *y* directions ($|K_x-K_y|/K_x$) is 0.61%, which suggests the simulated effective CTEs for our models are almost isotropic, i.e. the effective strains are insensitive to the loading directions.

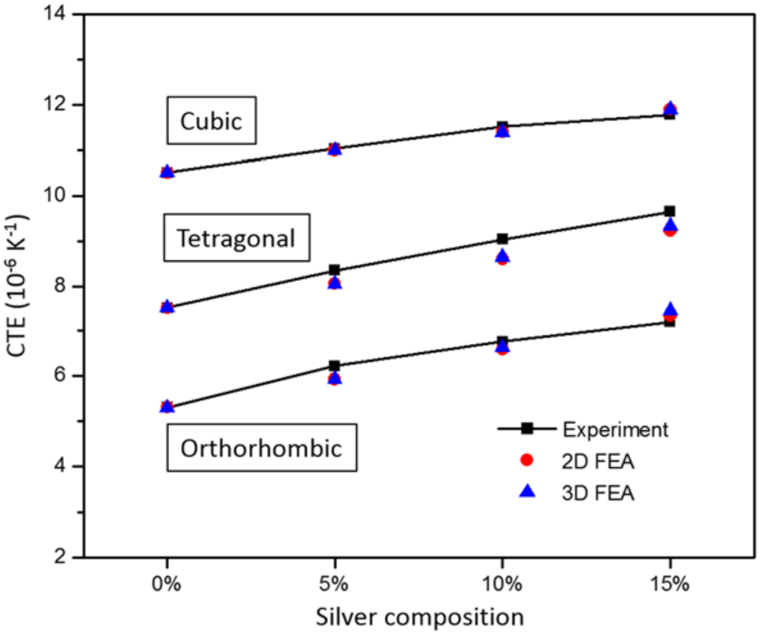

Figure 3.11 Effective CTE for Ag/BaTiO$_3$ composite: comparison between experiment and simulated results from 2D and 3D models.

Figure 3.11 shows the comparison of CTEs from 2D and 3D microstructural models and experimental results for all phases and silver compositions. For the 2D models the plotted values are calculated by averaging results from four FE models, two loading directions, and heat/cooling cycles. Except for the composite with 15 vol% Ag content at orthorhombic and cubic phases, the simulated results are slightly smaller than those of measured data. The largest deviation of the simulated CTEs from the measured ones is for the composite with 10 vol% Ag content at the tetragonal phase, which is 4.84% in relative error. Among all three phases the largest difference happens at the tetragonal phase since the dispersion in the measured CTEs and the difference between heating and cooling at the tetragonal phase is larger than at other two phases. The simulated effective CTEs from the 3D FE models based on randomly generated microstructures are very close to those of the 2D FE models which are based on realistic microstructures. The largest relative difference is shown for the orthorhombic phase for the composite with 10 vol% Ag content, which is 1.6%. As a result, it is more desirable to use 2D realistic microstructure based FE model, because the computational cost for the 2D models are much less than 3D model meanwhile the accuracy of the calculated effective CTEs are comparable. However, the detailed thermal residual stress and stress concentrations for 2D and 3D FE models are quite different as shown later. It is also concluded that the predicted effective CTEs are insensitive to the shape and size of the silver particles.

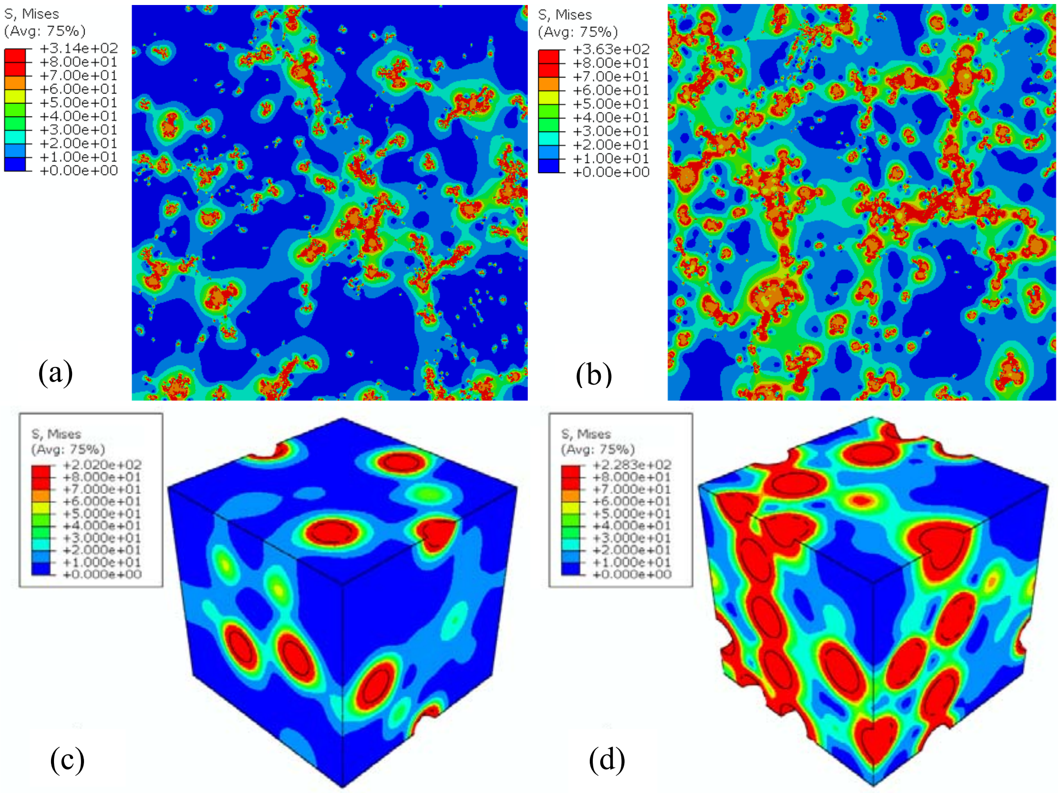

Figure 3.12 Simulated residual thermal stress for Ag/BaTiO$_3$ composite: (a)-(b), 2D results for 5 vol% and 10 vol% composite, respectively; (c)-(d), 3D results for 5 vol% and 10 vol% composite, respectively. The unit for stress is MPa.

One advantage of the microstructural based modeling is that we can examine the local field fluctuations in the composite and their effects on the overall performance/properties of the composite. For the thermal expansion analysis one of the most important local fields are the residual (thermal) stresses. The Ag/$BaTiO_3$ composite samples were manufactured by powder metallurgy method. After cold-pressing the green body was heated up to 1250 °C and then cooled down to room temperature. As a result, at room temperature the composite sample might experience significant internal thermal residual stresses. The effective thermal properties might be insensitive to the internal residual stress introduced during sintering. Its effect on the mechanical properties, however, usually cannot be neglected, as reported in [128]. Figure 3.12 presents the simulated thermal residual stress for the 2D and 3D finite element analyses. The thermal stresses for composites with 5 vol% and 10 vol% silver contents are shown. In the simulation we assume $BaTiO_3$ is at tetragonal phase. The initial temperature is set at room temperature, i.e. 25 °C. Then the composite is heated up to 120 °C. The selected temperature range for the simulation approximately is within the temperature span of the tetragonal phase for $BaTiO_3$ ceramic. Most of the residual stresses are located within and around the silver particles. Composites with 5 vol% silver contents have smaller regions with noticeable thermal stresses, compared to the ones with 10 vol% silver contents. The yield strength for silver is about 55 MPa as listed in Table 3.6. Figure 3.12 indicates that the residual thermal stress in the silver is greater than 60 MPa, which would result in yielding of silver. However, as shown in Table 3.8 the yielding of silver phase has little influence on the calculated effective CTEs. In addition, the simulated effective CTEs are in good agreement with experimentally measured values, which further validates that the effect of plastic deformation of silver is insignificant in case of thermal expansion analysis. It can be seen that smaller distance between two adjacent silver particles leads to larger stress concentration. As shown in Figure 3.12 (c)-(d) the stress concentration in 3D model is lower than that in 2D real microstructure based FE models, which is due the spherical silver particle approximation used in the 3D FE models.

3.4.4 The effective thermal conductivity

To make sure that the 2D micromechanical models can approximate the macroscopic behavior of the composite in heat transfer analysis, again firstly we will investigate the dispersion of simulated effective thermal conductivities. The analyses at all temperatures and silver compositions showed that the largest difference in effective thermal conductivities measured in the *x* and *y* directions is 0.7%, indicating a reasonable isotropic assumption. The largest dispersion is 0.10 W/mK at 25 °C and 75 °C for composite with 10 vol% silver. This value is small compared with the magnitude of the effective thermal conductivity itself.

Figure 3.13 shows the effective thermal conductivities by using polynomial functions up to 5th order. Note that the linear polynomial approximation (1st order) is equivalent to the constant temperature gradient BC. As expected increasing the polynomial order decreases the prediction of the effective thermal conductivities but the rate is slow due to the inefficiency of polynomial approximation to approximate highly fluctuated functions. As shown in literature [173], a polynomial of order over 20 or even

30 is needed to reach convergence for mechanical properties. In this study, it seems that the effective thermal conductivities from periodic BCs reach convergence at 5th order polynomial. In addition, the mixed BC gives a close prediction to the lower bound (uniform flux BC). The predictions from mixed and constant temperature gradient BCs for 2D and 3D micromechanics models are plotted in Figure 3.14. Under the mixed BC the predictions from 2D and 3D are very close, and the largest relative difference is 1.29%. In contrast, under constant temperature gradient BC the predictions from 2D and 3D models differ significantly. The predictions from 3D models are much larger than those from 2D models because the number of particles in 3D models is less than that in 2D models (based on SEM images).

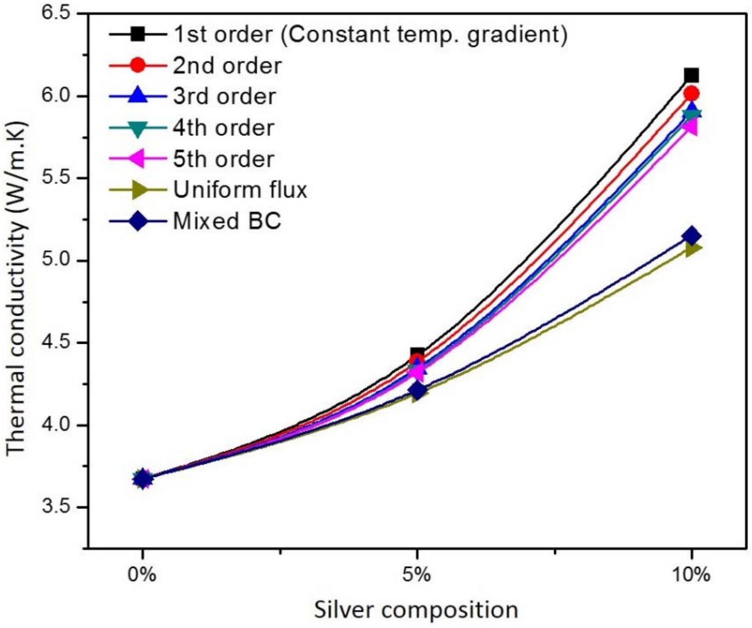

Figure 3.13 Effective thermal conductivities predicted by various boundary conditions for 2D micromechanical models at 25 °C.

Comparison of experimental results and the effective thermal conductivities from 2D micromechanics models with constant temperature gradient BC and mixed BC is given by Figure 3.15. The predictions from the constant temperature gradient BC (1st order periodic BC) give upper bounds and are close to the experiment results. On the other hand, the predictions from mixed BC underestimate the experiment results. The percent difference in the thermal conductivities from the mixed BC is 7.23-8.93% for 5 vol% composite and 15.22-18.71% for 10 vol% composite. One possible reason for the discrepancies is the high contrast in thermal conductivity between silver and $BaTiO_3$, which leads to high heat flux concentrations, which cannot be captured in the mixed BC. Figure 3.16 shows that the heat flux concentration for composites with 10 vol% silver is higher than the one with 5 vol% silver. In this study we did not take into consideration of the thermal contact resistance between constituents since we do not have information pertinent to the contact behaviors between $BaTiO_3$ and silver. Thermal contact resistance is usually determined experimentally due to its complex influencing factors, such as the thermos-physical and mechanical properties of the constituents, the presence of gaseous or nongaseous interstitial media, the apparent contact pressure, and so on [180].

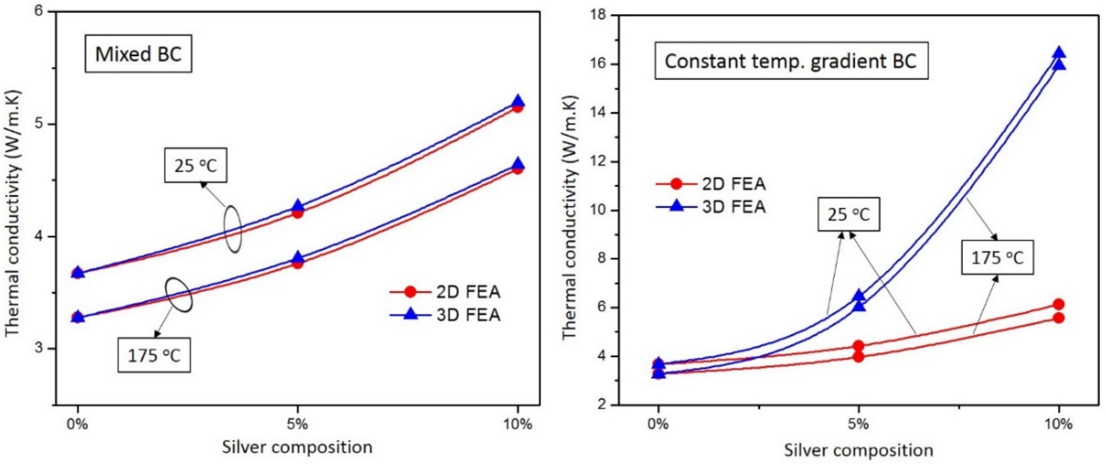

Figure 3.14 Comparison of predictions between 2D and 3D micromechanics models: left, mixed BC; right, constant temperature gradient BC.

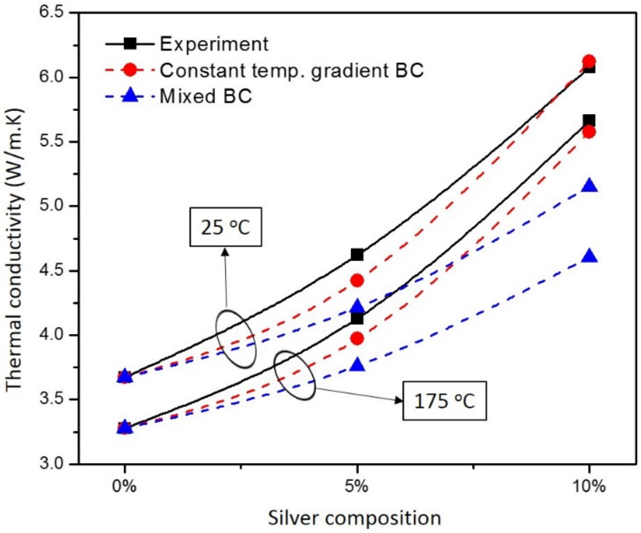

Figure 3.15 Comparison of experiment results to predictions from 2D micromechanics models with constant temperature gradient BC and mixed BC.

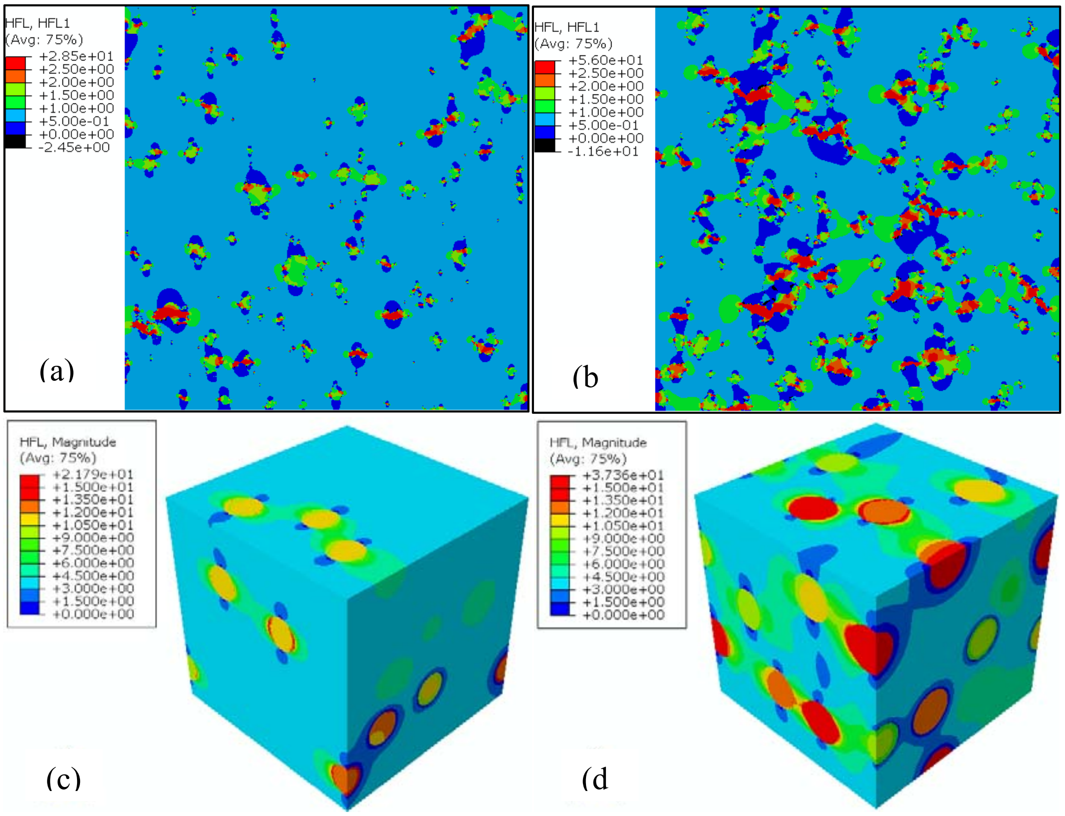

Figure 3.16 Simulated heat flux for Ag/BaTiO$_3$ composite: (a)-(b), 2D results for 5 vol% and 10 vol% composite, respectively; (c)-(d), 3D results for 5 vol% and 10 vol% composite, respectively. The unit for heat flux is μW/μm^2.

Detailed local heat flux fields for composites with 5 vol% and 10 vol% silver contents are shown in Figure 3.16 for 2D and 3D models. In the simulation right edge ($x=L$) of the model is prescribed with a temperature of 0 °C and the left edge ($x=0$) with 100 °C. Since it lies in the temperature span of tetragonal phase of BaTiO$_3$ ceramic within which its thermal conductivity almost stays constant, thermal conductivity for BaTiO$_3$ at room temperature is used as the input in the simulation. The heat transfer is assumed to be steady state. As shown in Figure 3.16 (a)-(b) only a very small part has heat flux in the ranges from 2.5 to 28.5 μW/μm^2 for composites with 5 vol% silver and from 2.5 to 56 μW/μm^2 for the composite with 10 vol% silver. The composite with 10 vol% silver has higher heat flux concentration compared to the one with 5 vol% silver. Higher heat flux is seen in the silver constituent. Lowest magnitude of heat flux happens at the interfaces between $BaTiO_3$ and silver constituents. When heat flows in the *x* direction and approaches phase boundaries it is attracted by silver phase due to its much higher thermal conductivity. Heat flux concentration also occurs in the regions between adjacent silver particles with small spacing because heat flows following a passage of higher conductive constituent. Heat flux concentration in 3D model is lower than that in 2D model, as shown in Figure 3.16 (c)-(d), due to its smoother spherical silver particles. The heat flow paths in the matrix are clearly observed in Figure 3.16 (c)-(d) as indicated by the green contours connecting silver particles.

CHAPTER IV

CHARACTERIZATION OF THERMAL TRANSPORT PROPERTIES OF COMPOSITES USING HOT-DISK: EXPERIMENTS AND SIMULATIONS

4.1 Introduction

Thermal management is a key challenge in a wide range of applications of materials due to the large amount heat that would be generated during service. For example, piezoelectric ceramics like barium titanate ($BaTiO_3$) and lead zirconate titanate (PZT) were widely used as actuators and sensors. Due to the large heat generation during cycling service, good thermal management is a key issue for the integrity and reliability of such devises. Thermal conductivity, thermal diffusivity and heat capacity are key thermal transport properties of materials. Knowledge of these thermal properties of materials is crucial for the design and performance of many devises under harsh thermal environment, such as thermal management of electronic packages in semiconductor industry. In order to improve the overall performance of devices, composites are often considered. For example, metal or polymer phases were blended into $BaTiO_3$ and PZT to improve its fracture toughness and ductility. Consequently, in addition to the mechanical properties of each individual phase the macroscopic effective thermal properties also need to be characterized. The aim of this chapter is to understand the effects of different microstructural morphologies of composites on their effective thermal properties determined from hot-disk technique.

Hot disk technique, as a transient plane source technique, has gain popularity due to its rapidness and accuracy. Furthermore, this technique can provide both thermal conductivity and thermal diffusivity of the specimen at the same time. During the measurement, certain amount of heat was generated on the hot disk sensor, made of double spiral of nickel wire embedded in Kapton polyimide film, by supplying a small constant current. At the same time, it also records the temperature changes of the specimen. The sensor was sandwiched between two plates of materials which thermal properties are measured. The recorded temperature change ΔT , determined from the electrical resistance change of the nickel sensor, is related to the thermal properties of surrounding samples by $\Delta T(t) = F(\tau)/K$, where $\tau = \sqrt{\alpha t/r^2}$, K and κ are the thermal conductivity and thermal diffusivity of the specimen, and r is the radius of the nickel sensor [169]. The selection of experimental time window under different situation was studied in the hot dick configuration by conducting sensitivity analysis in [181].

Various micromechanics models were put forward in literature to predict the effective thermal conductivity of composite materials as reviewed in Chapter I. Among them the micromechanics models based on the detailed microstructures of the composite has the advantage of simulating the detailed local field fluctuations, such as heat flux concentration and flowing paths. However, such models are usually based on steady state heat transfer analysis and can only predict the effective thermal conductivity. In this chapter, a micromechanics model based on transient heat transfer analysis was developed to predict the effective thermal conductivity, thermal diffusivity and heat capacity of composite materials, which mimics the hot disk experiment technique. Compared to micromechanics model based on steady state analysis, this model can predict various effective thermal properties at the same time. The detailed microstructure of the model was built based on randomly generating reinforcement particles in a square matrix. The effects of heat source geometry and particle size were studied. Sensitivity analysis were carried out to study the effects of small perturbations on the input data. Various effective thermal properties of Ag/$BaTiO_3$ composite were predicted and compared to experimental and numerical results previously reported in [182].

4.2 Conduction of heat in the hot-disk test

The conduction of heat in an isotropic and homogeneous infinite media can be described by the following parabolic partial differential equation [183]:

$$\begin{aligned} K\nabla^2 T + Q &= \rho c \frac{\partial T}{\partial t} \\ T(\vec{\mathrm{x}},0) &= T_0(\vec{x}) \end{aligned} \tag{4.1}$$

where K is the thermal conductivity, ρ is the density, c is the specific heat at constant pressure, and Q is the volumetric heat source with the unit $\mathrm{Js^{-1}m^{-3}}$. The above governing equations is used in the hot disk test.

If the problem under consideration is axisymmetrical the above partial differential equation can be simplified by using cylindrical radial coordinate as [184]:

$$\frac{1}{r}\frac{\partial}{\partial r}\left(r\frac{\partial T}{\partial r}\right)+\frac{Q}{K}=\frac{1}{\kappa}\frac{\partial T}{\partial t} \tag{4.2}$$

where $\kappa = K/\rho c$ is the thermal diffusivity. The Green's function corresponding to partial differential equation (4.2) is given as the following [184]:

$$G(r,t;r',t') = \frac{1}{4\pi\kappa(t-t')}\exp\left[-\frac{r^2+r'^2}{4\kappa(t-t')}\right]I_0\left[\frac{rr'}{2\kappa(t-t')}\right] \tag{4.3}$$

where $I_0(\bullet)$ is the Bessel function of first kind with zero order, i.e.:

$$I_0(x) = \frac{1}{2\pi}\int_0^{2\pi} e^{x\cos\theta}d\theta = \frac{1}{\pi}\int_0^{\pi} e^{x\cos\theta}d\theta \tag{4.4}$$

Note that $(Q_0/\rho c)G(r,t;r',t')$ represents the solution to an impulse point heat source of magnitude Q_0 at location r' and time t'. Q_0 represents the heat released per unit length at the point source, and its unit is $\mathrm{Jm^{-1}}$.

When the heat source is arbitrarily distributed in the material the solution can be expressed as the following by using the green function:

$$\begin{aligned} T(r,t) &= T_0 + \frac{\kappa}{K}\int_0^t\int_0^\infty Q(r',t')G(r,t;r',t')(2\pi r')dr'dt' \\ &= T_0 + \frac{\kappa}{K}\int_0^t\int_0^\infty \frac{Q(r',t')}{4\pi\alpha(t-t')}\exp\left[-\frac{r^2+r'^2}{4\kappa(t-t')}\right]I_0\left[\frac{rr'}{2\kappa(t-t')}\right](2\pi r')dr'dt' \end{aligned} \tag{4.5}$$

where T_0 is the initial temperature, and the unit of Q is $\mathrm{Js^{-1}m^{-3}}$.

4.2.1 Concentric ring heat source

When the material is continuously heated by a set of *n* concentric ring heat sources, $Q(r',t')$ can be expressed as the following [168]:

$$Q = Q_0 \sum_{i=1}^{n} \delta\left(r' - \frac{ia}{n} \right) H(t) \qquad (4.6)$$

assuming that n concentric ring heat sources are equally spaced, and that the largest radius of the rings has value a. As a result, the location of the ith ring is at ia/n, and the total length of the rings is $(n+1)\pi a$. $H(\bullet)$ is the Heaviside step function. The unit of Q_0 is $\mathrm{Js^{-1}m^{-2}}$. Substituting Eq. (4.6) for the heat source term $Q(r',t')$ in the general solution (4.5), we arrive at the solution to an infinite plane continuously heated by a series of equally spaced concentric rings,

$$T(r,t) = T_0 + \frac{Q_0 \kappa}{K} \sum_{i=1}^{n} \int_0^t \frac{1}{4\pi\kappa(t-t')} \exp\left[-\frac{r^2 + a_i^2}{4\kappa(t-t')} \right] I_0\left[\frac{r a_i}{2\kappa(t-t')} \right] (2\pi a_i)\, dt' \quad (4.7)$$

where $a_i = ia/n$.

With a change of variable $s^2 = \kappa(t-t')/a^2$, the solution can be simplified to:

$$T(r,\tau) = T_0 + \frac{Q_0}{K} \sum_{i=1}^{n} a_i \int_0^\tau \frac{1}{s} \exp\left[-\frac{r^2 + a_i^2}{4a^2 s^2} \right] I_0\left[\frac{r a_i}{2a^2 s^2} \right] ds \qquad (4.8)$$

where $\tau = \sqrt{\alpha t}/a$ is a normalized variable with unit 1. Note that $T(r,\tau)$ depends on thermal diffusivity κ only through the normalized parameter τ.

Averaging the temperature over the n concentric ring heat sources we get the average temperature increase over the ring as

$$\overline{\Delta T}(t,K,\kappa) = \frac{2\pi Q_0}{LK} \sum_{i=1}^{n} \sum_{j=1}^{n} a_i a_j \int_0^\tau \frac{1}{s} \exp\left[-\frac{a_i^2 + a_j^2}{4a^2 s^2} \right] I_0\left[\frac{a_i a_j}{2a^2 s^2} \right] ds \qquad (4.9)$$

where $L = (n+1)\pi a$ is the total length of the concentric rings. The above expression is a concise integral representation of the analytical. Using proper integration algorithm the above expression for average temperature can be numerically evaluated to desired accuracy.

4.2.2 Disk heat source

If the infinite media is continuously heated by a disk heat source of radius a, $Q(r',t')$ can be expressed as the following

$$Q = Q_0\left[H(r') - H(r'-a)\right]H(t) \tag{4.10}$$

here $H(\bullet)$ is the Heaviside step function and the unit of Q_0 is $\mathrm{Js^{-1}m^{-3}}$. The solution to an infinite plane continuously heated by a disk can be obtained by substituting Eq. (4.10) for the heat source term $Q(r',t')$ in the general solution (4.5),

$$T(r,t) = T_0 + \frac{\kappa}{K}\int_0^t\int_0^a \frac{Q_0}{4\pi\kappa(t-t')}\exp\left[-\frac{r^2+r'^2}{4\kappa(t-t')}\right]I_0\left[\frac{rr'}{2\kappa(t-t')}\right](2\pi r')\,dr'dt' \tag{4.11}$$

Then, the average temperature increase over the disk can be obtained as

$$\overline{\Delta T}(t,K,\kappa) = \frac{Q_0}{\pi a^2 K}\int_0^\pi\int_0^a\int_0^a E_1\left(\frac{r^2+r'^2-2rr'\cos(\theta)}{4a^2\tau^2}\right)rr'\,drdr'd\theta \tag{4.12}$$

where $\tau = \sqrt{\kappa t}/a$.

4.2.3 Nonlinear regression algorithm

In the above sections, the average temperature at time t_i over a series of concentric ring or disk heat source was analytically deduced as a nonlinear function of thermal conductivity K and thermal diffusivity κ, i.e. $\overline{\Delta T}\left(t_i;K,\alpha\right)$. The dependence of average temperature on time and thermal diffusivity κ is captured through the normalized parameter $\tau=\sqrt{\kappa t}/a$. It is noted that the above equations are derived for homogeneous materials, in which the material properties and parameters are spatially independent. In case of composites the material properties and parameters are spatially dependent, which affect the conduction of heat throughout the composite media. On the other hand, the average temperature over the heat source can also be measured by experimental methods like hot disk technique or be numerically simulated by finite element (FE) analysis. The analytical solution was deduced by assuming the material is homogeneous. For composite, however, the material is not homogeneous. Consequently the difference between the analytical solution and the experimental or numerical solution at time t_i can be expressed as

$$r_i=\overline{\Delta T}\left(t_i;K,\alpha\right)-\overline{\Delta T}_i \tag{4.13}$$

where the first term on the right hand side is the analytical solution, and the second term is experimental measured or numerically simulated value. As a result, the effective thermal conductivity K and thermal diffusivity κ of the composite can be estimated by minimizing the difference given by Eq. (4.13) at each time instance,

$$\begin{aligned} &minimize: \quad f(K,\kappa) = \frac{1}{2}\sum_{i=1}^{N} r_i^2 = \frac{1}{2}\|r\|^2 \\ &subject\ to: \quad K > 0, \kappa > 0 \end{aligned} \tag{4.14}$$

where $r = (r_1, r_2, \cdots, r_N)^T$. Furthermore, the specific heat c of the material can also be determined by $c = K/\kappa\rho$ if the density ρ is known. In this study, the second term in Eq. (4.13) will be simulated using finite element analysis by creating micromechanics models of composite material. The material constants of individual composition of the composite serve as input for the FE simulation. The minimization problem Eq. (4.14) was solved by Gaussian-Newton method [185].

4.3 Sensitivity study

An important issue related to the estimation of the material constants K and κ is their sensitivity to the change of input data, which shows the effect of small perturbations in input data (here are the simulated average temperatures over the heat source by FE analysis) on the estimated parameters. With perturbations in the input data the estimation of the thermal conductivity K and thermal diffusivity κ can be restated as the following minimization problem,

$$minimize: \quad f(K,\kappa;\vec{\chi}) = \frac{1}{2}\sum_{i=1}^{N} r_i(K,\kappa;\chi_i)^2 = \frac{1}{2}\|r\|^2 \tag{4.15}$$

where $\vec{\chi}$ is a vector of perturbations in the input data. As shown in [186] the sensitivity of the local minimizer $\vec{x}^* = (K^*, \kappa^*)$ with respect to the perturbation vector $\vec{\chi}$, evaluated at the base case $\vec{\chi} = 0$, can be calculated by:

$$\frac{\partial \vec{x}^*}{\partial \vec{\chi}}(\vec{\chi}=0) = -\left[\nabla^2_{\vec{x}\vec{x}} f\left(\vec{x}^*;\vec{\chi}=0\right)\right]^{-1} \bullet \nabla^2_{\vec{x}\vec{\chi}} f\left(\vec{x}^*;\vec{\chi}=0\right) \tag{4.16}$$

In this study, the perturbation to the average temperature is assumed to be constant at each time t_i,

$$r_i(K,\alpha) = \overline{\Delta T}(t_i;K,\alpha) - \left(\overline{\Delta T_i} + \chi\right) \tag{4.17}$$

where χ is the error in the simulated temperature from the finite element analysis. Here the error is assumed to be the same at each time instance. Then the sensitivity coefficients of the estimated parameters K^*, κ^* to χ can be calculated by plugging Eq. (4.17).

Table 4.1 Thermal properties and density for $BaTiO_3$ and Ag.

	Thermal conductivity (W/m.K)	Thermal diffusivity (mm^2/s)	Density (g/cm^3)	Heat capacity (J/g.K)
$BaTiO_3$[a]	3.672	1.438	6.02	0.424
Ag[b]	419.0	166.3	10.5	0.24

[a]: [182]

[b]: [176, 177]

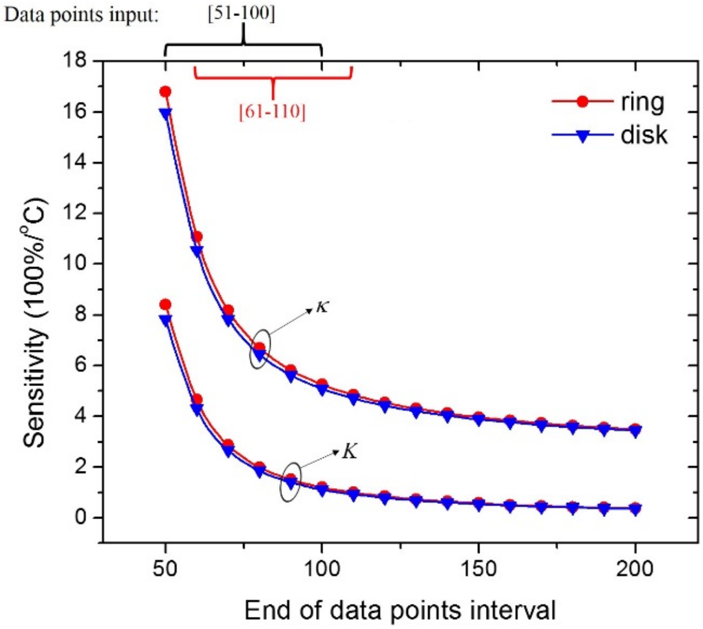

Figure 4.1 Sensitivity coefficients of material parameters estimation for monolithic $BaTiO_3$ ceramic. Note that 50 data points were used in the estimation. For example, the estimations at point 100 utilized the 51th to 100th data points.

In this study, the side length of the computational domain L equals to 30 mm, while the largest radius of the concentric ring heat source or the radius of the disk heat source equals to 3.189 mm. They were selected to approximate the experiment conditions that were conducted in [182]. The range of the computational time for the finite element simulation is selected to make sure that the transient heat transfer did not reach the boundary of the computational domain. The computational time was uniformly divided into 200 intervals, out of which 50 data points were used to estimate the two independent material parameters K and κ. For example, the estimations in Figure 4.1 at point 100 utilized the 51th to 100th data points, while estimations at point 110 used the 61th to 110th data points. Sensitivity analysis were carried out for both ring-shaped heat sources and disk-shaped heat sources. The ring shaped heat source includes 20 equally spaced concentric rings with a largest radius of 3.189 mm. The width of each ring in the finite element models was very small, i.e. 30 μm. The thermal properties and densities of $BaTiO_3$ and silver are listed in Table 4.1.

The effects of small perturbation in the input data on the estimated material parameters of monolithic $BaTiO_3$ ceramic are shown in Figure 4.1. The sensitivity coefficients are the normalized values, i.e. $\left(1/K^*\right)\bullet\left(\partial K^*/\partial\chi\right)$ and $\left(1/\kappa^*\right)\bullet\left(\partial\kappa^*/\partial\chi\right)$, instead of $\partial K^*/\partial\chi$ and $\partial\kappa^*/\partial\chi$. The sensitivity coefficients of the estimated material parameters become smaller as the input data points interval moves to larger time instances. The sensitivity coefficients tend to become constant as indicated by the almost flat trail in the plot. Consequently, to improve the accuracy of the parameters estimation, under the premise that the heat conduction does not reach the computational boundary, data points from larger time instances should be used. It is clear that the estimation of thermal diffusivity κ is more sensitive to the input data than the estimation of thermal conductivity K, which means the estimation precision of effective thermal conductivity is higher than that of thermal diffusivity. In addition, the sensitivity coefficients for ring-shaped heat source is very close to that for disk-shaped heat source, which indicates that 20 concentric rings can accurately approximate the disk geometry.

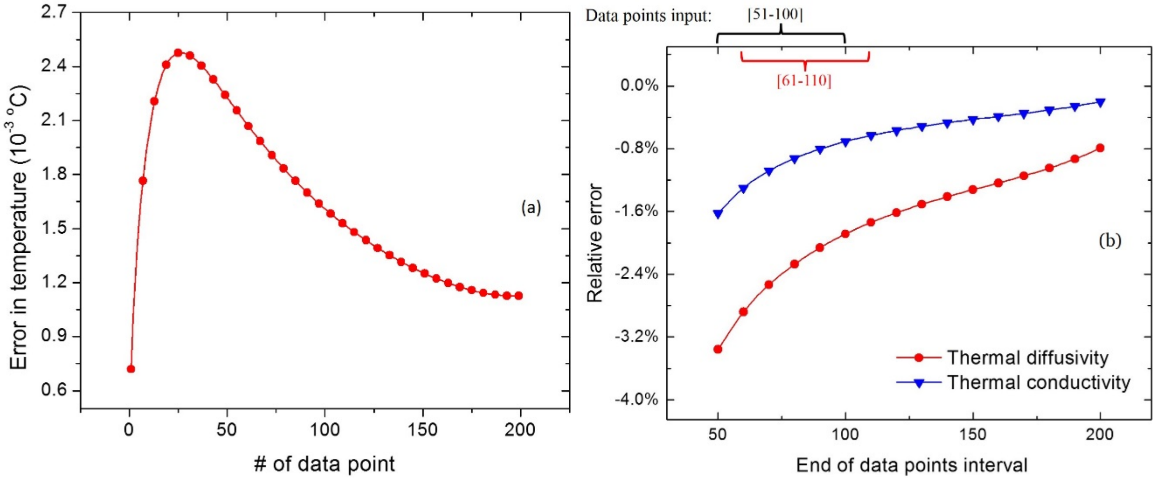

Figure 4.2 (a) Actual absolute error in the finite element simulated average temperature over disk heat source for pure BaiTiO$_3$ at each time instance; (b) the corresponding relative errors in estimated material parameters.

The actual absolute errors in the finite element simulated temperature averaged over the disk-shaped heat source for a typical computational model are plotted in Figure 4.2 (a) for monolithic BaTiO$_3$ ceramics at each time instances. The absolute error in temperature tends to decrease at larger time instances, except at several time instances in the beginning. The corresponding relative errors in estimated thermal conductivity and thermal diffusivity are plotted in Figure 4.2 (b). The relative errors significantly decrease as data points at larger time instances were used for input. It can be noted that the relative error for the estimated thermal conductivity is obviously smaller than that for the estimated thermal diffusivity, due to its less sensitive response to the perturbation in the input data. This observation will further be validated in the following section by the fact that the relative standard deviation of estimated thermal diffusivity is larger than that for estimated thermal conductivity. The smallest relative error is -0.20% and -0.79% for estimated thermal conductivity and thermal diffusivity, respectively.

In summary, to minimize the error in the estimated thermal properties, results of the sensitivity analysis suggest that if the computational boundary is not reached by the heat transfer during the computational time, data points from larger time instances should be used as the input. Furthermore, this analysis also shows that 50 data points is enough to lead to a relative small estimation error.

4.4 Effects of heat source geometry and particle size

In the finite element analysis the concentric rings heat source were approximated by rings with small finite width. Consequently, the computational area around the rings needs to be very finely meshed to capture its characteristics, which also might result in distorted elements. As shown in the previous sections, the sensitivities of estimated parameters to small perturbations in input data are very close to each other for both ring-shaped and disk-shaped heat sources. Consequently, computational geometry with disk-shaped heat source might be a better candidate for computational purpose. In this section the effective thermal conductivity K and thermal diffusivity κ for Ag/BaTiO$_3$ composite with 20 vol% of silver were estimated based on the finite element simulated temperatures over ring-shaped and disk-shaped heat sources, respectively. The estimated effective material parameters were then compared to study the influence of heat source geometry. Another important issue is how many reinforcement particles should be generated in the micromechanical models in order to obtain effective properties that are able to represent the corresponding macroscopic properties of the composites. If the number of reinforcement particles in the micromechanics model is too small the predicted effective material constants would not only be inaccurate but also have larger dispersions. On the other hand, finer mesh, and thus larger computational time, would be required if more reinforcement particles were included. In this section the convergence behavior of the model as the of particle size decrease were investigated to provide results for selecting a suitable number of reinforcement particles.

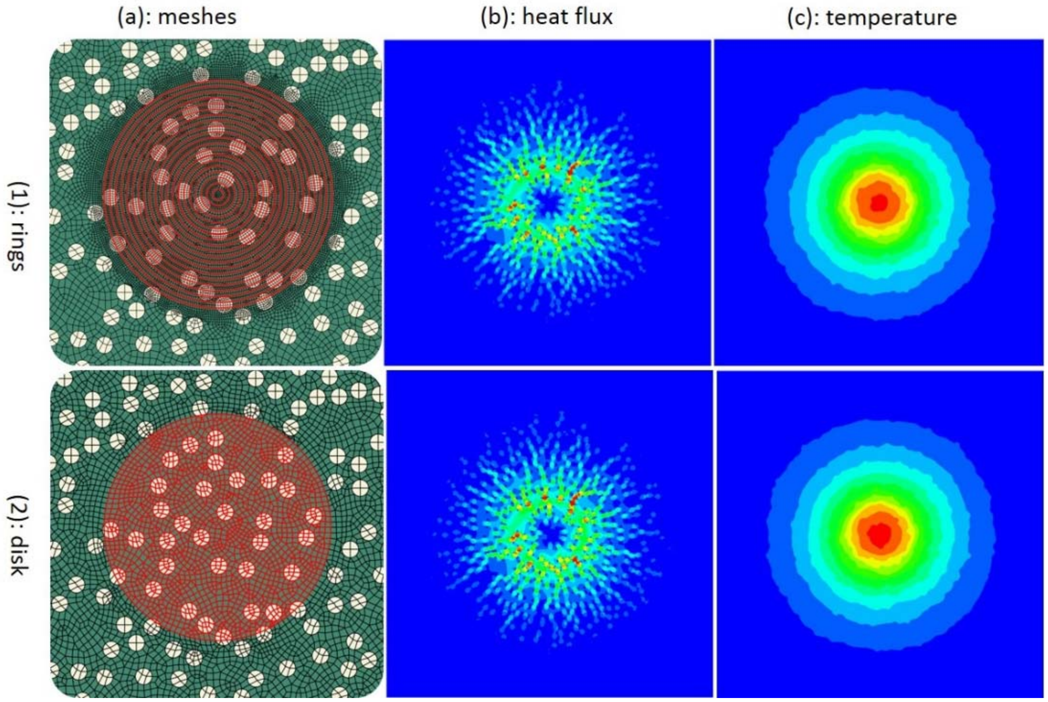

Figure 4.3 Effects of heat source geometry on the heat flux and temperature profile at t=20s for 20 vol% Ag/BaTiO$_3$ composite.

Table 4.2 Comparison of estimated material parameters between ring-shaped heat source and disk-shaped heat source.

	ring	disk	relative difference
K (W/mK)	5.5296±0.37%	5.5290±0.37%	0.01%
κ (mm^2/s)	2.0521±0.97%	2.0486±0.85%	0.17%

The heat flux and temperature profiles at t=20s for 20 vol% Ag/BaTiO$_3$ composite are shown in Figure 4.3 to study the influence of heat source geometry. Note that to show the heat source geometry and meshes clearly only part of the micromechanics model is shown in column (a) of the figure. 1000 particles are included in the micromechanics models. A mesh size was selected to ensure that each silver particle consists of at least four elements. Meshes were refined around the heat sources to capture the detailed geometry and to improve the precision. It is clear from meshes in column (a) that the meshes around the ring-shaped heat source were much denser than that around the disk-shaped heat source. Columns (b) and (c) show that the heat flux and temperature profiles are almost identical for the two different heat source geometries. The estimated thermal conductivity and diffusivity are listed in Table 4.2. Three micromechanics models were generated to improve the accuracy and to calculate the standard deviations. The relative differences for estimated material properties between the two types of heat source geometries, as shown in Table 4.2, are very small, i.e. 0.01% and 0.17% for thermal conductivity and thermal diffusivity, respectively. Furthermore, the standard deviations are also very close. Therefore, all following calculation were carried out using the disk-shaped heat source due to its computational efficiency.

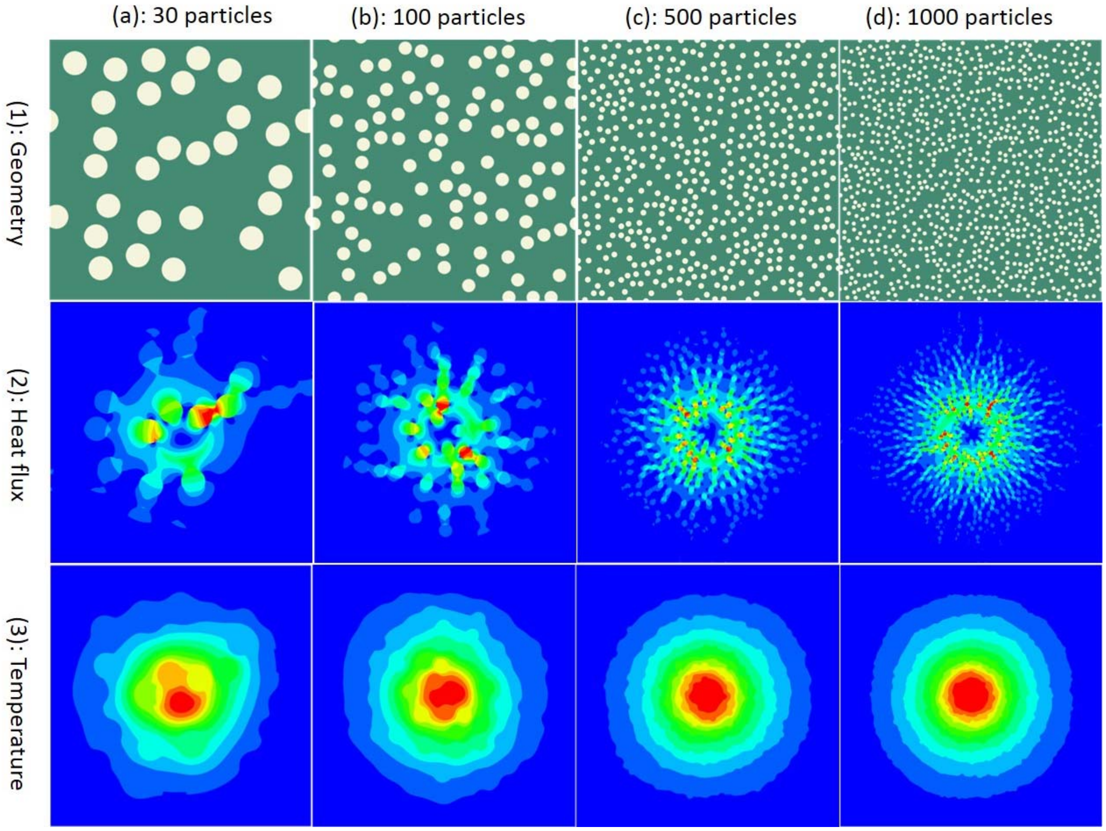

Figure 4.4 Effects of particle size on the heat flux and temperature profile at $t = 20s$ for disk-shaped heat source.

The heat flux and temperature profiles for different particle sizes for 20 vol% Ag/BaTiO$_3$ composite are shown in Figure 4.4 for disk-shaped heat source geometry. Four different particle size were studied, i.e. 30, 100, 500, and 1000 Ag particles pre model at the constant volume fraction of 20 vol%. As shown in [182], micromechanics models based on steady state heat transfer analysis of microstructure with 30 particles are enough to give relative small standard deviation for effective thermal conductivity prediction. For micromechanics models based on transient heat transfer analysis, however, as shown in Figure 4.4 column (a) the heat flux and temperature profiles are not radially symmetry and highly distorted. The unsymmetrical profiles were reduced with the increase of particle numbers. The heat flux and temperature profiles for models with 500 and 1000 particles are almost identical with approximately isotropic and circular envelope lines, which indicates that convergence has been achieved.

Table 4.3 compares the effective thermal conductivities predicted from steady state and transient heat transfer analysis for different number of reinforcement particles in the constant volume fraction of silver particles. Table 4.3 shows that as the particle size decrease, i.e. as particle number increases from 30 to 1000, the relative differences between predictions based on steady state and transient analysis significantly decreases. Very close predictions are given by steady state and transient analysis for micromechanics models with 500 or 1000 particles. Figures 4.5 shows the relative standard deviations for the predicted thermal properties of Ag/BaTiO$_3$ composite. Each standard deviations were calculated based on three micromechanics models. Relative standard deviation is defined as the ratio of standard deviation to the magnitude of the related parameter. For example, the relative standard deviation for thermal conductivity K is

$$relative\ standard\ deviation\ of\ K = \frac{standard\ deviation\ of\ K}{K} \tag{4.18}$$

The relative standard deviations rapidly drops for predictions using transient analysis and reaches convergence for particle number around 500. On the other hand, the relative standard deviation for steady state prediction is already very small for 30 particle models. Consequently, to estimate the effective thermal properties with good accuracy transient analysis needs more particles in the micromechanics models. Furthermore, the relative standard deviation of effective thermal conductivity prediction is smaller than that of effect thermal diffusivity, which means that the prediction for thermal conductivity has higher accuracy. Micromechanics models with 500 particles will be selected in the following predictions.

Table 4.3 Comparison of thermal conductivity K estimated by steady state and transient analysis.

K, conductivity (W/mK)	p=30	p=100	p=500	p=1000
steady state	5.5355	5.5792	5.5135	5.5256
transient	5.4641	5.5885	5.4901	5.5290
relative difference	1.29%	0.17%	0.42%	0.06%

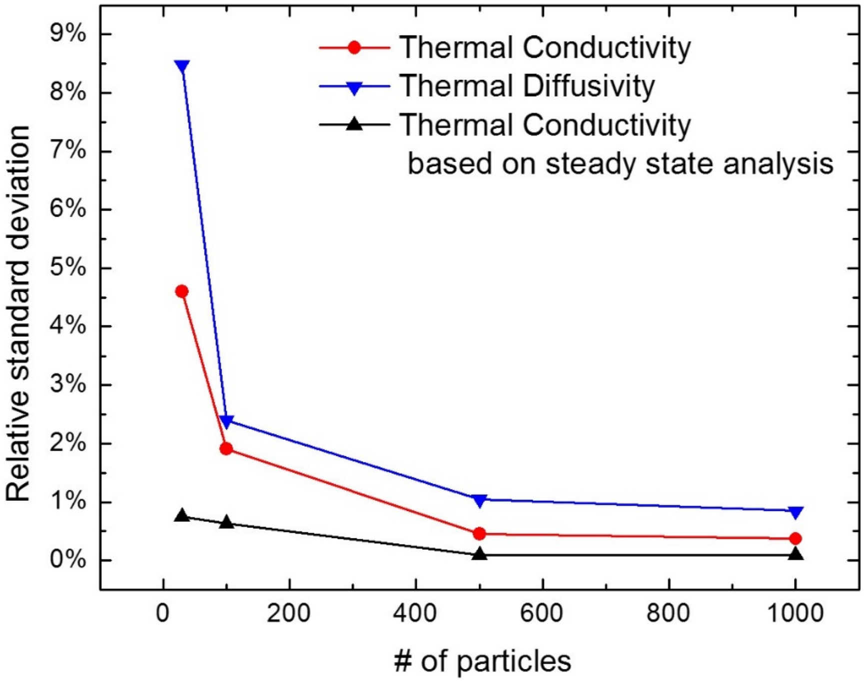

Figure 4.5 Relative standard deviation as a function of particle size for Ag/BaTiO$_3$ composite.

4.5 Results and discussion

In [182] micromechanics models based on steady state heat transfer analysis were considered to predict the effective thermal conductivity of Ag/BaTiO$_3$ composite. However, one drawback of steady state method is that effective thermal diffusivity and heat capacity cannot be estimated simultaneously. In this section the effective thermal conductivity, together with effective thermal diffusivity and heat capacity, of Ag/BaTiO$_3$ composites were predicted by micromechanics models based on transient heat transfer analysis developed in this study and described in the previous sections. The results are then compared to both experiment results and predictions from steady state analysis, when available.

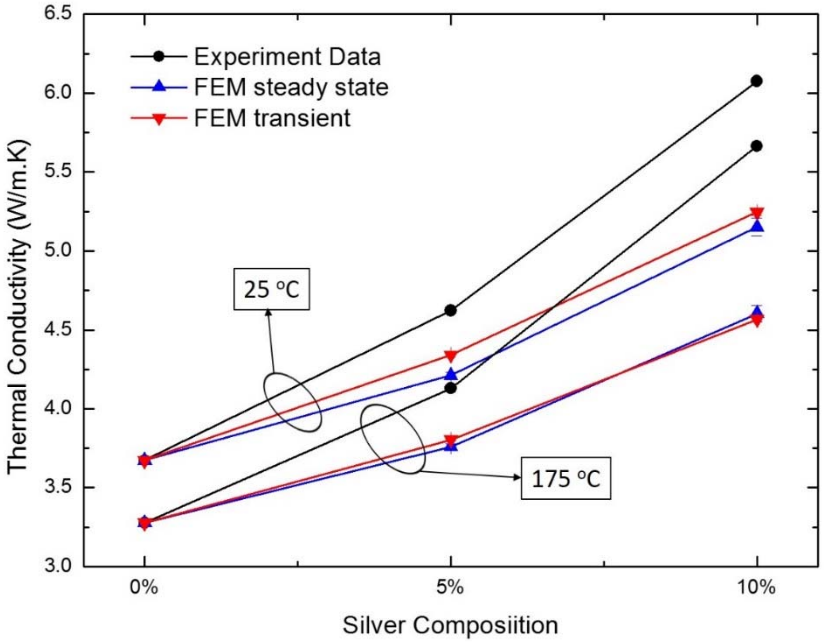

Figure 4.6 Comparison of experimental results with the effective thermal conductivity predicted by micromechanics models based on steady state and transient analysis.

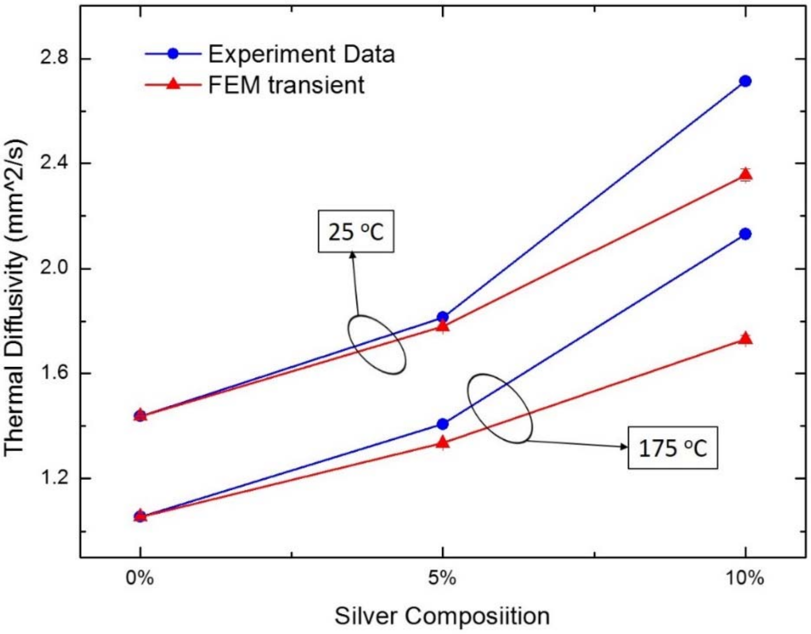

Figure 4.7 Comparison of experimental results with the effective thermal diffusivity predicted by micromechanics models based on transient analysis.

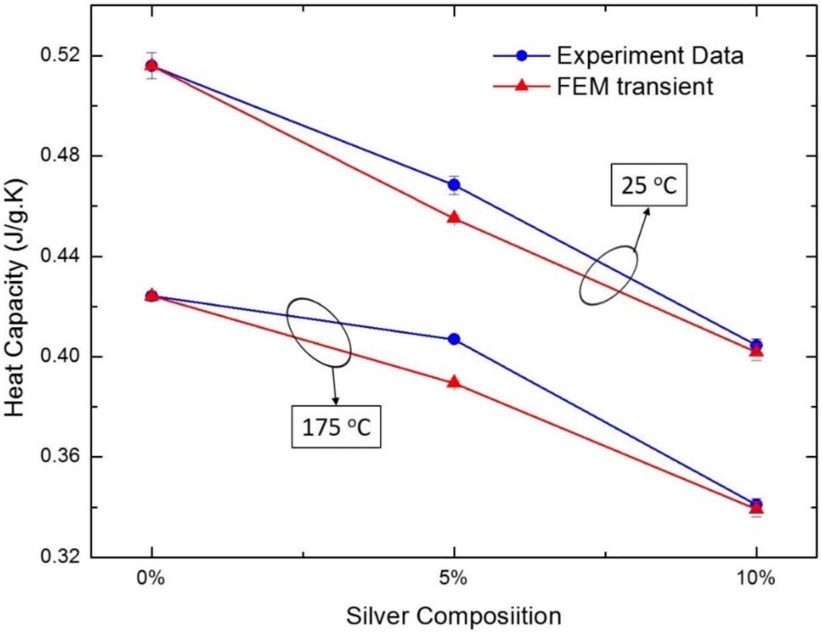

Figure 4.8 Comparison of experimental results with the effective heat capacity predicted by micromechanics models based on transient analysis.

Figure 4.6 shows the effective thermal conductivity predicted by micromechanics models based on the transient heat transfer analysis, as a function of silver composition. For comparison, experimental results and predictions based on the steady state heat transfer analysis from [182] were also plotted in the same figure. The difference between predictions based on the transient and steady state analyses is relative small. The predictions from the micromechanics analysis underestimate the experimental data. For the 5 vol% composite, the predictions underestimate the experiment results about 6.13% and 7.84% at 25 ^{o}C and 175 ^{o}C, respectively, while for 10 vol% composite underestimation reaches 13.66% and 19.35% at same temperatures. The underestimation increases with increasing the silver content. As explained in [182] one possible reason might be the high contrast in thermal conductivity between silver and $BaTiO_3$. Figure 4.9 shows that the heat flux concentration for composites with 10 vol% silver is higher than the one with 5 vol% silver.

The comparison of the effective thermal diffusivity predicted by the micromechanics models based on transient analysis and experimental results are shown in Figure 4.7. As in the case of effective thermal conductivity, the predictions underestimate experimental results. For 5 vol% composite, the values of thermal diffusivity are lower than experimental ones for 1.95% and 5.16% at 25 ^{o}C and 175 ^{o}C, respectively. For 10 vol% they are lower for 13.19% and 18.80% respectively. Again, the underestimation for 10 vol% composite is much larger than that for 5 vol% composite. Figure 4.8 compares the experimental measured heat capacity to that predicted using transient heat transfer micromechanics model for different silver compositions. For the effective heat capacity, the underestimation is relative small. For 5 vol% composite, the predictions underestimate the experiment results for about 4.26% and 2.82% at 25 ºC and 175 ºC, respectively, while for 10 vol% composite the underestimations are 0.54% and 0.67% respectively.

The profiles of heat flux and temperature were shown in Figure 4.9 for 0 vol%, 5 vol% and 10 vol% Ag/$BaTiO_3$ composites. Note that the heat transfer did not reach the boundary at t=20s, which is important because the analytical solution assumes an infinite large geometry. The largest magnitude of heat flux happens at some of the silver particles shown as red dots in Figure 4.9 because silver has a much larger thermal conductivity than $BaTiO_3$ matrix. The areas of the heat flux concentrations in 10 vol% seems to be more numerous than in 5 vol% composite. Furthermore, at each time, the distance that heat has transferred through the composite is larger in 10 vol% composite when compared to the 5 vol% one. The circular envelope lines of heat flux and temperature profiles indicate that the micromechanics models leads to the macroscopically isotropic response. However, the heterogeneity in the material is shown by the flux field not smoothly distributed for 5 vol% and 10 vol% composites, compared to the flux filed in homogeneous materials (Figure 4.9 (a)). In determining the effective properties of composites, this distribution is spatially averaged. The magnitude of highest temperature is slightly smaller in 10 vol% composite when compared to 5 vol% composite, because the larger amount of silver particles in 10 vol% makes heat transfer easier.

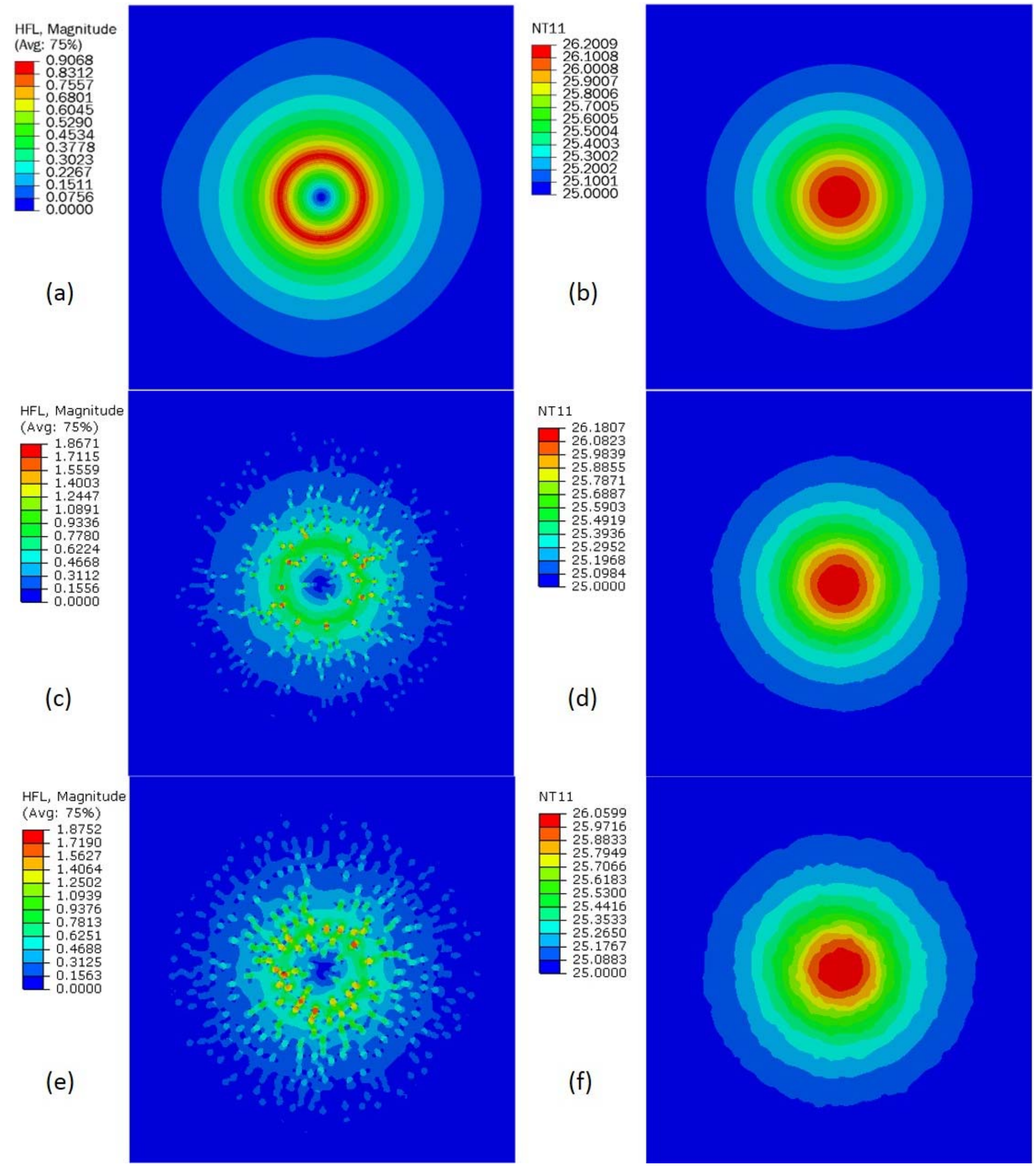

Figure 4.9. Heat flux and temperature profile for Ag/$BaTiO_3$ composite at t=20s: (a), (c), (e) heat flux for 0 vol%, 5 vol% and 10 vol%; (b), (d), (f) temperature for 0 vol%, 5 vol% and 10 vol%.

CHAPTER V

ELASTIC AND DIELECTRIC PORPERTIES OF ACTIVE AG/BATIO$_3$ COMPOSITE

5.1 Introduction

Barium titanate ($BaTiO_3$) as an electro-active ceramic has many engineering applications. For example, it has been used extensively in electronic industry like multilayer ceramic capacitors (MLCCs) because of its high dielectric constants [1]. Due to their high capacitance, relatively small size, and good reliability MLCCs are the key components in electronic devices nowadays. Barium titanate based ceramics are also preferred for actuators and sensors because it is lead free which is an advantage over other piezoelectric materials such as lead ziconate titanate (PZT) [4]. It also has a relative high permittivity. However, barium titanate is extremely brittle which greatly impedes its further applications. In order to improve its ductility and fracture toughness barium titanate has been blended with metallic or polymeric material to form a composite [7, 10, 11, 72]. Compared to monolithic ceramic, adding metal or polymer greatly enhances its ductility and fracture toughness. On the other hand, the introduction of metal phase significantly increases the dielectric constant of the composite, because the metallic particles can form internal electrodes within the ceramic [72].

In this study, we experimentally measured the elastic constants and dielectric properties of Ag/$BaTiO_3$ composite by using resonant ultrasound spectroscopy (RUS) technique and dielectric (impedance) spectroscopy, respectively. Furthermore, micromechanics models were constructed to understand the effect of microstructures on the overall elastic and dielectric properties of composites and numerically predict the effective properties of the composite. The micromechanics models are based on detailed microstructures either randomly generated by computer algorithm or from realistic SEM images. The predicted effective constants were then compared to the experimental results.

5.2 Experiment procedures

5.2.1 Resonant ultrasound spectroscopy

Resonant ultrasound spectroscopy (RUS), a dynamic technique, is a nondestructive method to measure the elastic constants of materials at various ambient temperatures. Compared to other techniques, it has the advantages of easy sample preparation, and measurements over the wide range of measuring temperatures of the entire scalar components of the elastic tensor using only one sample [82, 128, 129, 187, 188]. The geometry of Ag/$BaTiO_3$ composite used in this study was cylindrical with a diameter of ~18.5mm and a height of ~9.6mm. To ensure the repeatability of the measurements two specimens were tested for each composition. Since the grains of Ag/$BaTiO_3$ in the polycrystalline composite samples were randomly oriented, its material symmetry was assumed to be isotropic with only two independent scalar components of its elastic tensor(i.e. C_{11} and C_{44}), from which the well-known elastic constants Young's modulus, shear modulus and Poisson's ration were calculated. The nonlinear regression fitting algorithm was carried out using the commercial software Quasar RuSpec (Magnaflux Quasar Systems, Albuquerque, NM) which iteratively minimizes the root mean square error between analytically calculated and experimentally measured resonant frequencies of the specimen. An initial guess for the C_{11} and C_{44} is needed to feed to the nonlinear regression fitting algorithm as the starting point, which is selected from the previously reported values for pure barium titanate ceramic in literature.

5.2.2 Relative permittivity and dielectric loss

The dielectric constants in this study was measured by a dielectric (impedance) spectroscopy (Novocontroal America, INC). During the measurement the sample is mounted in a sample cell between two electrodes forming a capacitor. The sample voltage and current were then recorded, from which the various dielectric properties of the material can be calculated. The diameter of the sample for this testing was about 20 mm with a thickness between 1.5 mm to 2.0 mm. Top and bottom surfaces of the sample were carefully polished to make them parallel and smooth. Silver electrodes with a diameter of 16 mm were coated on these two surfaces and then burned at 150 °C for 2 hours. The control variables for the testing were frequency and temperatures. The frequency range selected varied 10^{-2} to 10^{7} Hz in the temperature range from -50 °C to 200 °C. This temperature range is selected to capture effects of two phase transformations that happen around 0 °C and 120 °C, respectively. We investigate the dielectric response of the composite samples near these phase transformation temperatures, as a sharp increase in the dielectric constant around the phase transformation temperature was expected. In order to better capture these sharp increases in the relative permittivity more temperature points were sampled around 0 °C and 120 °C in this study.

5.3 Experimental results

5.3.1 Elastic constants

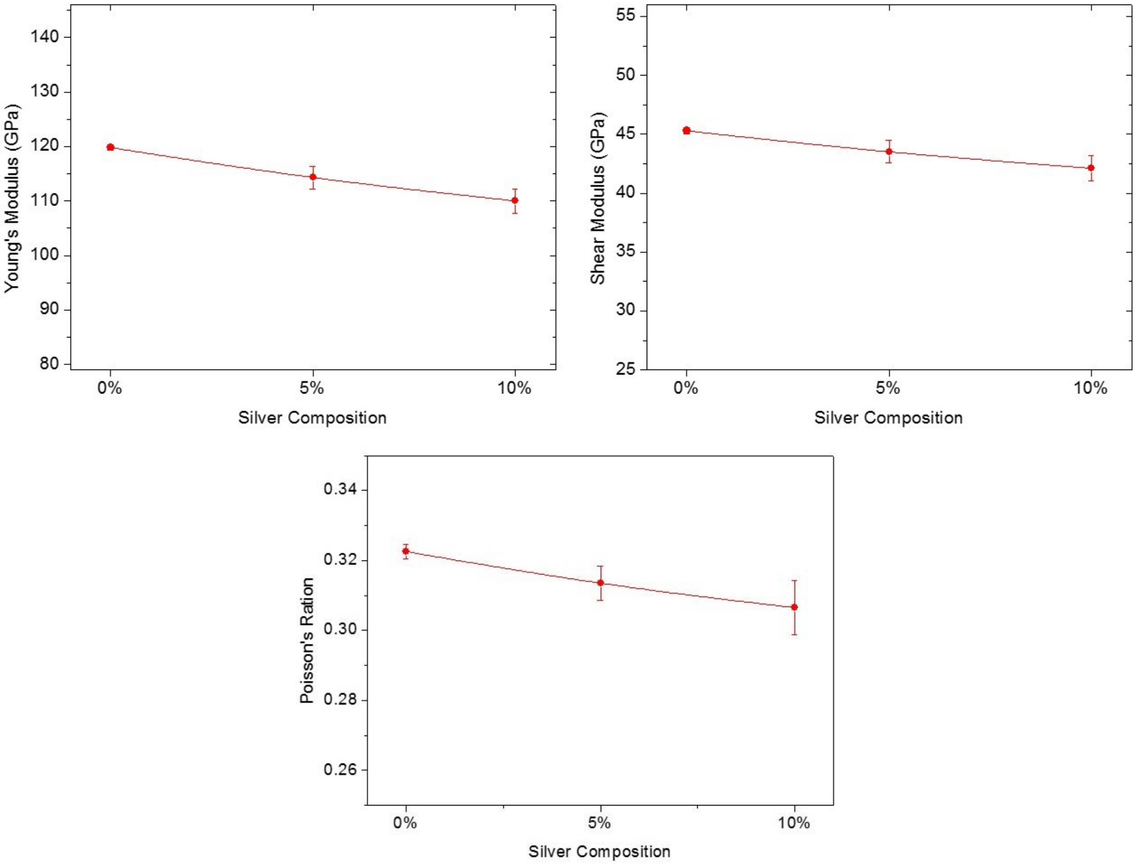

Figure 5.1 Young’s modulus, shear modulus, and Poisson’s ratio as a function of silver composition at room temperature, tested by RUS technique.

The elastic constants at room temperature, tested by resonant ultrasound spectroscopy, of Ag/BaTiO$_3$ composite are plotted in Figure 5.1 for different silver contents. Blending silver phase into barium titanate ceramic decreases its Young’s modulus because silver is softer. For example, the Young’s modulus of pure barium titanate ceramic is 119.81 GPa while 110.04 GPa for 10 vol% composite. Increase of silver content in the composite also decreases its shear modulus and Poisson's ratio. The standard error of testing results at higher silver composition is larger, which might be due to the dispersion of microstructures introduced by blending a silver phase. Compared to the experimental values reported in literature for pure barium titanate ceramic, the Young's modulus measured in this work, i.e. 119.81 GPa, is within the range of values reported earlier, i.e. ~107 GPa [178] and 128 GPa [189]. The differences might be due to different porosities and testing techniques used in different studies. Also, as shown in [178] pure barium titanate ceramics with finer grain has a relatively lower Young's modulus.

5.3.2 Relative permittivity and dielectric loss

The relative permittivity (ε_r') and dielectric loss (tanδ) as a function of frequency are plotted in Figure 5.2 for monolithic $BaTiO_3$ ceramic and for 5 vol% Ag/$BaTiO_3$ composite. In general, the relative permittivity increases as the operating frequency decreases because lower frequency gives more time to electric dipoles to respond to the applied external electrical stimuli. However, at higher frequency range, above 1 KHz, the dielectric constants are almost constant. With increasing operating frequency, the dielectric loss first increases up to 1 KHz and then decreases afterwards. The trends of relative permittivity and dielectric loss as a function of frequency for monolithic $BaTiO_3$ ceramic and 5 vol% Ag/$BaTiO_3$ composite are similar. The dielectric constants of 5 vol% Ag/$BaTiO_3$ are much higher than those of pure $BaTiO_3$, especially at lower frequencies. For example, the relative permittivity for monolithic $BaTiO_3$ ceramic at 1 KHz is 1776.05 while it is 2677.05 for 5 vol% Ag/$BaTiO_3$

composite; this is a 50.73% increase. Such a significant increase is because the silver particles are conductive and serves as internal electrodes which redistribute and enhance the local electrical filed under fixed applied external electrical potential [72]. At lower frequency conductive silver particles have more time to sufficiently redistribute the local fields which leads to a larger increase in the dielectric constants. On the other hand, increasing silver contents only slightly increases the dielectric loss in the composite. The relative permittivity and dielectric loss are sensitive to the microstructure of the samples as shown by the relatively large error bars in Figure 5.2. Generally, they strongly depend on the impurity, defects, and grain size of the samples [24]. The relative permittivity of monolithic $BaTiO_3$ ceramics measured in this work at room temperature and around Curie temperature are given in Table 5.1 and compared with previously reported values in the literature. Previously reported values in the literature have very large variations among the samples prepared using different synthesis processes. It is noted that the dispersion of dielectric constants at Curie temperature is much larger than that at the room temperature. The measured values in this work fall in the range reported in literature.

Table 5.1 Comparison of relative permittivity with values in literature at 1 KHz.

Relative permittivity	Room temperature	Curie temperature
Previously reported values[a]	1700 ~ 5000	2840 ~ 10000
This work	1720	7040

[a]: [90-96]

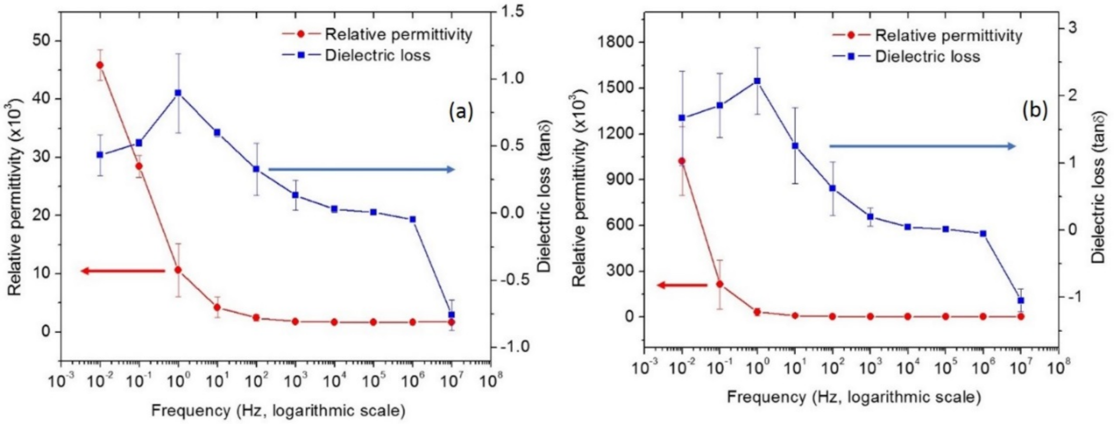

Figure 5.2 Relative permittivity (ε_r') and dielectric loss (tanδ) as a function of frequency at room temperature: (a) monolithic $BaTiO_3$ ceramic; (b) 5 vol% Ag/$BaTiO_3$ composite.

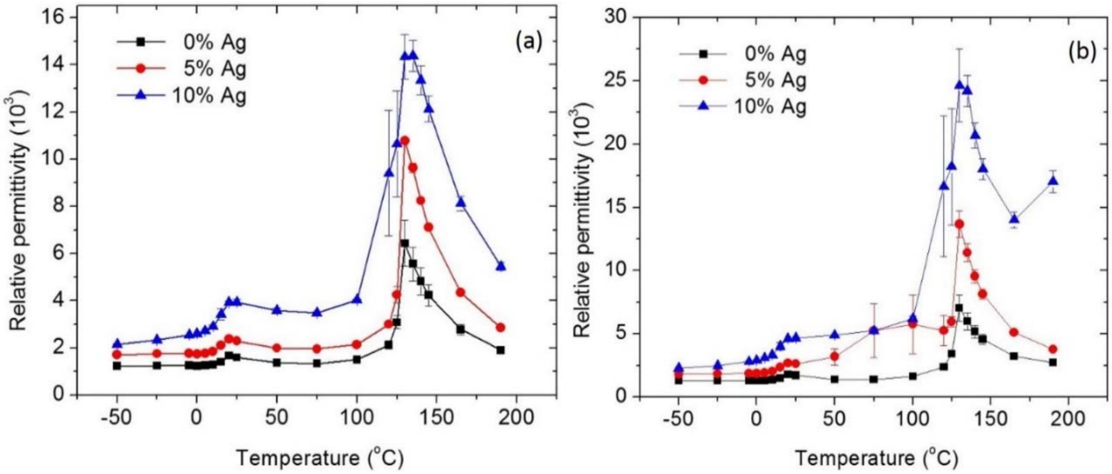

Figure 5.3 Relative permittivity as a function of temperature for varying silver compositions: (a) at 1 MHz; (b) at 1 KHz.

The relative permittivity as a function of temperature for varying silver compositions are plotted in Figure 5.3. The most significant features shown in these plots are the peaks around phase transformation temperatures, i.e. around 0 °C and 120 °C. The dramatic increases in dielectric constant near phase transformation temperatures were previously reported in literature [190] for monolithic $BaTiO_3$ ceramic. The peak at tetragonal to cubic phase transformation temperature (Curie temperature) is much sharper than that at orthorhombic to tetragonal phase transformation temperature, similar to previously reported results in [190]. Away from these phase transformation temperatures, the dielectric constants stay almost constant. With respect to Ag /$BaTiO_3$ composites Figure 5.3 shows that the trends for the relative permittivity as a function of temperature are similar to that for monolithic $BaTiO_3$ ceramic. Adding silver into $BaTiO_3$ greatly increases its dielectric constant, as shown for both 1 MHz and 1 KHz frequencies. Figure 5.3 shows that the standard deviation of measured relative permittivity is much larger for Ag/$BaTiO_3$ composites with higher silver content. One possible reason is the differences in the degree of percolated metallic particles in individual sample [72]. Furthermore, since the dielectric constant is extremely sensitive to the impurity, defects and grain sizes, a subtle change in the microstructure for individual samples can lead to large variation of measured values. The relative permittivity does not increase linearly as a function of silver content, as shown in Figure 5.4. At higher silver composition the effect of a certain amount silver increase on the dielectric constant increase is much more significant than that at lower silver compositions. One possible explanation for this phenomenon is the formation of electrical conductive chains by conductive silver particles and the fact that conductive silver particles serve as internal electrodes in the ceramic. As the increase of silver volume fraction they tend to become more clustered and form electrical "bridges", which greatly increase the internal electric field in the ceramic. At the extreme case, the silver particles would be connected to make the ceramic conductive.

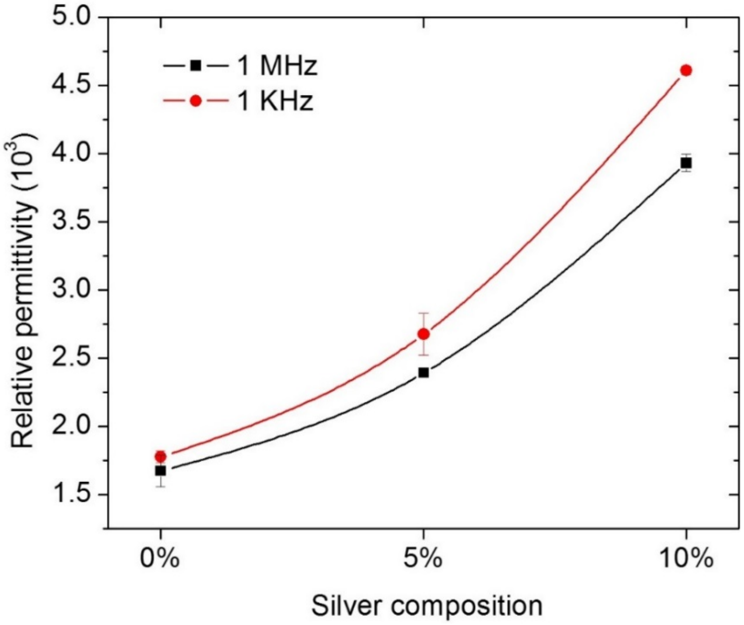

Figure 5.4 Relative permittivity as a function of silver composition at room temperature.

5.4 Micromechanics model predictions based on finite element analysis

Micromechanics models were generated to predict the effective elastic and dielectric properties of Ag/$BaTiO_3$ composites. Two different micromechanics models were considered. The first one is based on the realistic microstructures of the composite which is obtained from the scanning electronic microscopy (SEM) images. Different phases in the SEM images were distinguished by the open source software OOF. The second micromechanics model is based on microstructures that were created by randomly generating silver particles in the barium titanate matrix. To improve the reliability of the microstructures, representations of four models were generated for each 2D micromechanics model based on SEM images (refer to [182] for the details of micromechanics generation). Finite element (FE) analysis using commercial software ABAQUS were carried out for the micromechanics analyses, which were used to obtain the effective properties of the composite. A selected but typical microstructure of 2D FE models for 10 vol% Ag/BaTiO$_3$ composites was shown in Figure 5.5, together with an enlarged meshes for the part of the SEM image.

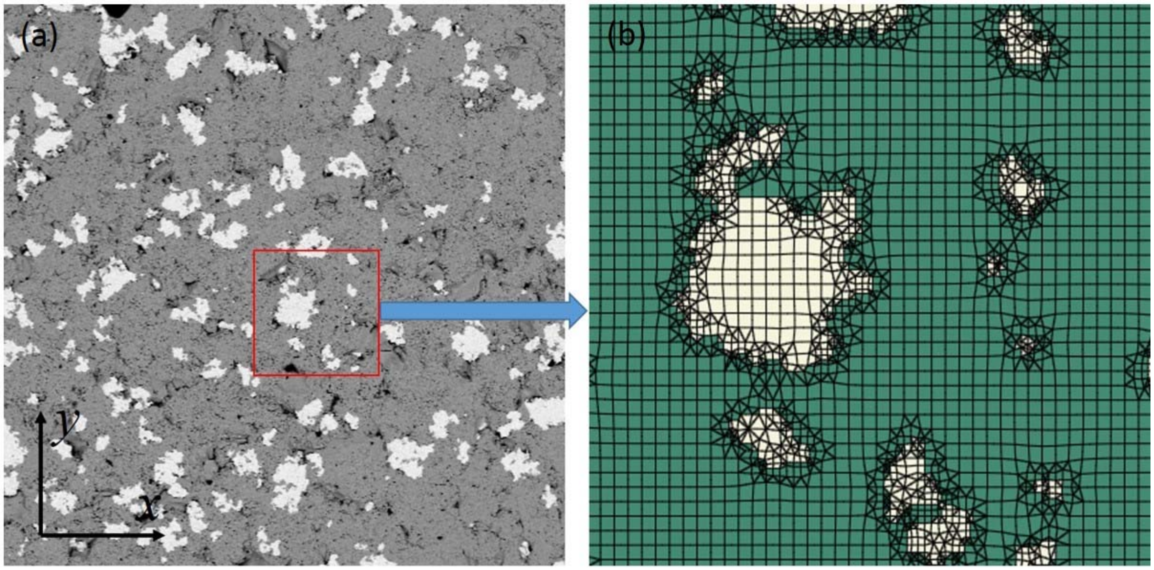

Figure 5.5 Selected but typical microstructure of 2D FE models for 10 vol% Ag/BaTiO$_3$ composites: (a) SEM image with size 547 x 547 mm; (b) enlarged meshes of part of the image.

In order to predict the effective elastic constants, the following mechanical boundary conditions (BCs) and constraints on the 2D micromechanics models are considered,

$$\begin{aligned} u_x(0,y)=0, u_x(L,y)=u_{right}, 0\le \mathrm{y}\le L \\ u_y(\mathrm{x},0)=0, u_y(\mathrm{x},L)=u_{top}, 0\le x\le L \end{aligned} \tag{5.1}$$

where L is the side length of the 2D model. The right and top edges of the model were constrained to deform in a straight line. A small traction was applied on the right or top edge, say $\sigma_{xx} = \sigma_0$ on the right edge. Consequently,

$$\begin{gathered} \bar{\varepsilon}_{xx} = \frac{u_{right}}{L}, \bar{\varepsilon}_{yy} = \frac{u_{top}}{L} \\ \bar{E} = \frac{\sigma_{xx}}{\bar{\varepsilon}_{xx}}, \bar{v} = \frac{\bar{\varepsilon}_{xx}}{\bar{\varepsilon}_{yy}}, \bar{G} = \frac{\bar{E}}{2(1+\bar{v})} \end{gathered} \tag{5.2}$$

where $\bar{E}, \bar{v}$ and $\bar{G}$ are the effective Young's modulus, Poisson's ratio and shear modulus. In order to investigate the effects of loading directions on the macroscopic responses of the model, the small traction was also applied on the top edge, i.e. $\sigma_{yy} = \sigma_0$. Then the effective elastic constants was calculated similar to Eq. (5.2). For predicting the effective dielectric constants of the composite material, a steady state dielectric analysis was conducted with the following boundary conditions and constraints on the electric potential ϕ ,

$$\phi(0, y) = 0, \phi(L, y) = \phi_{right}, 0 \le \mathrm{y} \le L \tag{5.3}$$

The right edge of the 2D micromechanics model were enforced to have constant electric potentials. A small surface charge was applied on the right edge, i.e. $q_x = q_0$. Then

$$\bar{E}_x = \frac{\phi_{right}}{L}, \bar{\varepsilon}_x = \frac{q_x}{\bar{E}_x} \tag{5.4}$$

where $\bar{E}_x$ is the effective electric field in the x-direction; $\bar{\varepsilon}_x$ is the effective dielectric constants in the x-direction. To investigate the effects of loading directions on the macroscopic dielectric response of the composite effective dielectric constants in the y-direction can be obtained by similar boundary conditions and surface charge loadings as in Eqs. (5.3) - (5.4). The boundary conditions and loadings for 3D micromechanics models can be applied similarly to those of 2D models.

In addition to the mixed boundary conditions (BC) stated above for 2D models other types of BCs, such as constant displacement gradient, uniform traction and periodic BCs for mechanical analysis and constant electric potential gradient, uniform electrical flux, and periodic BCs for dielectric analysis, were also implemented to study their influences on the predicted effective properties. With respect to periodic boundary condition, since not only the meshes but also the microstructures are not periodic, polynomial functions were used to approximate the field fluctuations on the boundaries [173]. In ABAQUS, polynomial functions and reference points are used as constraints to the boundaries. For example, the following equations were used to define the 2nd order polynomial approximation for dielectric analysis,

$$\begin{aligned} &\phi(0,y)=\phi_{x0}+\phi_{x1}\left(\frac{y}{L}\right)+\phi_{x2}\left(\frac{y}{L}\right)^2, \quad \phi(L,y)=\phi(0,y)+\langle\vec{g}\rangle\cdot\vec{p}_x; \\ &\phi(x,0)=\phi_{y0}+\phi_{y1}\left(\frac{x}{L}\right)+\phi_{y2}\left(\frac{x}{L}\right)^2, \quad \phi(x,L)=\phi(x,0)+\langle\vec{g}\rangle\cdot\vec{p}_y \end{aligned} \tag{5.5}$$

where $\phi_{x0},\cdots,\phi_{y2}$ are the electric potentials at reference points; $\vec{p}_x=(L,0)^T$ and $\vec{p}_y=(0,L)^T$; and $\langle\vec{g}\rangle$ the applied macroscopic electric potential gradient. Similar approximations apply to static mechanical analysis for elastic constants predictions. The effective properties predicted by periodic BC are bounded by those obtained by constant gradient and uniform traction (or flux) BCs, where constant gradient BC results in an upper bound and uniform traction (or flux) BC leads to a lower bound. In addition, for the dielectric analysis if the dielectric constant of the particulate reinforcement is larger than that of the matrix, which is the case in this study, then the convergence rate of uniform flux BC is similar to that of periodic BC and is much faster than that of constant electric potential gradient BC [174]. As shown in the following sections, for the effective dielectric constant the mixed BC gives a close prediction to the lower bound (uniform flux BC) and for the effective elastic constants the influence of different BCs is negligible. As a result, in the following simulations the mixed BC is employed, except a comparison of various BCs, because of its computational efficiency.

5.4.1 Effective elastic constants

Figure 5.6 shows the effective elastic constants of Ag/BaTiO$_3$ composite by using a polynomial function approximation up to 5th order. Note that the linear polynomial approximation (1st order) is equivalent to the constant displacement gradient BC. It is clear that the influence of different BCs is negligible. As a result, mixed BC will be used in the following analysis for its computational efficiency. The effects of microstructure and loading directions on the predictions of the effective elastic constants is shown in Figure 5.7 for 10 vol% Ag/BaTiO$_3$ composite. For each composition four 2D models were generated to reduce the influences of microstructure dispersions which is shown in Figures 5.7 (a) and (c) for the effective Young's modulus and shear modulus, respectively. The actual silver volume fraction for each FE model is the same as that for effective thermal conductivity analysis reported in [182], since the samples for dielectric constant and thermal conductivity tests were all from the same batch fabricated using the same procedure. The largest differences between the predictions of these four models are 1.51

GPa and 0.62 GPa for effective Young's modulus and shear modulus, which are 1.34% and 1.45% of their average, respectively. On the other hand, the largest differences between loading directions are 1.16 GPa and 0.49 GPa for effective Young's modulus and shear modulus, which are 1.03% and 1.16% of their average, respectively. Consequently, though microstructure introduced anisotropy exists, its magnitude is very small. The predictions averaged from four finite element analyses were plotted in Figure 5.7 (b) and (d) for different silver contents. It is clear that after averaging the predictions from x-direction loading and y-direction loading almost lie on top of each other, which means the microstructure introduced anisotropy was significantly reduced.

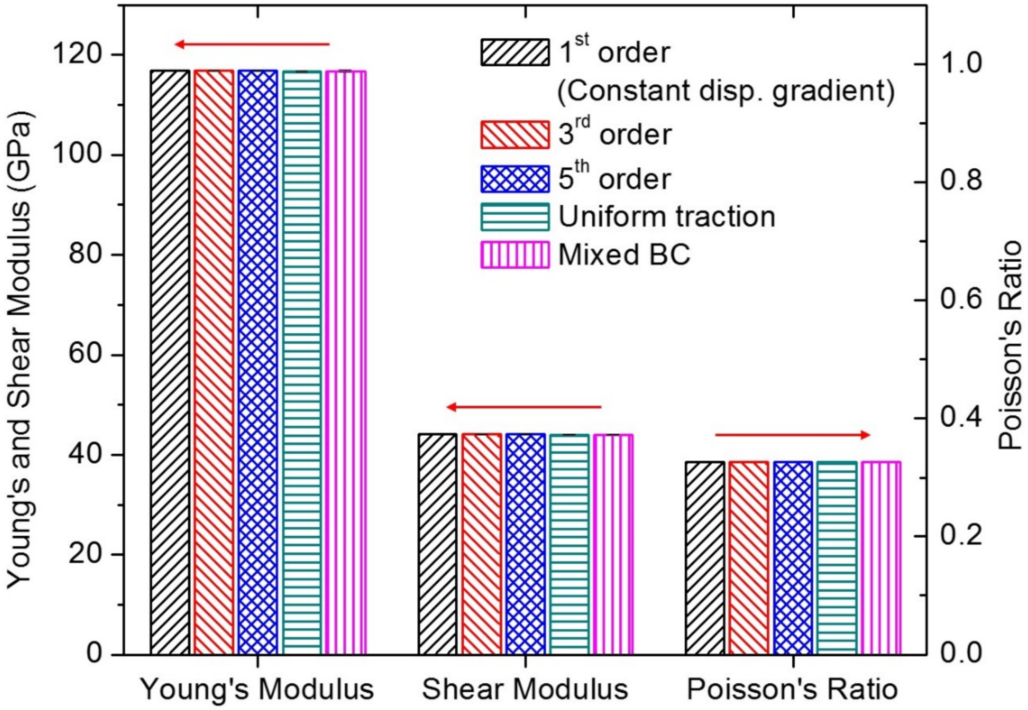

Figure 5.6 Effective elastic constants predicted by various boundary conditions for 2D micromechanics models for 5 vol% composite.

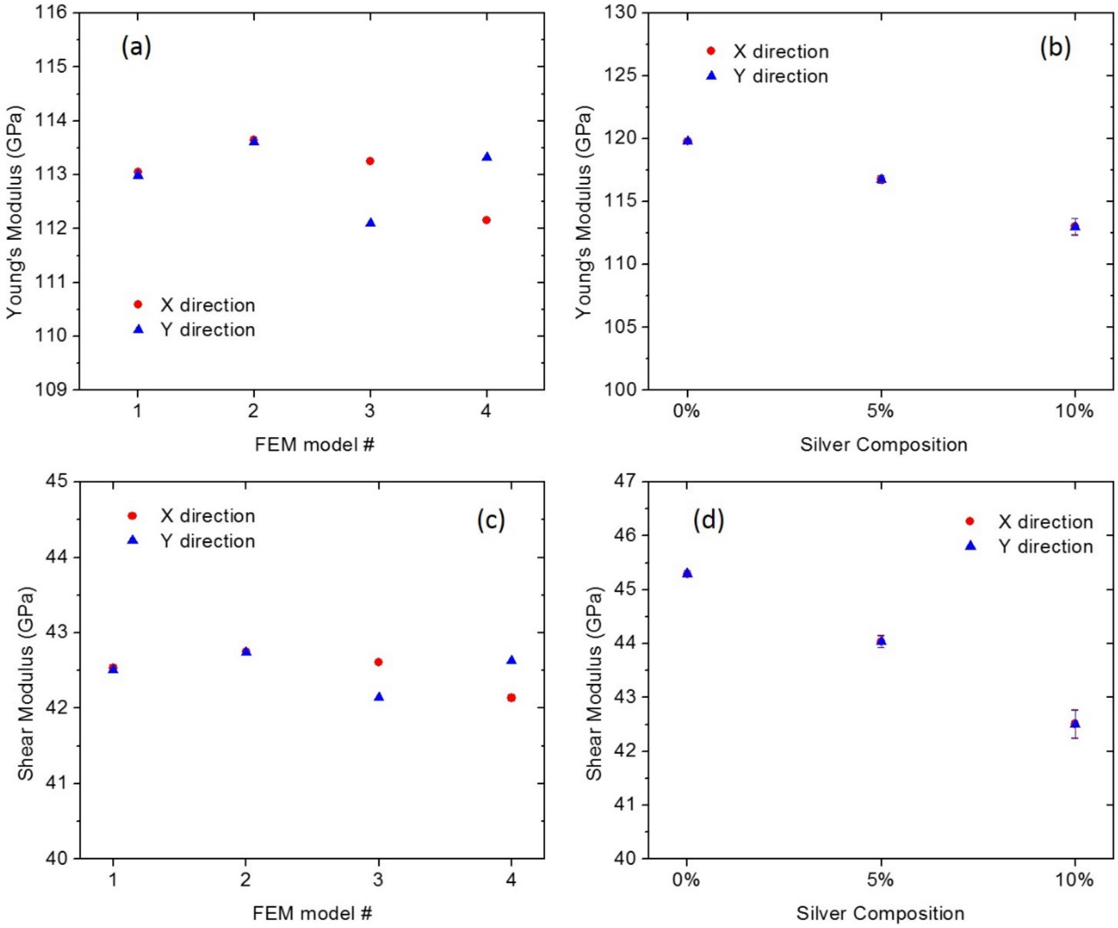

Figure 5.7 Effects of microstructure and loading directions on effective Young's modulus and shear modulus for 10 vol% Ag/BaTiO$_3$ composite.

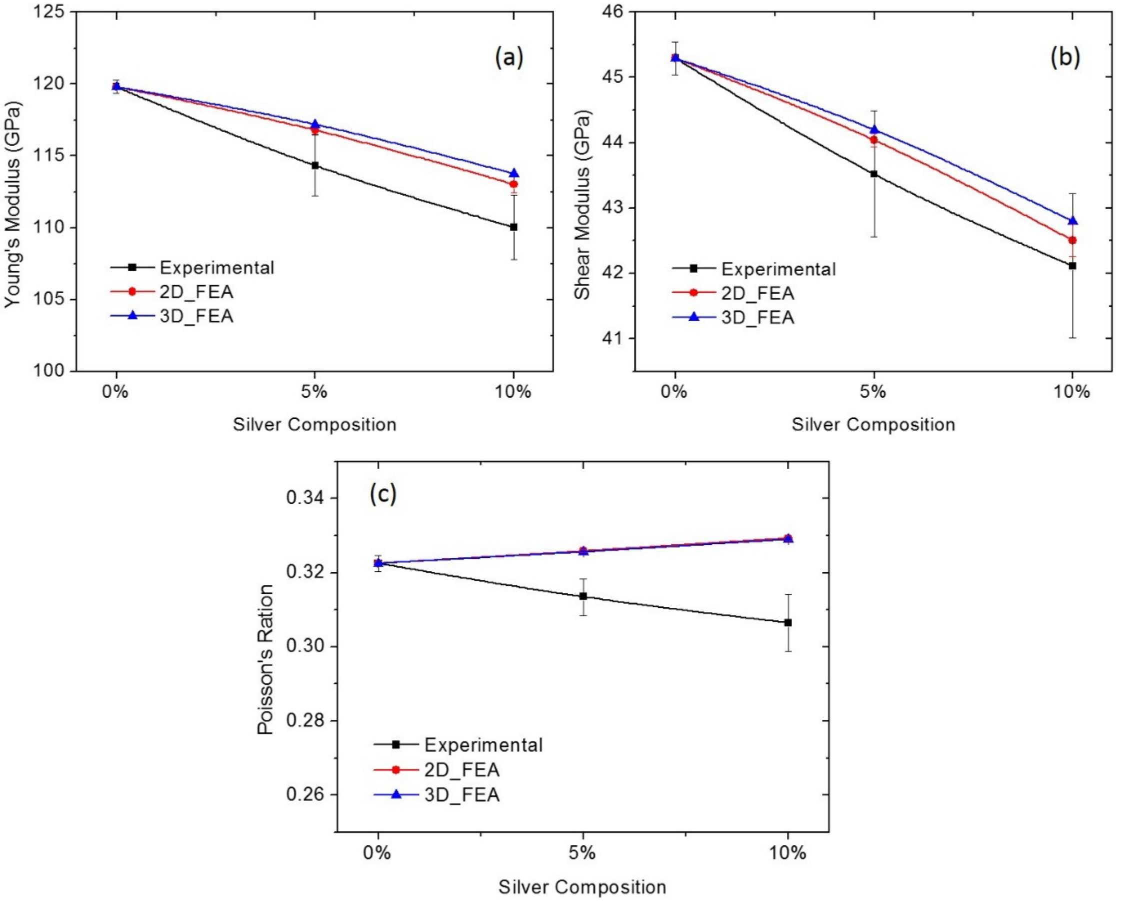

Figure 5.8 Comparison of predicted effective elastic constants to the experimental results for Ag/BaTiO$_3$ composites.

The comparison of predicted effective elastic constants to the experimental results for Ag/BaTiO$_3$ composite was shown in Figure 5.8 for different silver compositions. The prediction results from the micromechanics models based on 2D realistic microstructures and 3D randomly generated microstructures are very close to each other. The largest relative differences are 0.66%, 0.68% and 0.11% for the effective Young's modulus, shear modulus and Poisson's ratio, which might be due to the difference in shape and dispersion of the silver particles. The predictions slightly overestimate the experimental results. For 2D micromechanics models the largest overestimations are 2.7%, 1.2% and 7.46% for the effective Young's modulus, shear modulus and Poisson's ratio. Note that this difference is still within the standard deviation of experimental data. However, the possible reason for such overestimation might also be result from micromechanics model built in this work in which the interfaces were assumed to be perfect and no defects were taken into consideration. However, it is inevitable to introduce defects both within each phase and on the phase interfaces during the process of sample fabrication. Consequently, the micromechanics predictions slightly overestimate the experiment results.

One advantage of micromechanics models based on detailed microstructures of the composite is that the local field fluctuations can be simulated. The simulated von Mises stress contours are shown in Figure 5.9 for Ag/$BaTiO_3$ composites. The loading is in the x-direction and the nominal stress is 1. It is clear that stress concentration exits around phase interfaces, though the stress in most portion of the computational domain lies between 1.0 and 1.1. The stress concentration for 10 vol% composite is larger than that for 5 vol% composite, because the distance between Ag particles are smaller in 10 vol% composite. Furthermore, the stress concentration in 3D micromechanics models are smaller than that in 2D models, because the particles in 3D models are spherical unlike in 2D models based on real SEM images. It can be concluded that the effect of stress concentration from the microstructural variations on the overall (macroscopic) linear elastic properties is quite negligible.

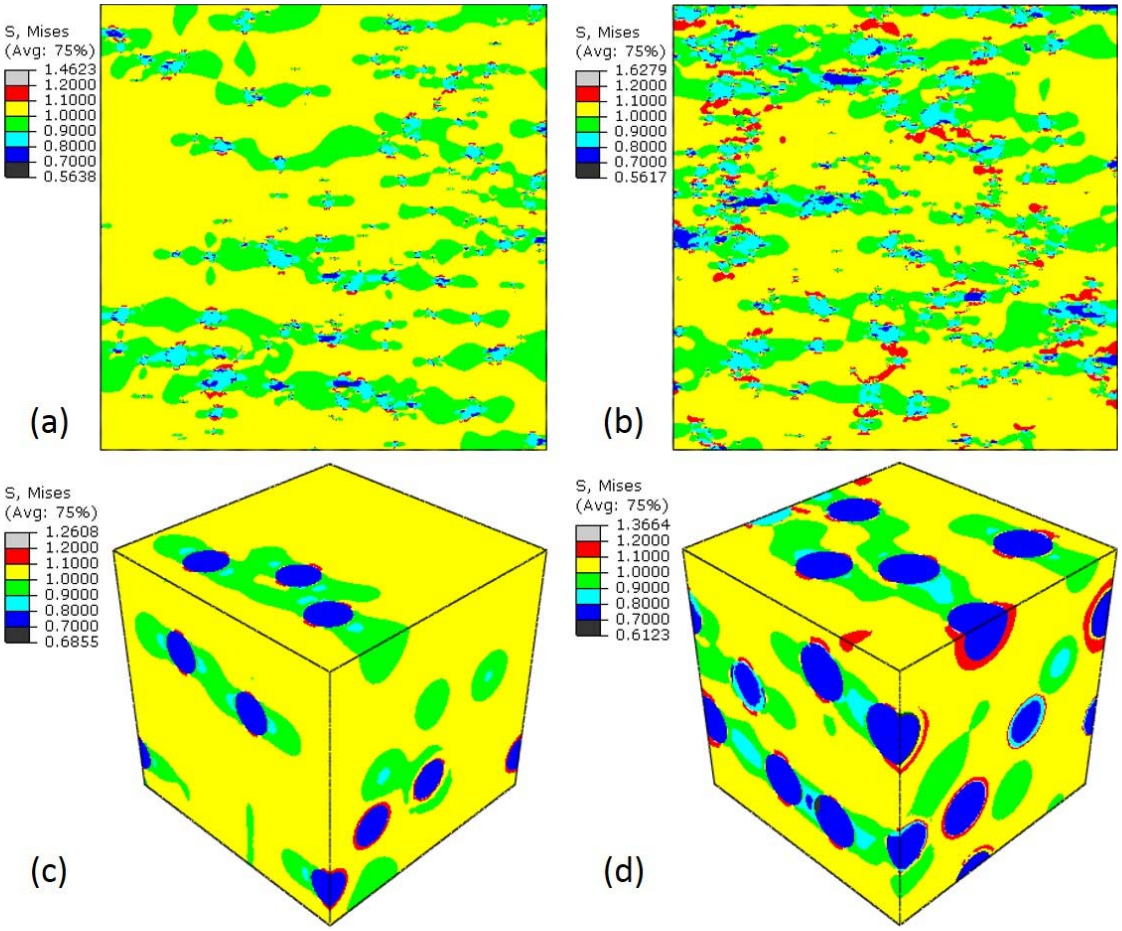

Figure 5.9 Simulated von Mises stress contours for Ag/BaTiO$_3$ composite: (a) 2D model for 5 vol% Ag; (b) 2D model for 10 vol% Ag; (c) 3D model for 5 vol% Ag; (d) 3D model for 10 vol% Ag.

5.4.2 Effective relative permittivity

Similarly, the above micromechanics models are used to study the overall relative permittivity of composites. Figure 5.10 shows the effects of microstructure and electric field direction on the effective relative permittivity, where the effective dielectric constant (ε_{eff}) for 10 vol% Ag/BaTiO$_3$ composite is shown in the Figure 5.10 (a), while the Figure 5.10 (b) is ε_{eff} for varying Ag composition. Both analyses were conducted at room temperature and 1 MHz operating frequency. Again the actual silver volume fraction for each FE model is the same as that for effective thermal conductivity analysis reported in [182]. As shown in Figure 5.10 (a), among all FE models the largest difference of the effective dielectric constants for each loading direction is 91.9 at FE model 1. This difference is relatively small compared to the magnitude of the dielectric constant itself (only 3.91%). Furthermore, since for each composition four FE models were constructed, the largest relative difference between the averaged values of the four models is even smaller, only 0.76% as shown in Figure 5.10 (b). This means that the 2D realistic microstructure based micromechanical FE models are approximately isotropic and can well represent the macroscopic isotropy of the material. The largest relative difference in the effective dielectric constants averaged from x- and y- direction values among all four FE models is 7.14%, which, though small, still indicates certain degree of dispersion in microstructure among the FE models. Such microstructural variations, together with the fact that averaging four models obviously reduces the largest relative difference between different loading directions (from 3.91% to 0.76%), justifies the necessity of generating four FE models for each composition for effective dielectric analysis.

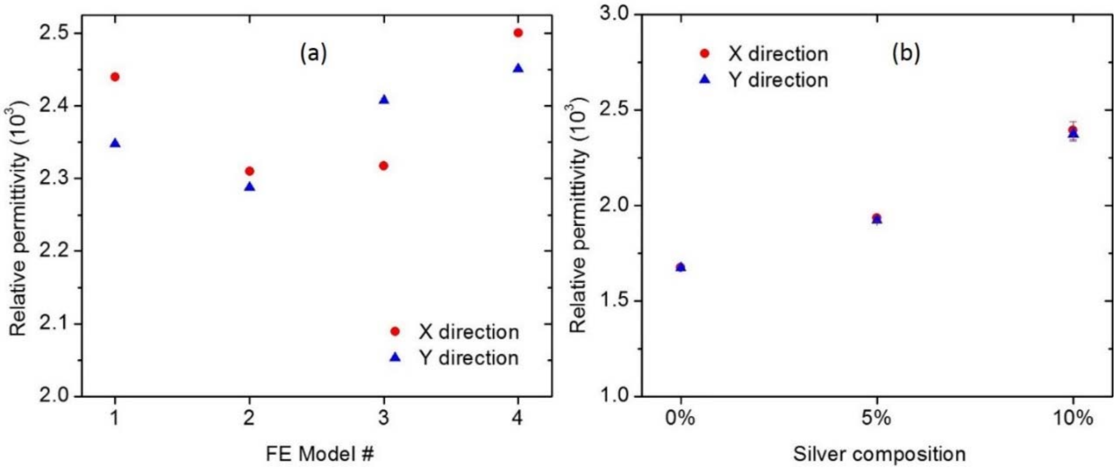

Figure 5.10 Effects of microstructure and loading direction on effective dielectric constants: (a) ε_{eff} for 10 vol% Ag/BaTiO$_3$; (b) ε_{eff} for varying Ag composition. Both at room temperature and 1 MHz frequency.

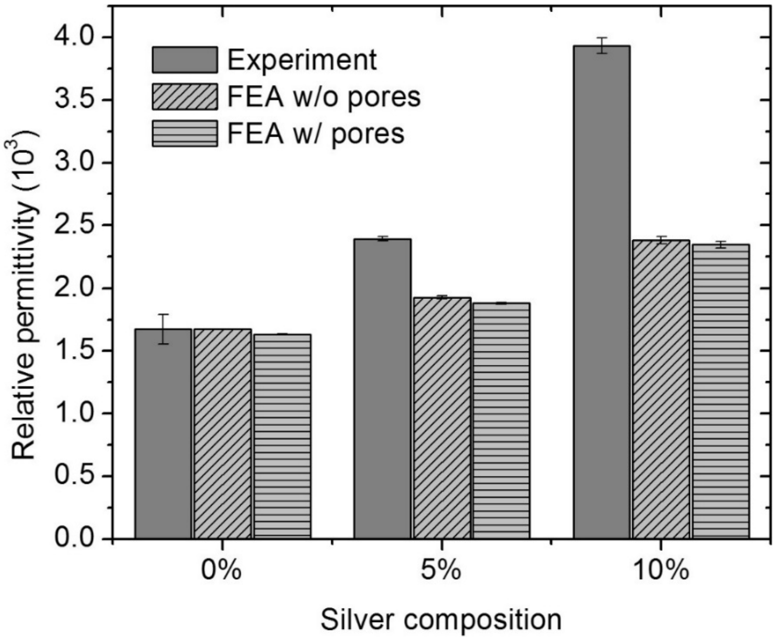

Figure 5.11 Effects of pores on effective dielectric constant ε_{eff}, at room temperature and 1 MHz.

The effects of porosity on effective dielectric constants from FE simulations (without pores and that with pores) are shown in Figure 5.11, where a comparison with experimental results is also provided. The volume fractions of silver and pores are the same as that for effective thermal conductivity analysis in [182] for the reason given previously. It is clearly that pores slightly decreases the effect dielectric constants, which is because the dielectric constant of pore is equal to that of vacuum. The pores in the ceramic serve as electric flux barriers and interrupt its paths. The largest relative difference between simulated results with and without pores is 2.48%, which happens at 5 vol% composite with a porosity of 0.87%. This difference is relatively small and negligible compared to the difference between experimental results and FE simulated values, which is 19.42% for 5 vol% composite.

The effective dielectric constant predicted by various boundary conditions for 2D micromechanics models for 5 vol% composite are shown in Figure 5.12 (a). Note here that the vertical axis is in logarithmic scale. Polynomial function approximation of the periodic BC up to the 5th order was implemented. Note that the linear polynomial approximation (1st order) is equivalent to the constant electric potential gradient BC, which gives an upper bound prediction. As expected, increasing the order of polynomial approximation decreases the predicted value of the effective dielectric constant. Since the ratio of the dielectric constant of silver to that of barium titanate is theoretically infinite, the predicted values for composites at lower polynomial approximation are extremely high. The prediction from Uniform flux BC is the lower bound, which is very close to the mixed BC prediction. In addition, the experimental value lies between the upper and lower bounds. Figure 5.12 (b) shows a comparison of the effective dielectric constants from experimental results, 2D and 3D FE simulated values at room temperature. Mixed BC is used for its computational efficiency. The simulated results, both for 2D and 3D FE models, underestimate the experimental measured values. It is clearly shown in Figure 5.12 (b) that the experimentally measured values as a function of silver content increase much more rapidly than those from FE simulations. The increase of dielectric constants as a function of silver is approximately a linear function of the silver content in FE predictions, while can be described more suitably by a power law equation for experiment results [72]. As a result, the discrepancy between measured and simulated values rapidly increases as the increase of silver content. For 2D FE models at 1 MHz operating frequency the underestimation is 19.42% for 5 vol% composite while it reaches 39.39% in 10 vol% composite. There are several possible reasons for such underestimation. First, conductive silver particles within the matrix serve as internal electrodes. Similar to the formation of thermal conductive chains in thermal conductivity test, they are inclined to form electrical conductive chains in dielectric measurements, which can provide a relative much easier "conductive bridge" for the electric flux to pass through. Increasing silver content assists the formation of conductive chains [72]. However, such effects of electrical conductive chains are not well considered in the FE based micromechanical models. Second, silver particles are conductive and, theoretically, its dielectric constants are infinite, which means the contrast (ratio of dielectric constant of silver to that of barium titanate) is theoretically infinite. In the numerical simulation a very large dielectric constant (10^8 times the value for $BaTiO_3$) was inputted for silver to approximate its theoretical value. It is well known that in the calculation of effective properties by micromechanical models the error becomes increasingly significant with the contrast of material properties increases. As a result, noticing such a huge contrast in dielectric properties between silver and barium titanate it is not very surprising that the prediction error is large. Compared to the underestimation for effective thermal conductivity in [182], the underestimation for effective dielectric constant is much larger (39.39% versus 18.71% for 10 vol% composite). This might be due the much larger differences in dielectric constant between two constituents, than that of thermal conductivity (infinity versus approximate 114). Finally, in the simulation we assumed a linear constitutive relation between electric field and electric displacement, i.e. $\vec{D} = \varepsilon_{eff} \vec{E}$. However, there might be other mechanisms to relate them, especially when the silver composition is large, which was not taken into consideration during the numerical simulation.

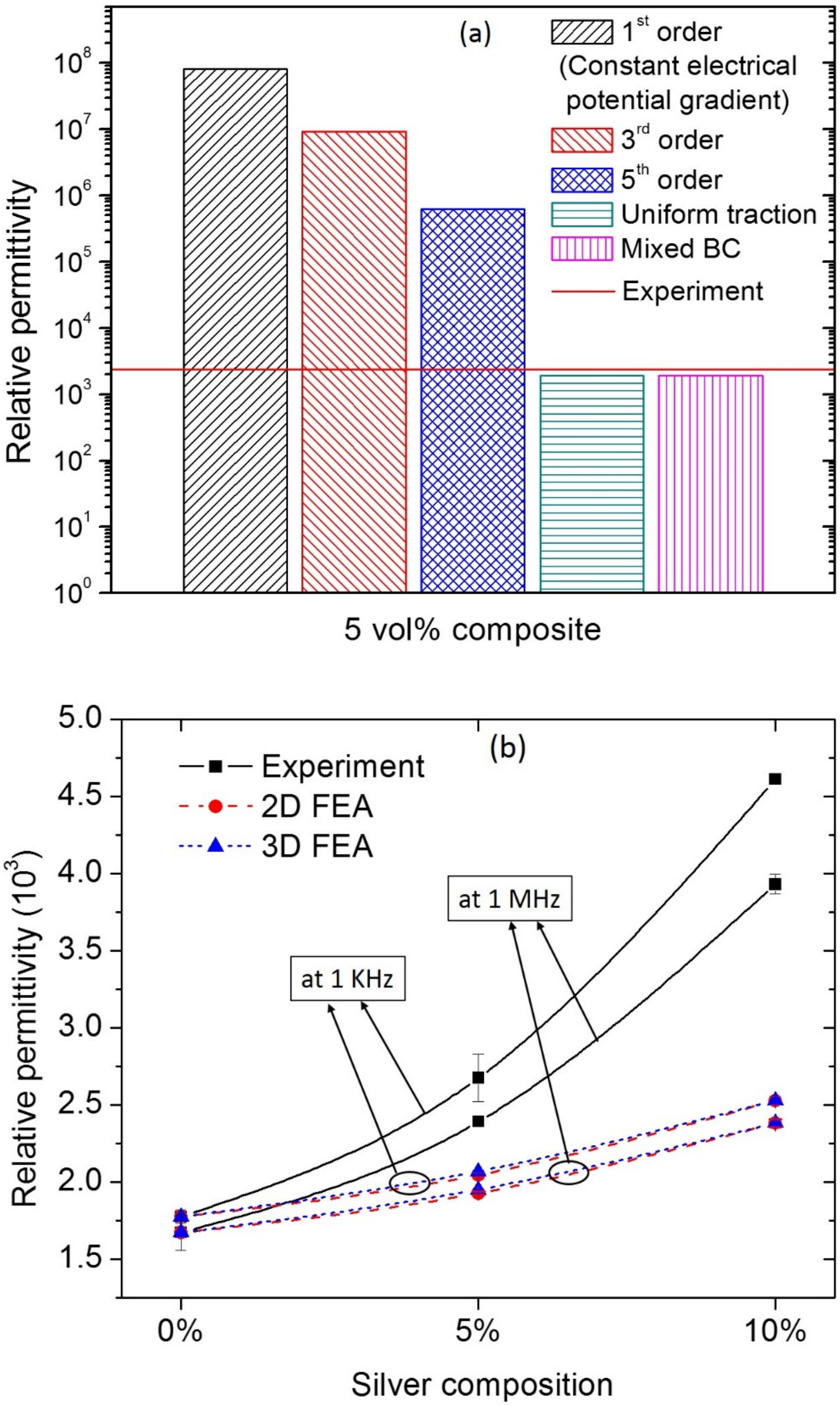

Figure 5.12 Micromechanics model predictions: (a) effects of different BCs (logarithmic scale in vertical axis); (b) comparison between experiments and predictions from mixed BC.

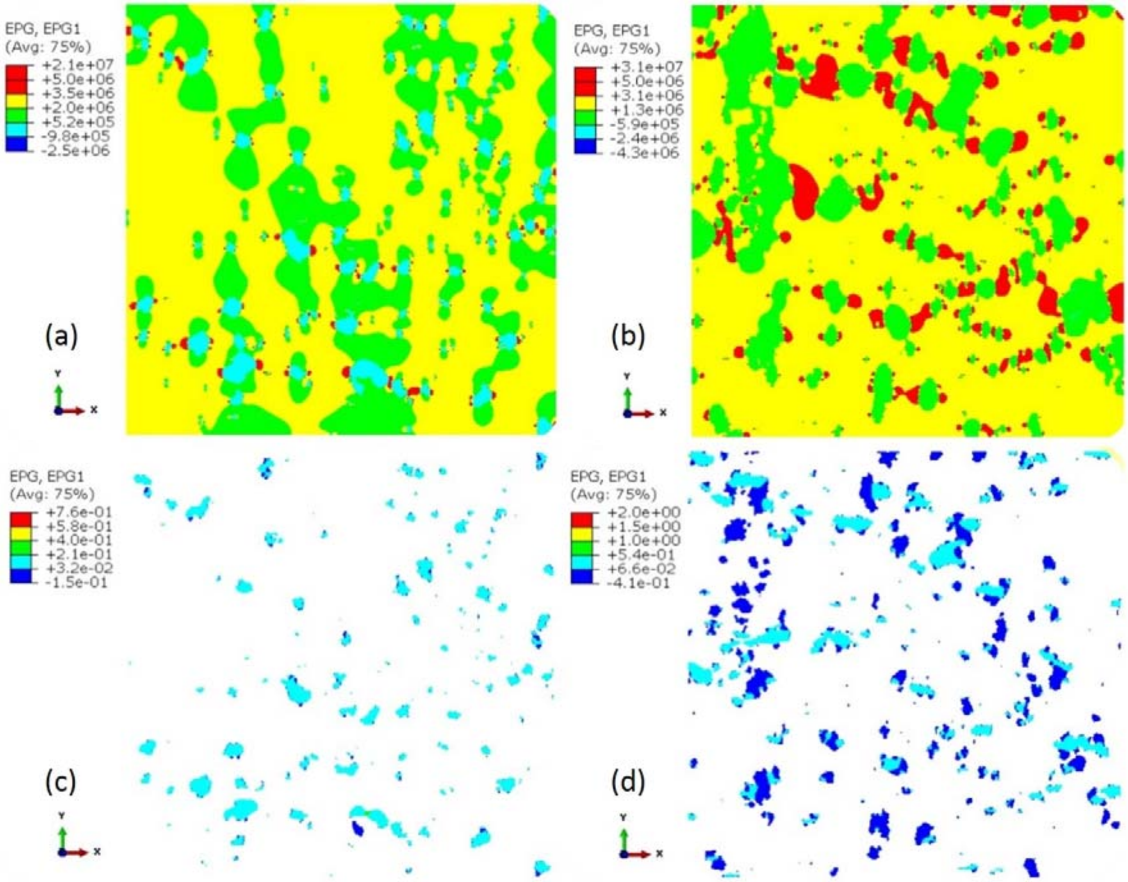

Figure 5.13 Simulated electric potential gradient in x direction for 2D models: (a) 5 vol% Ag/BaTiO$_3$; (b) 10 vol% Ag/BaTiO$_3$; (c) Ag particles for 5 vol% composite; (d) Ag particles for 10 vol% composite.

Figures 5.13 and 5.14 show the detailed local electric fields in *x*-direction for 5 vol% and 10 vol% Ag/BaTiO$_3$ composites for 2D and 3D micromechanics models, respectively. In the simulations, the left edge (*x=0*) was prescribed with zero electric potential, while the right edge (*x=L*) of the model was prescribed with an electric potential with a magnitude that leads to an effective electric field of 1 MV/m in the composite. The reason for this is that the poling of BaTiO$_3$ samples usually needs an electric field of this magnitude. The simulations were done at room temperature and with an operating frequency of 1 MHz. The theoretically infinite dielectric constant of silver was approximated with a vale that are 10^8 times of the dielectric constant of $BaTiO_3$. This value was selected because firstly it is big enough, and secondly it will not incur numerical difficulty by extremely deteriorating the condition number for the system matrix. For 2D models, as shown Figure 5.13 (a) and (b), the magnitude of electric field in x-direction is in the range from 2.0 to 3.5 MV/m for 5 vol% composite, while in the range from 1.3 to 3.1 MV/m for 10 vol% composite. It is clearly shown that adding silver particles in the composite greatly increases the area with larger magnitude of electric field. Since the nominal electric field is 1 MV/m, the concentration factor for 5 vol% composite is 21, while it reaches values of 31 for 10 vol% composite. Electric field concentration usually happens along the interfaces at barium titanate side, especially in areas between two nearby silver particles. Since silver particles are conductive, as expected the electric field within silver is approximately zero compared to that within barium titanate. The electric field distribution patterns for the 3D models are similar to that in 2D models, as shown in Figure 5.14, except its concentration is lower due to the smooth surfaces of the spherical silver particles. To clearly show the direction of simulated electric fields their resultants were plotted as vector symbols in Figure 5.15. Since silver particles serve as internal electrodes, electric fields flows along those conductive particles. The electric fields emanate from silver particles to nearby silver particles. Electric fields that flow along the shortest path between adjacent silver particles have larger magnitudes. Through the above detailed local field analysis, it is clear that more attention must be paid when trying to pole $BaTiO_3$ ceramic with metal particles reinforcements. When poling metal/$BaTiO_3$

composite, application of external nominal field of 1 MV/m will result in the actual fields in some parts of the sample well above 1 MV/m with the field concentration effect which would increase locally its magnitude to 20, even 30 times of the nominal one. Consequently, if not well designed it would be in a great risk to destroy the samples and damage the equipment.

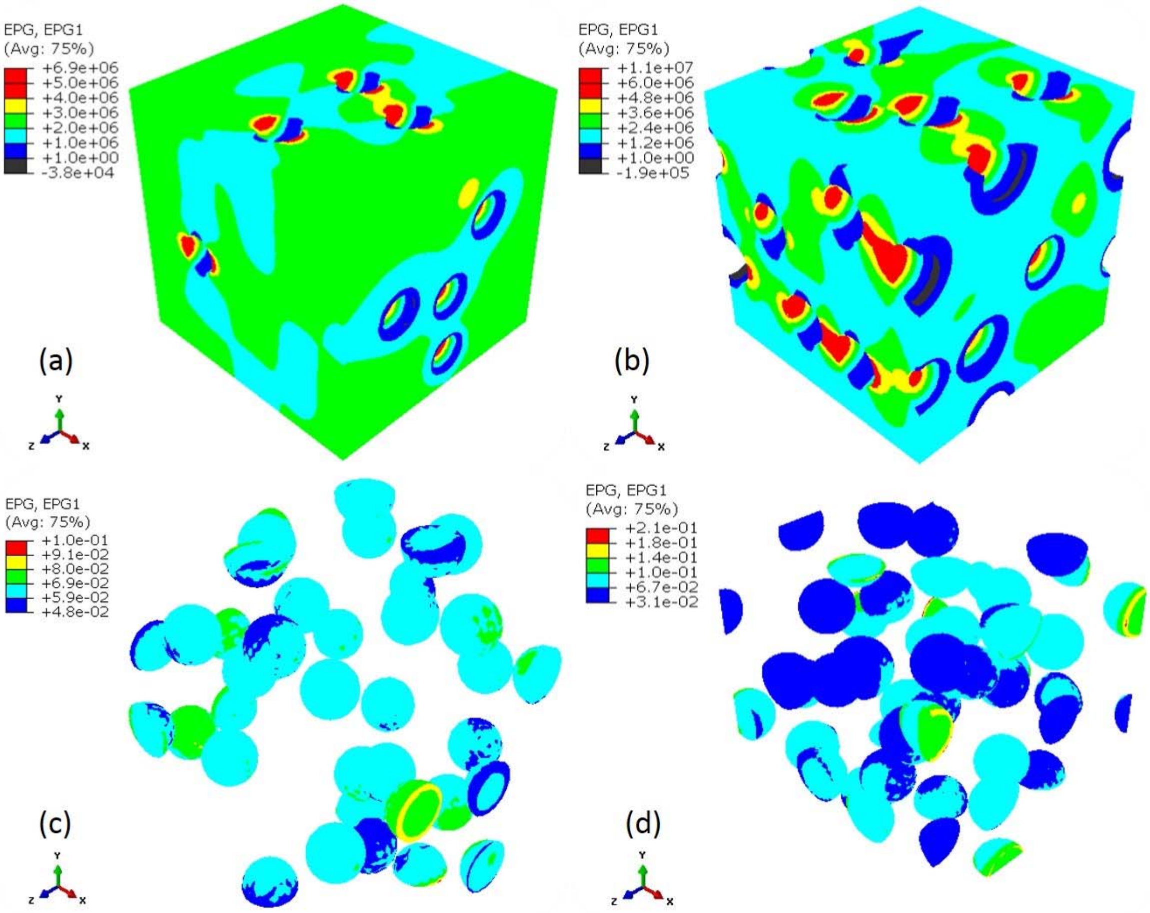

Figure 5.14 Simulated electric potential gradient in x direction, 3D model: (a), (c) $BaTiO_3$ and Ag for 5 vol% composite, respectively; (b), (d) $BaTiO_3$ and Ag for 10 vol% composite, respectively.

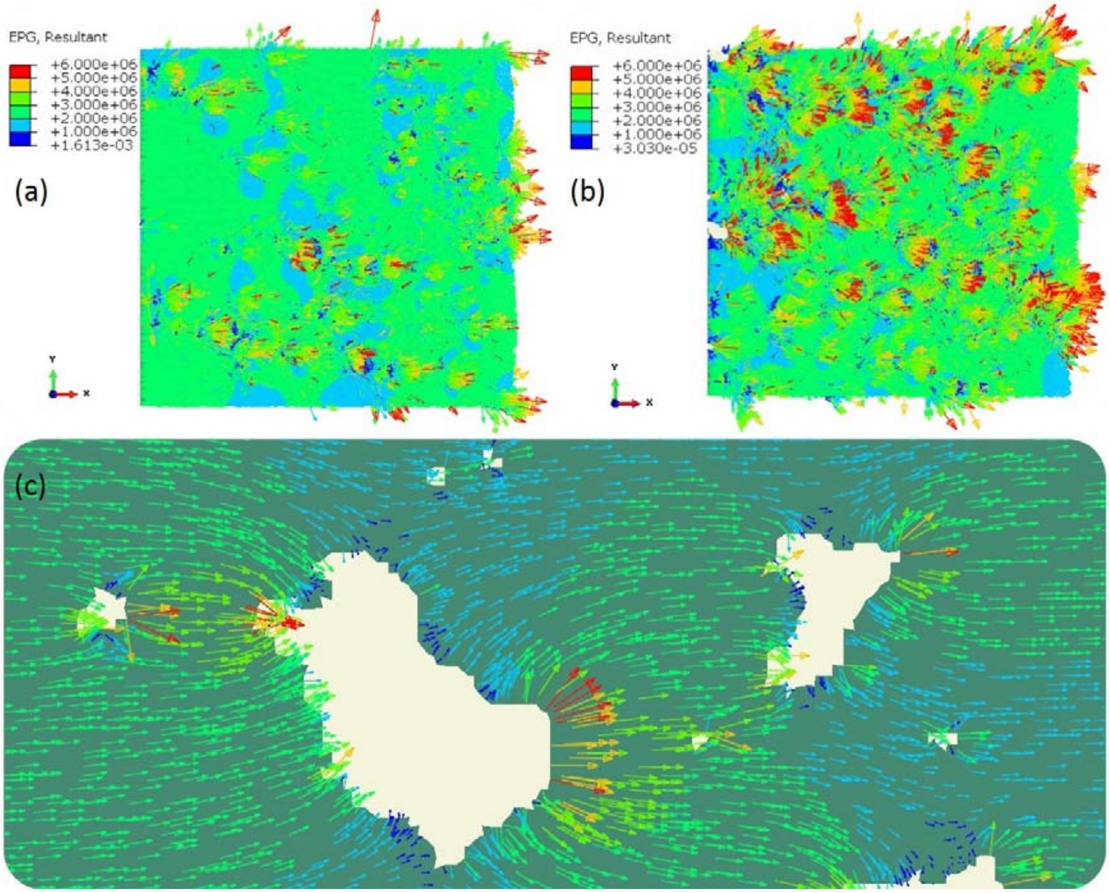

Figure 5.15 Symbolized simulated electric fields resultant direction for 2D models: (a) 5 vol% Ag/BaTiO$_3$; (b) 10 vol% Ag/BaTiO$_3$; (c) enlarged plot for 5 vol% Ag/BaTiO$_3$.

CHAPTER VI

A NONLINEAR CONSTITUTIVE MODEL FOR DESCRIBING CYCLIC MECHANICAL RESPONSES OF AG/BATIO$_3$ COMPOSITES

6.1 Introduction

At low stress level, the response of BaTiO$_3$ ceramic is linear elastic and no permanent deformation is observed upon unloading. This indicates that under such low stresses, microstructural changes, such as dipole moment reorientations, cracking, etc., do not occur in that the domain structures remain the same. When the applied stress is increased, a nonlinear stress-strain behavior is observed, even when the magnitude of strains is relatively small. Upon unloading, permanent strain is observed which is more pronounced when the specimens were subjected to high stresses. This nonlinear inelastic behavior is attributed to microstructural changes, such as 90° domain wall movements [142]. Externally prescribing a compressive stress, with magnitude higher than the coercive stress limit, will cause the polar axis to rotate to the plane perpendicular to the loading direction, which results in 90° domain wall movement and leads to formation of permanent strain. In addition to reorientation of dipole moments at high stresses, permanent strain can also occur due to microstructural changes such as micro-cracking, grain boundary slipping, etc.

Due to the absence of lead, compared with some other piezoelectric ceramics, BaTiO$_3$ based ceramics are preferred for actuator and sensor applications [4]. In such applications, the material usually undergoes cyclic loads resulting nonlinear hysteretic response and energy dissipation. Consequently, characterization and modeling of the hysteretic response is crucial in those applications. This chapter focuses on the experimental investigation of the hysteretic behavior of pure $BaTiO_3$ and $Ag/BaTiO_3$ composite under cyclic compressive loading and development of a constitutive model that take into account microstructural changes.

6.2 Experimental procedure and results

$Ag/BaTiO_3$ composite samples were fabricated by powder metallurgy method. The volume fractions of Ag powder used to prepare samples for this study were chosen to reach 0 vol%, 5 vol%, 10 vol% and 13 vol% of Ag in the final samples. The maximum silver volume fraction in the specimen is 13 vol% because the melting point of silver, which is 961.8 ^{o}C, is much lower than the sintering temperature (1250 ^{o}C). As a result, adding more silver content would result in the silver being squeezed out of the composite during the sintering process, which leads to large amount of porosity and also undetermined silver volume fraction in the final product after sintering. The density of the sintered samples was measured by Archimedes' principle and listed in Table 6.1 for completion. Detailed description of processing method, porosity and constituent compositions, and microstructural morphologies of the samples can be found in Xing et al. [182].

Table 6.1 Relative density and porosity of Ag/$BaTiO_3$ composite with varying silver composition.

Volume Fraction	0 vol%	5 vol%	10 vol%	13 vol%
Relative density (%)	96.98±0.15	96.60±0.26	97.39±0.06	96.46±0.13
Open porosity (%)	0.02±0.01	0.02±0.01	0.08±0.02	0.19±0.06
Closed porosity (%)	3.00±0.16	3.38±0.27	2.53±0.07	3.35±0.11

The stress-strain curves for pure $BaTiO_3$ and different Ag/$BaTiO_3$ composite were obtained under cyclic uniaxial compressive loading using material test system (MTS, MTS Systems Corp., MN). To reduce the chance of stress concentration due to the possible imperfect contact between sample surfaces and the spacers of the MTS machine, the sintered samples were cut to ensure the flatness and parallelism of their top and bottom surfaces. The carefully machined composite specimens have a cylindrical shape with dimensions of approximately 17.5 mm in height and 8.75 mm in diameter. Due to its extreme brittleness, pure $BaTiO_3$ specimens have been machined to smaller dimensions of approximately 12.6 mm in height and 6.31 mm in diameter. The length to diameter ratio for all specimens is approximately 2:1 to reduce the chance of buckling. For composite specimens an axial extensometer (MTS Systems Corp., MN) was attached directly on the sample to measure the deformation, from which the strain can be calculated. For pure $BaTiO_3$ ceramic specimens, however, due to its smaller height relative to the gauge length of the axial extensometer the extensometer was attached to spacers inserted between samples and pushrods. As a result, the measured deformation is the summation of the deformation of the ceramic sample and the spacers. However, the spacers' contribution to the total deformation can be neglected because of its much larger elastic modulus (i.e. elastic modulus of the spacer's material, i.e., tungsten carbide, is ~650 GPa [191]) compared with the ceramic samples. A displacement-controlled testing mode with a crosshead speed of 0.001 mm/s was adopted to control both the loading and unloading process. To ensure a perfect contact between the tips of the extensometer and the lateral surface of the cylindrical specimens a preload with a magnitude of approximately 3 MPa was applied on the samples. During testing the specimen was first loaded to a maximum stress level and then was unloaded to the preload at the same speed. In a subsequent testing step, the magnitude of the maximum stress was augmented by a certain value, usually around 25 or 50 MPa. The specimen was reloaded to this maximum stress level and then unloaded again to the preload. These steps were repeated until either the maximum stress of 200 MPa was reached or the sample failed.

Selected but typical stress-strain hysteretic responses for Ag/$BaTiO_3$ composites with varying silver composition are plotted in Figure 6.1. Note that 3-4 tests were conducted for each composition to ensure the repeatability of the testing. Scanning Electron Microscopy (SEM) images for different silver composition are also included as inserts in Figure 6.1. Figure 6.1 (a) shows the hysteretic response of monolithic $BaTiO_3$. During the loading of pure $BaTiO_3$ in the first loading-unloading cycle, obvious "toe region" can be observed at the beginning of the stress-strain curves. Furthermore, much smaller "toe region" can be still observed at the preloading stress level. Since the height of the monolithic $BaTiO_3$ ceramic specimens was slightly smaller than the extensometer gauge length, the extensometer was attached to the spacers. Therefore, compression and slip of the spacer-specimen interface is the most likely reason for the observed "toe region" at the beginning of stress-strain curves in Figure 6.1 (a). Consequently, after the loading cycle at larger stresses, the contact between the sample surface and the spacer became much tighter and the influence of toe was significantly mitigated. To remove the influence of toe region observed, the stress-strain curves were shifted to zero strain at the beginning of the second loading cycle, which allowed the comparison of stress-strain curves obtained for pure $BaTiO_3$ with those obtained for $Ag/BaTiO_3$ composites.

The polycrystalline specimens were tested in as-processed state and therefore it is reasonable to assume that all dipole moments in the $BaTiO_3$ were randomly distributed. When a compressive force is applied the dipoles tend to rotate to the plane perpendicular to this force, which results in a domain wall movement. Since an energy barrier needs to be overcome to initiate the rotation of dipoles, there is a stress threshold, only above which the domain wall can move under the mechanical loading. Such stress threshold is the coercive stress. On the other hand, domain wall cannot further evolve when all rotatable dipoles have been reoriented. The coercive stress cannot be exactly identified in Figure 6.1 (a), but it is located between 25 MPa and 50 MPa because an inflection point happens within this range in the loading curves. The area enclosed by the loading and unloading curves of each cycle is the energy dissipated due to domain wall movement and other microstructural changes. The unloading curve at each cycle is convex with decreasing strain rather than a straight line with a constant strain, indicating part of the rotated dipoles was recovered when the compressive load was removed.

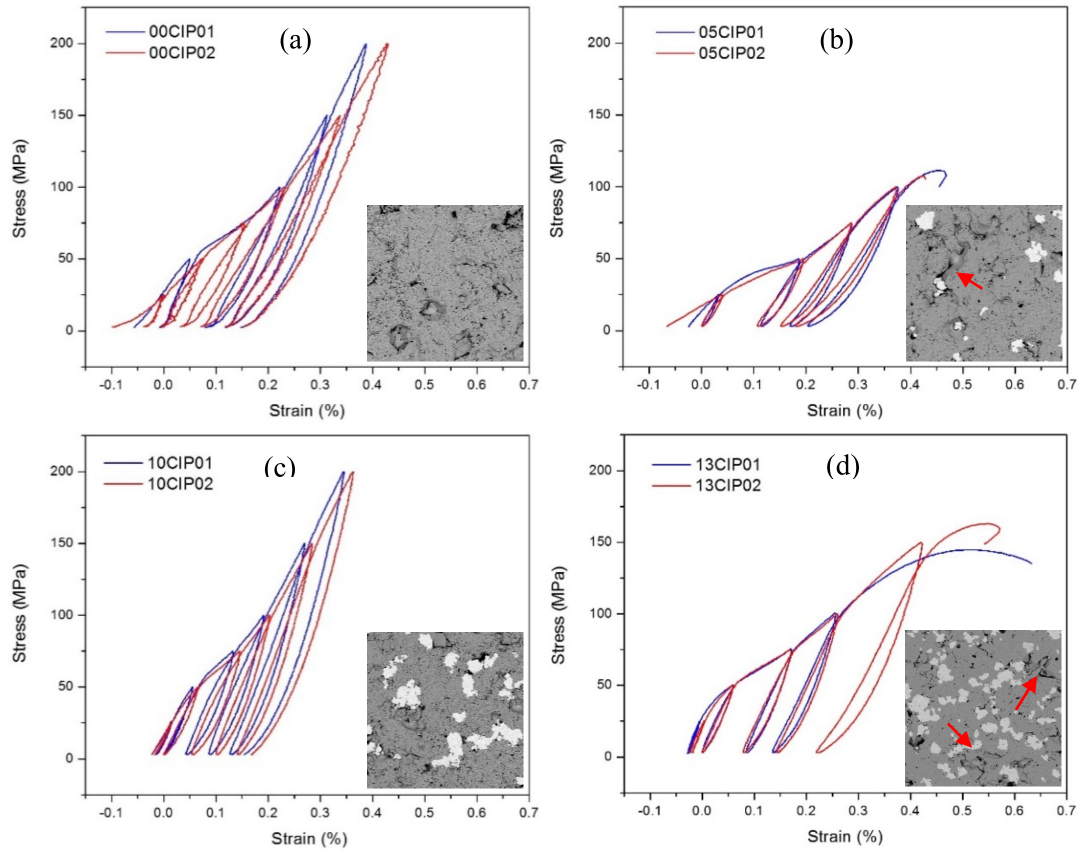

Figure 6.1 Ferroelastic stress-strain hysteresis for Ag/BaTiO$_3$ composite with varying silver composition: (a) pure BaTiO$_3$ ceramic; (b) 5 vol% silver; (c) 10 vol% silver; (d) 13 vol% silver. In the legend the label "05CIP02", for example, means the second specimen of the 5 vol% composite material. SEM images for different silver composition are also included. The size the SEM images is ~211 µm.

The hysteretic curves for 5 vol% silver composite is plotted in Figure 6.1 (b). A large toe region is observed again for the first loading cycle due to the possible unparalleled surface and effect of surface asperities on specimen surface and spacers under a small load. However, unlike the monolithic ceramic tests where the extensometer was attached to the spacers no toe region was further observed in subsequent cycles when unloaded to the preload stress level. For 5 vol% silver composite the largest portion of dipole rotation happens in the 25 MPa to 50 MPa cycle. The specimens broke at a loading level around 115 MPa, which is smaller than that for the monolithic $BaTiO_3$ ceramic. The hysteretic curves for 10 vol% silver composite have similar trend as that for pure $BaTiO_3$ ceramic as depicted in Figure 6.1 (c). Large portion of inelastic strain was developed in the 50 MPa to 100 MPa loading cycle where the dipoles can be easily reoriented to the plane perpendicular to the applied force. The 13 vol% silver composite specimens broke at a stress level around 150 MPa as shown in Figure 6.1 (d). The failure is ductile facture because a large amount of inelastic deformation was developed before the final cleavage of the samples. The fractured composite samples with 5 vol% and 13 vol% showed a fracture angle of approximate 45 ºC which is a characteristic of ductile fracture. The relative large silver content in 13 vol% silver composite significantly enhanced the specimens' ability to deform like a ductile material. However, it also introduced more defects in the composite and led to lower failure strength.

It is worth noting here that both 5 vol% and 13 vol% composites failed at relatively lower stresses (115 and 150 MPa, respectively) when compared to the pure $BaTiO_3$ and 10 vol% composite. The later, can be attributed to the micro-cracks and pores that were introduced during sintering of those samples. SEM images in Figure 6.1 illustrate that 5 vol% and 13 vol% composites contain more sharp micro-cracks between $BaTiO_3$ grains and pores and between $BaTiO_3$ and silver (denoted by arrows in Figure 6.1) when compared to pure $BaTiO_3$ sample and 10 vol% composite. Figure 6.1 shows that at 100 MPa the strain of 5 vol% and 13 vol% composite specimens is larger than the strain of other composite specimens. This is because the permanent strain developed in those composites is due to the combination of dipole reorientation and micro-crack evolution.

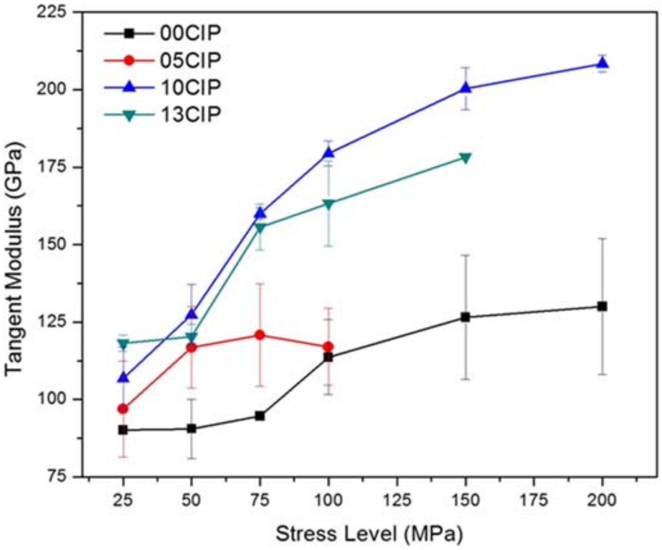

Figure 6.2 Tangent modulus as a function of loading stress level for Ag/BaTiO$_3$ composites.

Table 6.2 Tangent modulus at different loading stress level for Ag/BaTiO$_3$ composite with varying silver composition.

		Stress Level					
		at 25 MPa	at 50 MPa	at 75 MPa	at 100 MPa	at 150 MPa	at 200 MPa
Tangent Modulus (GPa)	0 vol%	90.1	90.5	94.7	113.7	126.5	130.0
	5 vol%	96.9	116.8	120.8	117.0	-	-
	10 vol%	106.9	127.3	160.0	179.4	200.4	208.4
	13 vol%	118.2	120.3	155.7	163.3	178.3	-

Tangent modulus calculated at the initiation of the unloading stage is plotted in Figure 6.2 as a function of loading stress level. Figure 6.2 shows that the tangent modulus increases with increasing stress level. At higher stress level more dioples had already been reoriented to the plane perpendicular to the applied force and hence, the response becomes stiffer. The largest increase of tangent modulus happens between the stress levels of 50 MPa and 100 MPa which corresponds to the region where dipoles can be easily reoriented as indicated by the largest amount of energy dissipation shown in Figure 6.1. At higher stress levels the tangent modulus was only slightly increased due to the nearly saturation of dipole reorientation. The slower increase and even decrease in elastic modulus of 5 vol% and 13 vol% composites above stresses of approxiamtely 75 MPa when compared to pure $BaTiO_3$ and 10 vol% composite (refer to Figure 6.2) can be also attributed to the microcrack propagation in those samples.

Table 6.2 lists the average tangent modulus at different loading level for $Ag/BaTiO_3$ composite with varying silver composition. The increase of silver composition increases the tangent modulus up to the 10 vol% compoiste, which results from stress concentration effect. Due to the blending of silver phase to the $BaTiO_3$ matrix, stress concentration was introduced around the interfaces between silver particles and the surounding matrix phase. Consequently large portion of the matrix was under a loading state with a larger stress level than the norminal applied stress. Further addition of silver to 13 vol% reduces the tangent modulus which might be due to higher amount of less compliant phase and the increasing porosity as the relative density of 13 vol% composite is obvious smaller than others (refer to Table 6.1).

6.3 Constitutive model development

To describe the hysteretic response of Ag/$BaTiO_3$ composites under the uniaxial compressive testing, a simple one-dimensional constitutive model was presented that is based on the thermodynamics of irreversible process and multiple natural configurations. The formation of permanent strain under mechanical compressive loading for $BaTiO_3$ ceramics is attributed to the microstructural changes. These microstructural changes are associated to domain wall movement due to the rotation of the electric dipoles to the plane perpendicular to the applied force, and other possible mechanisms such as microcracking, grain boundary slipping, etc. In this study, two natural configurations, which are different stress-free configurations, associated with the original and final configurations of microstructures are considered in formulating the constitutive model. In the original configuration, i.e. before any external loading is applied, the dipoles are randomly distributed. Gradually increasing the external loading induces microstructural changes, i.e., dipole reorientations, and finally when the external load is sufficiently large it reaches the final configuration of microstructures (all rotatable dipoles have been reoriented). It is noted large stresses can also induce cracking, in addition to dipole reorientation, as shown in some of the specimens tested. In order to account for the effect of microstructural changes on the macroscopic responses of materials, we introduce a volume fraction α that measures the percentage of changes ($\alpha = 0$ the material in its original microstructures and $\alpha = 1$ the material with complete microstructural changes). The volume fraction α is used as the internal state variable. Detailed discussion on the constitutive model based on multiple natural configurations can be found in [192, 193].

The loading rate in the compression tests is 0.001 mm/s, which is slow and treated as quasi-static. The deformation is considered as isothermal and rate independent. Following Doraiswamy et al. [194] the Gibbs free energy per unit volume is introduced as a function of the stress σ and the volume fraction α of domain transformation. For one dimensional problem the stress σ is given by axial force divided by cross-section area F/A, which is the first Piola stress; the strain ε is given by length change divided by original length $(L - L_0)/L_0$, which is the deformation gradient. These stress-strain measures are close to the true stress and strain measures when the deformations are relatively small, such as the ones observed in the tested specimens. The specific form of Gibbs free energy is assumed to be of the following form:

$$G = -\left[\alpha \frac{\sigma^2}{2E_2} + (1-\alpha)\frac{\sigma^2}{2E_1}\right] + B\alpha(\alpha - 1) - C\alpha \tag{6.1}$$

where the first term in bracket on the right hand side represents a linear combination of the elastic strain energy of the initial configuration and the final configuration; the second term represents the interaction energy between these two configurations; E_1 and E_2 are the elastic moduli of the initial configuration and the final configuration, respectively; B is a material constant that characterizes the interaction energy and needs to be identified from experimental data; C is a constant to keep the driving force zero at initial configuration as will be shown later.

For a purely mechanical process the macroscopic energy dissipation rate is given in terms of the difference between the stress power and the rate of change of Helmholtz potential:

$$\dot{D} = \sigma\dot{\varepsilon} - \dot{\psi} \tag{6.2}$$

where ψ is the Helmholtz free energy per unit volume, which is related to the Gibbs free energy by a Legendre transformation $\psi = G + \sigma\varepsilon_e$. Here ε_e is the elastic strain. Substituting the Helmholtz free energy in Eq. (6.2) and using the specific form of the Gibbs free energy, the rate of energy dissipation can be reformulated:

$$\dot{D} = -\left(\frac{\partial G}{\partial \sigma} + \varepsilon_e\right)\dot{\sigma} + \sigma\left(\dot{\varepsilon} - \dot{\varepsilon}_e\right) - \frac{\partial G}{\partial \alpha}\dot{\alpha} \tag{6.3}$$

The second law of thermodynamics requires the energy dissipation to be nonnegative in a closed loading cycle. Employing the standard reasoning in continuum thermodynamics, the reversible strain ε_e can be expressed as a linear combination of the elastic strains of the two configurations,

$$\varepsilon_e = -\frac{\partial G}{\partial \sigma} = \alpha\frac{\sigma}{E_2} + \left(1-\alpha\right)\frac{\sigma}{E_1} \tag{6.4}$$

Consequently,

$$\dot{D} = \sigma\left(\dot{\varepsilon} - \dot{\varepsilon}_e\right) - \frac{\partial G}{\partial \alpha}\dot{\alpha} \tag{6.5}$$

Hence, two sources contributing to the rate of dissipation are identified. The first term in the right hand side of Eq. (6.5) represents the contribution from the permanent strain due to microstructural changes. The second term represents the process of microstructural changes. i.e., reorientation of dipole moments, which is the Gibbs free energy difference between the two configurations. As explained above the volume fraction of domain change is used to characterize the extent of dipole reorientation, so a natural assumption about the permanent strain is that it is proportional to α,

$$\varepsilon - \varepsilon_e = \varepsilon_{\max} \alpha \tag{6.6}$$

where $\varepsilon_{\max}$ is the largest possible remnant strain obtained when all the domains have been transformed to the final configuration. It is a material constant and can be estimated, which will be shown later. Substituting Eq. (6.6) to Eq. (6.5) the dissipation rate reduces to:

$$\dot{D} = \left(\sigma \varepsilon_{\max} - \frac{\partial G}{\partial \alpha} \right) \dot{\alpha} \tag{6.7}$$

As a result, the internal state variable can be identified as the volume fraction α of domain change, and the associated driving force is $F = \sigma \varepsilon_{\max} - \partial G / \partial \alpha$. As pointed out in [194], $\dot{D}$ as a macroscopic rate of dissipation, can be negative. However, the net energy dissipation in a closed loading cycle must be non-negative. From the specified form of Gibbs free energy, the driving force is

$$F = \sigma \varepsilon_{\max} + \left(\frac{1}{2E_2} - \frac{1}{2E_1} \right) \sigma^2 - B(2\alpha - 1) + C \tag{6.8}$$

Hence, the driving force is a function of stress and volume fraction. From the relative change of the driving force, the constant C can be selected to make the driving force zero at the initial configuration. Combining Eqs. (6.4) and (6.6) the volume fraction α is expressed as a function of the stress σ and the strain ε,

$$\alpha = \frac{\varepsilon - \dfrac{\sigma}{E_1}}{\dfrac{\sigma}{E_2} - \dfrac{\sigma}{E_1} + \varepsilon_{\max}} \tag{6.9}$$

When the stress and strain are known the driving force and volume fraction can be calculated from Eqs. (6.8) and (6.9). In the theory of plasticity, the irreversible process is modeled by introducing an energy dissipation potential, from which the flow rule for the plastic strain can be deduced. In this work the Preisach operator was adopted to simulate the relation between the driving force and the volume fraction related to dipole reorientations, which can better handle the internal loading loops. The details of the theory of Preisach model is presented in Appendix for completion.

Preisach model (see section 6.5 for more details) is employed to simulate the relation between the driving force and the volume fraction of the domain transformation. The ultimate goal, however, is to predict the strain output given the stress input. The procedure is described as follows. Given the stress σ_n, strain ε_n, the volume fraction α_n at step n, and the stress input σ_{n+1} at step $n+1$, the current driving force F_{n+1} is calculated using Eq. (6.8) by substituting the volume fraction α_n from the previous step. The volume fraction α_{n+1} at current step $n+1$ can be predicted by the Preisach model. Having determined α_{n+1} the elastic strain $\varepsilon_{e,n+1}$ and the total strain ε_{n+1} at current loading step can be calculated using Eqs. (6.4) and (6.6), respectively. It should be noted that to calculate F_{n+1} the volume fraction α_n from the previous step is used instead of α_{n+1} at the current step, which is unknown at this stage. As a result, the stress increment $\Delta\sigma_{n+1} = \sigma_{n+1} - \sigma_n$ should be small to reduce the error. Also, iterative scheme can be adopted to reduce the chance of error accumulation through incremental steps.

6.4 Comparison of model prediction and experiment results

The Preisach operator was employed to simulate the relation between the driving force and the volume fraction of domain change rather than the entire relation between stress and strain. The original stress-strain data is transformed to driving force vs. volume fraction data by using Eqs. (6.8) and (6.9). Figure 6.3 shows a comparison of the stress-strain response for 10 vol% specimen and the corresponding driving force vs. volume fraction curve using the material constants characterized later in this section. As mentioned in section 6.2 that toe region exist in the stress-strain experiment data at lower loading levels due to the possible unparalleled sample surfaces. To get a better prediction it is reasonable to remove such toe region from the experiment data. As shown in Figure 6.3 the driving force vs. volume fraction curve has similar trend with the stress-strain data.

In order to use the model presented in previous section to predict the hysteretic response of Ag/BaTiO$_3$ composite, the model parameters need to be identified from the experimental data. There are two sets of parameters. One set is introduced in the part of model development where the thermodynamics of the material is considered, namely E_1, E_2, B, and C in Gibbs free energy and the maximum available permanent strain $\varepsilon_{\max}$.

These constants are characteristics of the material. For instance, E_1 is the elastic constant at the initial configuration and can be calculated by the slope at the initiation of loading as shown in Figure 6.3 (a). Also labeled in Figure 6.3 (a) is the elastic constant E_2 at the final configuration given by the tangent modulus at the initial stage of unloading. Unless microcracking is introduced at higher stresses, E_2 normally always has a larger value than E_1 for each loading cycle because at the final configuration more dipoles have been reoriented leading to a stiffer material response. The parameter B characterizes the interactional energy between different configurations and is proportional to the area of hysteresis as discussed in [192]. A value for it is chosen to ensure a good fit between the predictions and the experimental data, assuming that $\varepsilon_{\max}$ is resulting only from dipole reorientation. A parametric study of the influence of parameter B on the model prediction will be present later in this section. The parameter C is chosen to impose the driving force zero at the initial configuration, which in this study C=-B. The parameter $\varepsilon_{\max}$ characterizes the maximum extent of permanent strain. Under a compressive stress the maximum permanent strain can be reached when all the *c*-axes of the tetragonal crystal lattice are situated as close as possible to the plane perpendicular to the direction of loading [14]. By simulating 100,000 tetragonal unit cells with randomly distributed initial orientation [148] it is shown that under compressive stress,

$$\varepsilon_{\max} = 0.4035\frac{c-a}{a} \tag{6.10}$$

where c and a are the lattice parameters of $BaTiO_3$ single crystal. $\varepsilon_{spon} = (c-a)/a$ represents the spontaneous strain of a unit cell with respect to the undistorted state. Theoretical values of lattice parameter c and a for $BaTiO_3$ are calculated in [195] which are $3.994\ \dot{\mathrm{A}}$ and $3.943\ \dot{\mathrm{A}}$, respectively, leading to a maximum permanent strain $\varepsilon_{\max}$ of 0.52%.

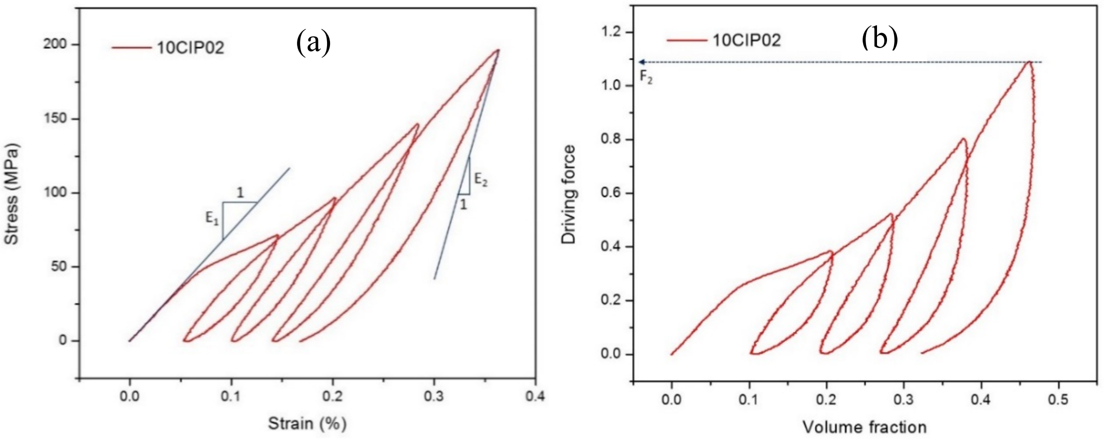

Figure 6.3 Comparison of the stress-strain hysteresis and the corresponding driving force vs. volume fraction curve: (a) stress-strain hysteresis for 10CIP02 specimen; (b) driving force vs. volume fraction curve. The elastic constants at two configurations are labeled in (a) and the Preisach parameter F_2 is labeled in (b).

The other set of parameters $F_{\min}$ and $F_{\max}$ defines the density distribution function, i.e. the Preisach triangle, and is related to the Preisach model, but not to the material itself. They should be chosen to ensure a better fitting of the experimental data. As shown in Figure 6.3 (b) $F_{\max}$ is chosen to be the largest value of the driving force. The reason is that if a value smaller than the largest driving force is assigned to $F_{\max}$ the material response at the stress level leading to a driving force larger than would be purely elastic. The experimental data, however, show that at the largest stress level in the test the material response is still dissipative and the permanent strain has not yet saturated. On the other hand, if a value larger than th$F_{\max}$e largest driving force is assigned to $F_{\max}$ the entries of the weight vector corresponding to the hystron elements with upper threshold bigger than $F_{\max}$ will not be well estimated because all of the training data are obtained at driving force levels lower than $F_{\max}$. Consequently, the Preisach model predictions at high stress levels would deviate significantly from the experimental data. The deformation of polycrystalline $BaTiO_3$ ceramic is unsymmetrical due to the fact that the amount of dipoles capable of being reoriented is different under compression and under tension. As shown in (Fröhlich 2001), the maximum permanent strains under compression and under tension are $\varepsilon_{\max}^{com} = 0.4035\varepsilon_{spon}$ and $\varepsilon_{\max}^{ten} = 0.5520\varepsilon_{spon}$, respectively. Since the difference is not significant and the experimental data are limited to compressive tests, the parameter $F_{\min}$ is chosen to be the negative of $F_{\max}$.

A parametric study was first carried out to investigate the effects of the model parameter B on the hysteretic responses for $Ag/BaTiO_3$ composite. Four different values for B were selected and the predictions were compared to the experiment data in Figure 6.4. The weight vector $\vec{w}$ for the hystron elements was estimated using limited data points as shown by the circle markers in Figure 6.4. The model predictions of the outer loading/unloading cycle do not depend on the values of B, while the inner loading/unloading loops depend on the value of parameter B. With relatively larger absolute values of B as shown in Figure 6.4 (a) and (b), the predicted inter loops have smaller enclosing areas than the experimental measurement, corresponding to smaller energy dissipation. With $B = -1.0$ the predicted response for the first inner loop is nearly elastic as shown in Figure 6.4 (a). Deceasing the absolute value of B the predicted energy dissipation increases. In Figure 6.4 (c) and (d) the predicted energy dissipation for the first loop is smaller than the experimental measurement, while larger for the latter two inner loops. In all of the case considered here the parameter B is chosen to be -0.01, since it leads to relatively better predictions of the inner loops.

The model parameters for Ag/BaTiO$_3$ composites with varying silver contents are given in Table 6.3. The material constants E_1 and E_2 are adopted from Table 6.2 and listed here for completion. The prediction capability of Preisach model depends on the number of hystrons in the Preisach triangle. In this work each right-angle side of the Preisach triangle is divided into 400 intervals corresponding to a total number of 80601 hystrons.

Table 6.3 Model parameters for Ag/BaTiO$_3$ composites with varying silver content.

	Volume fraction of silver			
	0 vol%	5 vol%	10 vol%	13 vol%
E_1 (GPa)	90.5	96.9	127.3	120.3
E_2 (GPa)	130.0	117.0	208.4	178.3
$F_{\max}$ (MPa)	0.967	0.504	0.973	0.747
B (MPa)	-0.01	-0.01	-0.01	-0.01
C (MPa)	0.01	0.01	0.01	0.01

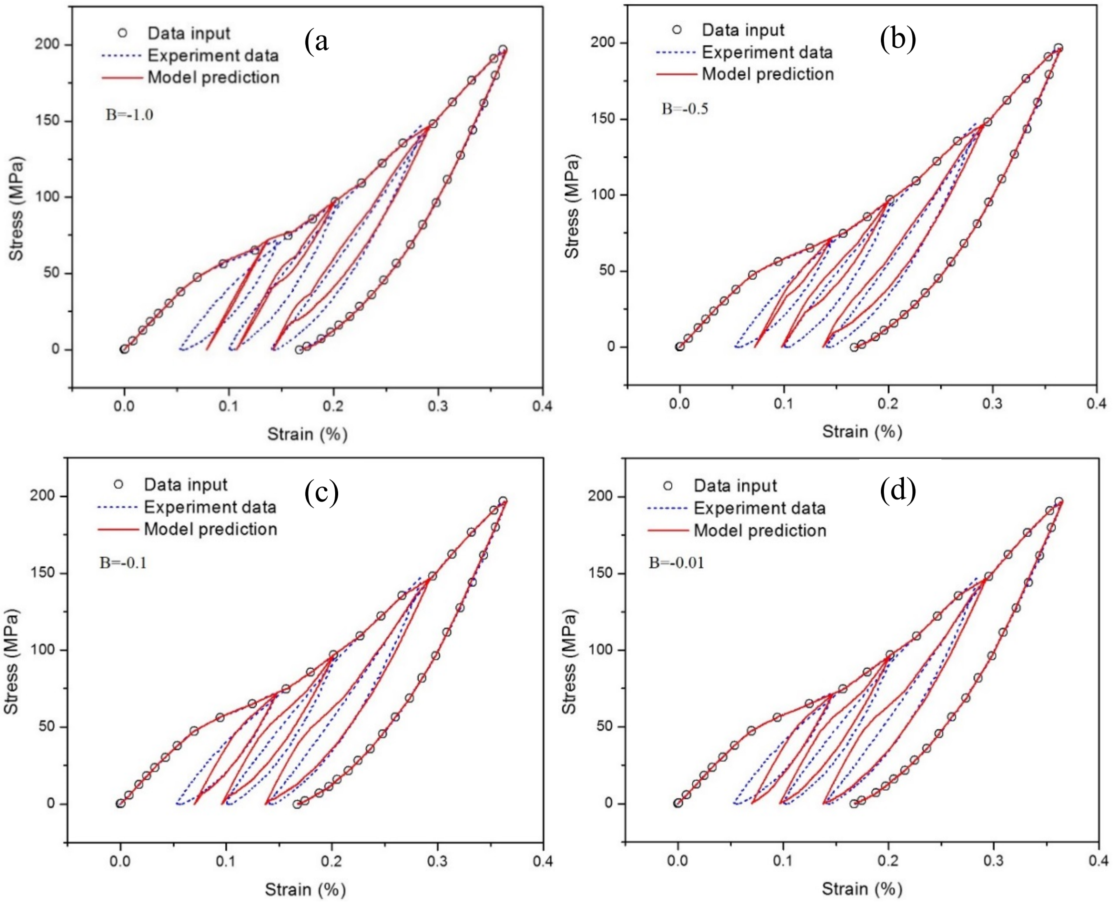

Figure 6.4 Parametric study of the effects of model parameter *B* on the predictions of ferroelastic hysteresis for 10 vol% Ag/BaTiO$_3$ composite: (a) *B*=-1.0; (b) *B*=-0.5; (c) *B*=-0.1; (d) *B*=-0.01.

The accuracy of model predictions is strongly influenced by the estimation of weight vector $\vec{w}$ for the discretized hystron elements and the number of data input. For instance, testing may only be carried out for the outer loading/unloading cycle, and the inner loading loops responses need to be predicted. It is also possible that experimental data from the outer cycle and also some inner loop at certain loading level are available, and the hysteretic responses of inner loops at other loading levels need to be predicted. The model predictions using different data input were investigated and the results are shown in Figure 6.5 for 10 vol% composite specimen 10CIP02. The input data in Figure 6.5 (a) are from the outer cycle and the first inner loop, while in Figure 6.5 (b) the input data are from all loading/unloading cycles. It is evident that with more input data the prediction becomes better, not only on the loading and unloading curves of the inner loop, but also the area it enclosed, corresponding to the energy dissipation. The improved performance of the model is from estimating the weight vector $\vec{w}$ with more input data.

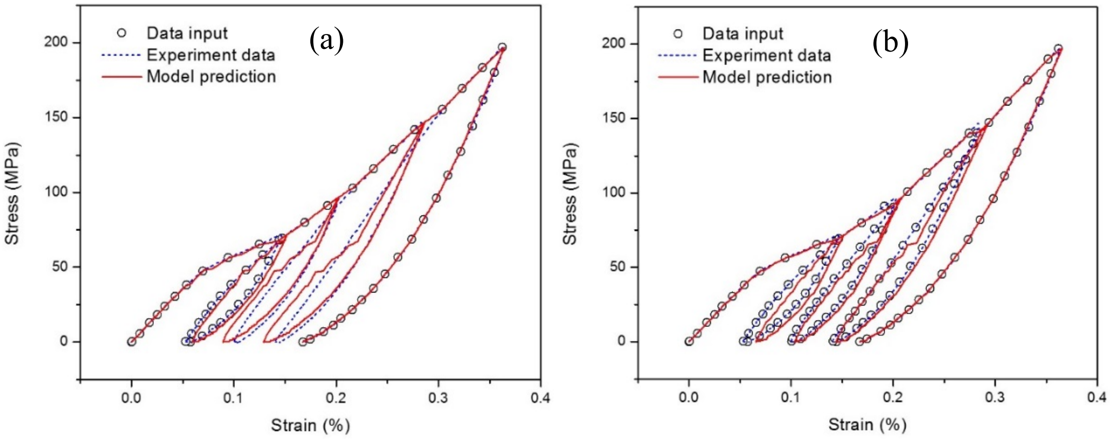

Figure 6.5 Comparison of the model predictions using different data input for 10 vol% composite specimen 10CIP02. The input data in (a) are from the outer cycle and the first inner loop experiment data, while in (b) the input data are from all loading/unloading cycles.

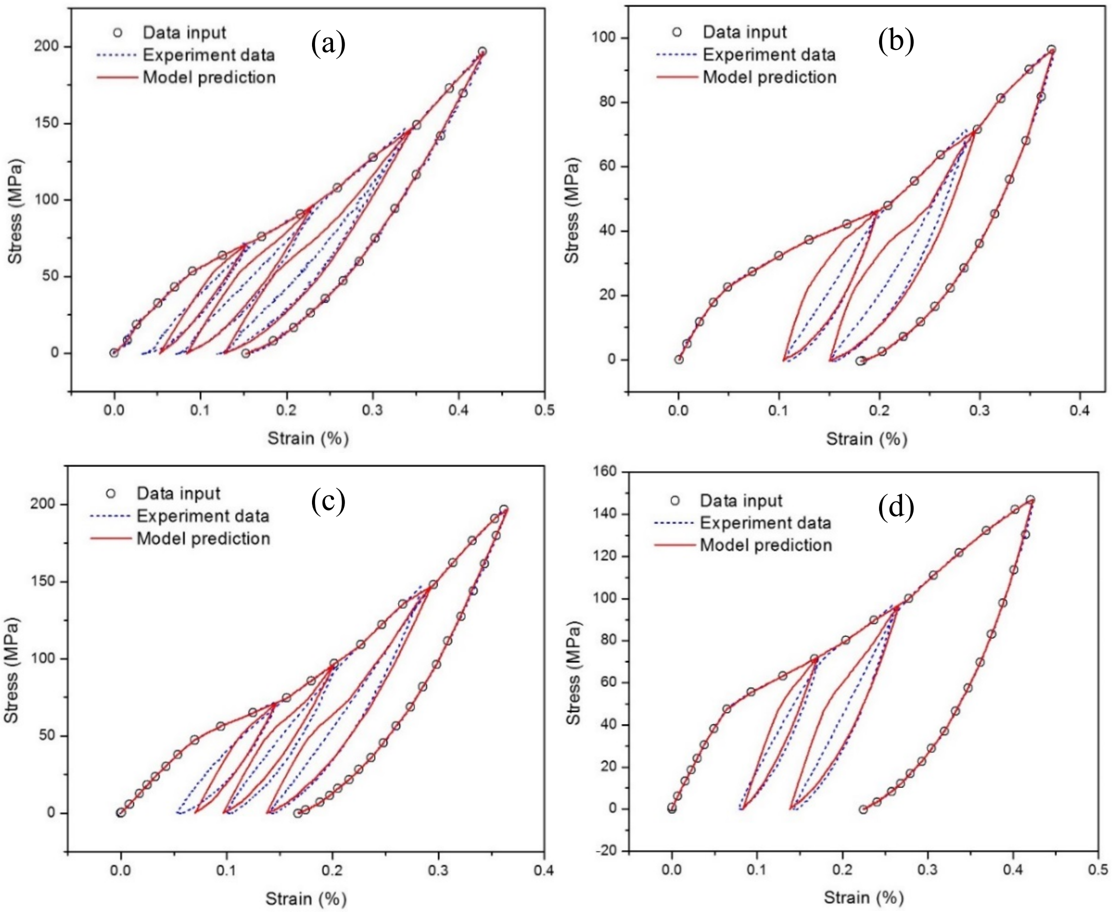

Figure 6.6 Model predictions for Ag/BaTiO$_3$ composite with varying silver content. The input data are from only the outer cycles as indicated by the circle makers: (a) Pure BaTiO$_3$ ceramic specimen 00CIP02; (b) 5 vol% composite specimen 05CIP02; (c) 10 vol% composite specimen 10CIP02; (d) 13 vol% composite specimen 13CIP02.

Model predictions for Ag/BaTiO$_3$ composite with varying silver content are plotted in Figure 6.6. Only data from the outer cycle are used to estimate the weight vector $\vec{w}$. The predictions capture the features of the hysteresis loops. The predicted unloading curves are very close to the experimental measurement, and the slope is also well estimated. However, it overestimates the energy dissipation for the inner loops. The predictions can be significantly improved when the input data with one inner loop are also incorporated in determining the weight factor as shown in Figure 6.5 (a). It is noted that in the model predictions for every inner loop the loading and unloading curves intersect with each other at the point located in the outer cycle, the so called wiping out phenomenon, which is a characteristics of the classical Preisach model. However, in the experimental measurement the loading curve did not intersect the unloading curve at its highest point. For Ag/$BaTiO_3$ composite with 5 vol% and 13 vol% silver composition the specimen were broken before reaching the loading stress level of 200 MPa. The predictions using the data from the loading curve up to the breaking point as input instead of the largest available outer cycle are plotted in Figure 6.7. The key features of the hysteretic response are captured by the model. Such predictions are usefully when cyclic material response is needed but only one loading-unloading test was available.

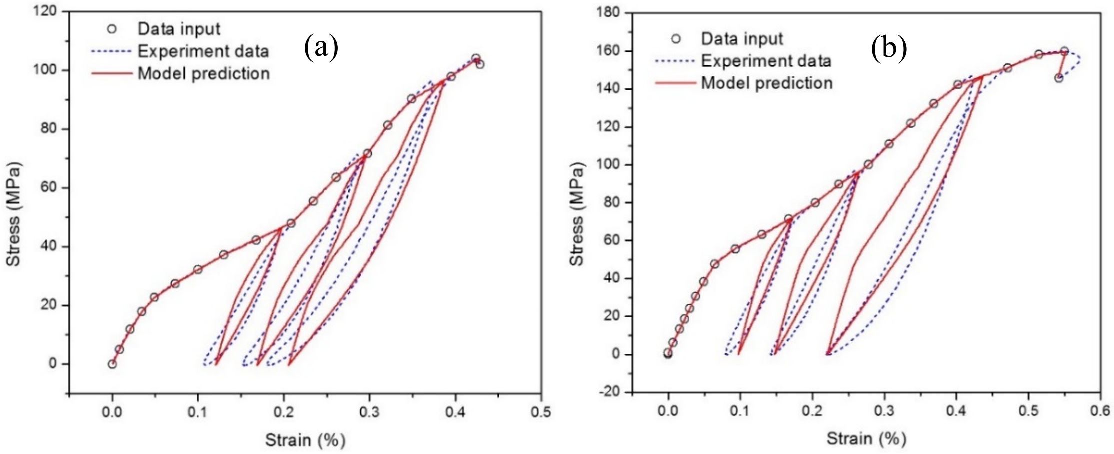

Figure 6.7 Model predictions for (a) 5 vol% composite specimen 05CIP02 and (b) 13 vol% composite specimen 13CIP02. Note that since the samples broke at the largest loading stress level the input data are only from the loading curves of the outer cycle.

6.5 Preisach model

The volume fraction α is defined as a weighted superposition of kernels of the Preisach operator [196],

$$\alpha(t) = \iint\limits_S K_F[v](t)\, w(F_1, F_2)\, ds \tag{6.11}$$

where $K_F[v](t)$ is the kernel operator; $w(F_1, F_2)$ is a continuous density function with support over the Preisach triangle as shown in Figure 6.8 (b). The classical Preisach kernel (hystron) is depicted on Figure 6.8 (a) with thresholds F_1 and F_2. In this work, F_1 and F_2 represent the two driving force thresholds and the output is the volume fraction α. The arrows in the figure indicate the flow direction of the driving force. If the driving force increases beyond the upper threshold value F_2 the hystron will be triggered on, leading to a volume fraction output. On the other hand, the hystron will be switched off if the driving force decreases below the lower threshold value F_1. Hence the kernel operator in the Preisach model is depicted by the following formula [197],

$$K_F[v](t) = \begin{cases} K_F[v](0) & \text{if } \tau(t) = \varnothing \\ -1 & \text{if } \tau(t) \neq \varnothing \text{ and } v(\max \tau(t)) = F_1 \\ +1 & \text{if } \tau(t) \neq \varnothing \text{ and } v(\max \tau(t)) = F_2 \end{cases} \tag{6.12}$$

where $\tau(t)$ is a set of time instances when the driving force crosses the two threshold values,

$$\tau(t) = \{ t_i \in (0, t] \mid v(t_i) = F_1 \text{ or } v(t_i) = F_2 \} \tag{6.13}$$

The initial condition for the kernel is

$$K_F\left[v\right]\left(0\right)=\begin{cases}-1 & \text{if } v\left(0\right)\leq F_1\\ +1 & \text{if } v\left(0\right)\geq F_2\end{cases} \tag{6.14}$$

As depicted in Figure 6.8 (b) the Preisach triangle is given as following,

$$S=\left\{\left(F_1,F_2\right)\mid F_{\min}\leq F_1\leq F_2\leq F_{\max}\right\} \tag{6.15}$$

The area in the shaded region represents the part of Preisach triangle where the kernel operator equals to $+1$ at current time and loading history, while the rest of the triangle is where the kernel operator equals to -1. If denoting the shaded area at time t with S_t^+ and the rest with S_t^+ the volume fraction output Eq. (6.11) can be simplified as

$$\alpha\left(t\right)=\iint\limits_{S_t^+} w\left(F_1,F_2\right)ds-\iint\limits_{S_t^-} w\left(F_1,F_2\right)ds \tag{6.16}$$

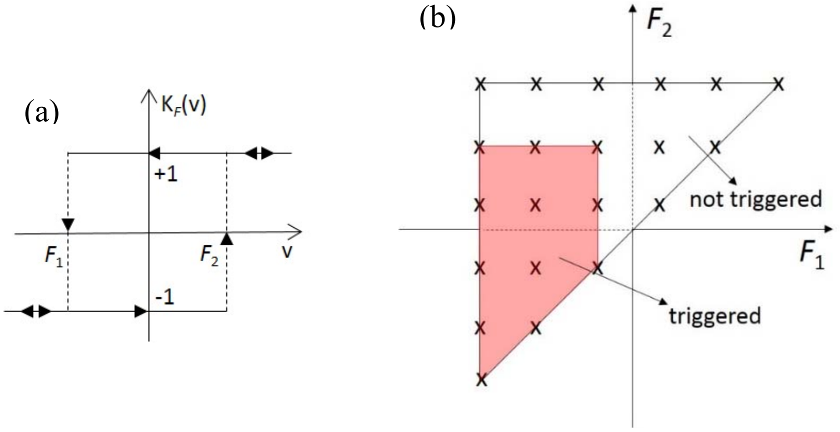

Figure 6.8 (a) Classical Preisach kernel (hystron) with threshold F_1 and F_2, v is the input variable and $K_F(v)$ is the kernel of Preisach model; (b) Preisach triangle. Each marker represents a discretized hystron element. Area under red represents the discretized hystrons that are triggered on under current time and loading history.

To calculate the volume fraction it is necessary to obtain the density distribution function $w\left(F_1, F_2\right)$ from the Preisach triangle. The density function is estimated by the driving force input F and the volume fraction output α from experimental data. Due to the finite number of experimental data the Preisach triangle usually is subdivided as shown in Figure 6.8 (b), where each marker represents a subdivision over which the density function is assumed to be constant. Consequently, each marker can be treated as a discretized hystron element as shown in Figure 6.8 (a). The hystron elements in the shaded area are triggered at current time and loading history, while the rest are still switched off. Assuming each right-angle side of the Preisach triangle is divided into m intervals, the total number of hystron elements is $N = \left(m+1\right)\left(m+2\right)/2$. As a result, the volume fraction in Eq. (6.16) at time t can be discretized as,

$$\alpha\left(t\right) = a_t^T \vec{w}, \tag{6.17}$$

where a_t is a column vector of dimension N at time t with the ith entry equals to $+1$ if the ith hystron element is triggered on and equals to -1 otherwise. $\vec{w}$ is the weight vector of dimension N with its entries representing the constant density for each hystron element. $\vec{w}$ needs to be estimated from the experimental data. Denoting the experimental data point at t_i as $\left(F_i, \alpha_i\right)$ the weight vector is estimated by solving the following quadratic optimization constraint:

$$\begin{aligned} \text{minimize:} \quad & \frac{1}{2}\left\| A\vec{w} - b \right\|_2^2 \\ \text{subject to:} \quad & \vec{w} \geq 0 \end{aligned} \tag{6.18}$$

where the coefficient matrix $A^T = \left(a_1, \cdots, a_n\right)$, a_i is the column vector in Eq. (6.17) at time t_i; $b^T = \left(\alpha_1, \cdots, \alpha_n\right)$ is the vector of volume fractions from experiment data; n is the total number of experiment data points. Note that usually the number n of data points is much smaller than the number N of total hystron elements, so the quadratic objective function in Eq. (6.18) is not strictly convex and possibly infinite number of optimal solution exist. The optimization problem Eq. (6.18) is solved using the CVX software, a Matlab-based program for convex optimization [198].

CHAPTER VII

CONCLUSIONS AND FUTURE STUDIES

This study focuses on understanding the effects of blending silver phase into barium titanate ceramic on its thermal, mechanical and dielectric properties. Both experimental techniques and numerical methodologies were employed though this investigation process. The major conclusions from previous chapters are summarized in the following paragraphs.

In Chapter II, Ag/$BaTiO_3$ composite with varying silver composition was fabricated by powder metallurgy method with two different cold compacting procedures (A and B). SEM image analysis shows that the microstructures, particle shape, and particle size of samples from these two procedures are comparable. Furthermore, no obvious difference in relative density was observed, which indicates that the final density is more controlled by sintering process rather than cold compaction. Energy-dispersive x-ray spectroscopy (EDS) and x-ray diffraction (XRD) analysis shows that silver did not chemically react with barium titanate and silver did not get oxidized. The only two existing phase is barium titanate and silver.

In Chapter III, the influence of silver phase and temperatures (-50 to 250 ^{o}C) on the effective thermal properties of Ag/$BaTiO_3$ composite was experimentally and numerically investigated. $BaTiO_3$ showed two phase transformations within the temperature range of interest. Thermal-mechanical analysis (TMA) shows the addition of silver in $BaTiO_3$ matrix has little influence on the phase transformation temperatures. CTE stays constant at each crystalline phase, but increases as $BaTiO_3$'s crystal structure changes from orthorhombic to tetragonal phase further to cubic. In addition, CTE slightly increases as the increase of silver content. Differential scanning calorimetry (DSC) was conducted to determine the heat capacity of Ag/$BaTiO_3$ composites. Our results show that heat capacity increases as the temperature increases and decreases as silver content increases. Phase transformation temperatures from DSC test stay constant as silver content increases, but are slightly different with that from the TMA measurement. Thermal conductivity and thermal diffusivity were measured by hot disk technique. Thermal conductivity is nearly constant at tetragonal and cubic phases, respectively, but smaller at cubic phase than that at tetragonal phase. Increase of silver content significantly enhanced the thermal conductivity of the composite due to the formation of thermal conductivity chains. Numerical results showed that microstructure introduced anisotropy is negligible and the effective properties are independent of loading directions. Our micromechanical models achieved macroscopic homogeneity. Effective CTE were shown to be insensitive to the yielding of silver phase and the elastic modulus of $BaTiO_3$ matrix. The prediction of effective CTE was in a good agreement with experimental results. The effective thermal conductivity with a constant temperature gradient BC gives a close predictions of experimental data. An investigation of local field shows that high stress and heat flux concentration exist in the thermal expansion and steady state heat transfer analyses, respectively.

In Chapter IV, a micromechanics model was developed to predict the various effective thermal properties, such as thermal conductivity, thermal diffusivity, and heat capacity, of composite materials. The model is based on transient heat transfer analysis.

Compared to micromechanics model based on steady state heat transfer analysis, the major advantage of this newly developed model lies in its ability to predict various effective thermal properties at the same time. Based on the assumption that the heat was transferred within an infinite 2D isotropic and homogeneous media, the average temperature, at each time instance, over the heat source area can be solved analytically as a nonlinear function of the thermal conductivity K and thermal diffusivity κ of the material. The average temperature over the heat source area was also calculated by finite element analysis. Then the effective material constants of the composite can be estimated by fitting the finite element calculated average temperature with the analytical solution by nonlinear regression. Sensitivity analysis was carried out to investigate the influence of small perturbations on the input data. Sensitivity analysis shows that estimations using data input from larger time instances are less sensitive to small perturbations in input data, and that 50 data points are enough for desired accuracy. Two kinds of heat source geometries were studied, i.e. concentric ring-shaped and disk-shaped. For these two geometries the predicted effective constants were very close, which makes the disk-shaped more preferable due to its uniform meshes, and hence less computational time. The study of particle size effect shows that convergence is reached for 500 reinforcement particles with a small relative standard deviation for the estimated material constants. The relative standard deviation for effective thermal conductivity prediction is smaller than that for effect thermal diffusivity. Consequently, the prediction for thermal conductivity has higher accuracy. Various effective thermal properties for Ag/$BaTiO_3$ composite were predicted using the newly developed micromechanics model and compared to both experimental and numerical results reported in [182]. The predicted effective thermal conductivity from transient analysis is close to that from steady state analysis. However predicted thermal properties underestimates the experimental results.

In Chapter V, the elastic constants and dielectric properties of Ag/$BaTiO_3$ composite with varying silver content (from 0 vol% to 10 vol%) were measured using resonant ultrasound spectroscopy (RUS) technique and dielectric (impedance) spectroscopy, respectively. The elastic constants measured include Young's modulus, shear modulus and Poisson's ratio, while the dielectric properties tested are relative permittivity and dielectric loss. To numerically study the various effective elastic and dielectric properties of the composites, two different micromechanics models were considered, one of which is based on realistic microstructures from scanning electron microscopy (SEM) images, and the other based on randomly generating spherical Ag particles within a $BaTiO_3$ matrix. All of the elastic constants decreases as the increase of silver composition because silver phase is softer. The relative permittivity decreases, while the dielectric loss increases as the testing frequency increases up to 1 KHz and then starts to decrease afterwards. The relative permittivity and dielectric loss changes with frequency follow the similar trends for the pure barium titanate ceramic and Ag/$BaTiO_3$ composites. However, at the same frequency the relative permittivity is much larger in composites than that of monolithic ceramics. On the contrary, dielectric loss only slightly increases as the addition of silver phase. Two peaks exist in the relative permittivity vs. temperature plot: one is around the orthorhombic to tetragonal phase transformation temperature, i.e. ~0 ^{o}C, and the other around the tetragonal to cubic phase transformation temperature, i.e. ~120 ^{o}C. The later peak is much sharper than the former one. Adding silver phase increases the magnitude of relative permittivity, but does not affect its trend with temperature. Micromechanics predictions of the effective properties from 2D and 3D models are very close. In addition, different boundary conditions (BC) were implemented to study their effects on the overall response of the composite. While the predictions of effective elastic constants do not depend on specific boundary condition, they strongly influence the prediction of effective relative permittivity. The constant electric potential gradient BC gives an extremely large prediction which is an upper bound, while the uniform flux leads to a lower bound. Experimentally measured relatively permittivity lies between the upper and lower bounds. One possible reason for such big fluctuation in predictions is the extremely high contrast in relative permittivity between silver and barium titanate. Due to the adding of silver particles stress and electric flux concentrations exit at the phase interfaces which increase as the increase of silver composition.

In Chapter VI, the hysteretic response of Ag/$BaTiO_3$ composite was investigated using experimental technique and a thermodynamically consistent constitutive model. Experimental results show that the largest portion of remnant strain was developed between the loading levels of 25 MPa and 100 MPa, which corresponds to extensive amount of energy dissipation. The unloading curve for each cycle is convex indicating a recovering of part of the reoriented dipoles when releasing the applied stress. Specimens with 5 vol% and 13 vol% silver composition were broken before the maximum stress was reached. The failure were ductile because a large amount of inelastic deformation was observed before the final cleavage and the fractured specimens showed a fracture angle of approximate 45 °C. The tangent modulus was calculated for each stress level at the initial stage of the unloading cycle. It was found that tangent modulus increases as the stress amplitude prior to unloading increases. The addition of silver phase up to 10 vol% also increases the tangent modulus due to the internal stress concentration. However, further addition of silver phase leads to a decrease of tangent modulus because the more introduced defects dwarfs the effect of stress concentration. A one-dimensional constitutive model based on the thermodynamics of irreversible process was presented to model the hysteretic response from experiment. The key features can be captured by the model predictions using data input only from the outer loading/unloading cycle. However, the energy dissipation for inner loading loops was often overestimated, especially at higher stress levels. Providing data input for one inner loop can significantly improve the model predictions. The presented one-dimensional constitutive model combining irreversible thermodynamics and Preisach operator is capable of simulating the hysteretic stress-strain response with fair accuracy by using only limited data input.

To further examine the influences of silver phase on the macroscopic properties of Ag/$BaTiO_3$ composite the following investigations are suggested to be carried out in the future:

1. Various linear properties, such as thermal, elastic and dielectric, were measured in this work. However, to fully understanding the effects of adding silver phase the mechanical-electrical couple coefficients, i.e. piezoelectric constants, of the composite should also be measured and analyzed.

2. The effective transportation properties was underestimated by the micromechanics models built in this work, due its incapability of including certain mechanisms of transportation phenomenon. Consequently, new micromechanics models should be developed in the future to give a better prediction.
3. As shown in the micromechanics analysis, high electrical flux concentration exists within Ag/$BaTiO_3$ composite because of silver particles, even the nominal value is small. Consequently, nonlinear ferroelectric testing and modeling should be conducted, which would enhance the understanding of its response under electrical loading. Furthermore, it will also help the poling process of the specimens, because poling is carried out at high electrical loadings.
4. Before poling the dipoles are random distributed in the ceramics and no net polarization exists. Consequently, the material symmetry is isotropic. However, it changes to transversely isotropic after poling due the reorientation of dipoles. Consequently, material properties of poled specimens are suggested to be measured in the future.

REFERENCES

1. Hennings, D., *Barium titanate based ceramic materials for dielectric use.* International Journal of High Technology Ceramics, 1987. **3**(2): p. 91-111.
2. Sakabe, Y., *Multilayer ceramic capacitors.* Current Opinion in Solid State and Materials Science, 1997. **2**(5): p. 584-587.
3. Kishi, H., Y. Mizuno, and H. Chazono, *Base-metal electrode-multilayer ceramic capacitors: past, present and future perspectives.* Japanese Journal of Applied Physics, 2003. **42**(1R): p. 1-15.
4. Takenaka, T., K.-i. Maruyama, and K. Sakata, *(Bi1/2Na1/2) TiO3-BaTiO3 system for lead-free piezoelectric ceramics.* Japanese Journal of Applied Physics, 1991. **30**(9S): p. 2236-2239.
5. Karaki, T., K. Yan, and M. Adachi, *Barium titanate piezoelectric ceramics manufactured by two-step sintering.* Japanese Journal of Applied Physics, 2007. **46**(10S): p. 7035-7038.
6. Ikushima, H. and S. Hayakawa, *Electrical properties of Ag-doped barium titanate ceramics.* Japanese Journal of Applied Physics, 1965. **4**(5): p. 328-336.
7. Chen, C. and W. Tuan, *Mechanical and dielectric properties of BaTiO3/Ag composites.* Journal of Materials Science Letters, 1999. **18**(5): p. 353-354.
8. Halder, N., et al., *Effect of silver addition on the dielectric properties of barium titanate based low temperature processed capacitors.* Materials Research Bulletin, 1999. **34**(4): p. 545-550.

9. Chen, C.Y. and W.H. Tuan, *Effect of silver on the sintering and grain‐growth behavior of barium titanate.* Journal of the American Ceramic Society, 2000. **83**(12): p. 2988-2992.

10. Panteny, S., C. Bowen, and R. Stevens, *Characterisation of barium titanate-silver composites, part I: Microstructure and mechanical properties.* Journal of Materials Science, 2006. **41**(12): p. 3837-3843.

11. Kojima, T., et al., *Fabrication of BaTiO3/Ag composites using uniform Ag-deposited BaTiO3 particles.* Journal of the Ceramic Society of Japan, 2009. **117**(1372): p. 1328-1332.

12. Sánchez-Jiménez, P.E., et al., *Mechanochemical preparation of BaTiO 3–Ni nanocomposites with high dielectric constant.* Composite Structures, 2010. **92**(9): p. 2236-2240.

13. Vijatović, M., J. Bobić, and B. Stojanović, *History and challenges of barium titanate: Part I.* Science of Sintering, 2008. **40**(2): p. 155-165.

14. Kamlah, M., *Ferroelectric and ferroelastic piezoceramics–modeling of electromechanical hysteresis phenomena.* Continuum Mechanics and Thermodynamics, 2001. **13**(4): p. 219-268.

15. Jona, F. and G. Shirane, *Ferroelectric crystals*. Vol. 1. 1962: Pergamon.

16. Vijatović, M., J. Bobić, and B. Stojanović, *History and challenges of barium titanate: Part II.* Science of Sintering, 2008. **40**(3): p. 235-244.

17. Jaffe, B., *Piezoelectric ceramics*. Vol. 3. 2012: Elsevier.

18. Cho, W.-S., *Structural evolution and characterization of BaTiO 3 nanoparticles synthesized from polymeric precursor.* Journal of Physics and Chemistry of Solids, 1998. **59**(5): p. 659-666.

19. Forsbergh Jr, P.W., *Domain structures and phase transitions in barium titanate.* Physical Review, 1949. **76**(8): p. 1187-1201.

20. Frazer, B., H. Danner, and R. Pepinsky, *Single-crystal neutron analysis of tetragonal BaTi O 3.* Physical Review, 1955. **100**(2): p. 745-746.

21. Zhong, W., D. Vanderbilt, and K. Rabe, *Phase transitions in BaTi O 3 from first principles.* Physical Review Letters, 1994. **73**(13): p. 1861-1864.

22. Lines, M.E. and A.M. Glass, *Principles and applications of ferroelectrics and related materials*. 1977: Oxford University Press.

23. Moulson, A.J. and J.M. Herbert, *Electroceramics: materials, properties, applications*. 2003: John Wiley & Sons.

24. Arlt, G. and D. Hennings, *Dielectric properties of fine ‐ grained barium titanate ceramics.* Journal of Applied Physics, 1985. **58**(4): p. 1619-1625.

25. Chaim, R., et al., *Sintering and densification of nanocrystalline ceramic oxide powders: a review.* Advances in Applied Ceramics, 2008. **107**(3): p. 159-169.

26. Xing-Xiang, J., H. Dong-Shen, and W. Luqian, *Sintering characteristics of microfine zirconia powder.* Journal of Materials Science, 1994. **29**(1): p. 121-124.

27. Duran, P., et al., *Nanostructured and near defect-free ceramics by low-temperature pressureless sintering of nanosized Y-TZP powders.* Journal of Materials Science, 1997. **32**(17): p. 4507-4512.

28. Ting, J.-M. and R. Lin, *Effect of particle-size distribution on sintering.* Journal of Materials Science, 1994. **29**(7): p. 1867-1872.

29. Shiau, F.S., T.T. Fang, and T.H. Leu, *Effect of particle ‐ size distribution on the microstructural evolution in the intermediate stage of sintering.* Journal of the American Ceramic Society, 1997. **80**(2): p. 286-290.

30. Yang, X. and M. Rahaman, *Thin films by consolidation and sintering of nanocrystalline powders.* Journal of the European Ceramic Society, 1997. **17**(4): p. 525-535.

31. Harmer, M. and R. Brook, *Fast firing – microstructrual benefits.* Transactions and Journal of British Ceramic Society, 1981. **80**(5): p. 147-149.

32. Mostaghaci, H. and R. Brook, *Fast firing of nonstoichiometric BaTiO sub/ 3.* Transactions and Journal of the British Ceramic Society, 1981. **80**: p. 148-149.

33. Ragulya, A. and V. Skorokhod, *Rate-controlled sintering of ultrafine nickel powder.* Nanostructured Materials, 1995. **5**(7): p. 835-843.

34. Huckabee, M.L. and H. Palmour, *Rate controlled sintering of fine-grained Al2O3.* American Ceramic Society Bulletin, 1972. **51**(7): p. 574-576.

35. Gilde, G.A., P.J. Patel, and M. Patterson. *Comparison of hot-pressing, rate-controlled sintering, and microwave sintering of magnesium aluminate for*

optical applications. In *AeroSense'99*. International Society for Optics and Photonics, 1999. p. 94 -104.

36. Huckabee, M., T. Hare, and H. Palmour III, *Rate controlled sintering as a processing method*. In *Processing of Crystalline Ceramics*. Springer US, 1978. p. 205-215.

37. Ragulya, A., *Rate-controlled synthesis and sintering of nanocrystalline barium titanate powder.* Nanostructured Materials, 1998. **10**(3): p. 349-355.

38. Mishra, R.S., C.E. Lesher, and A.K. Mukherjee, *High ‐pressure sintering of nanocrystalline γAl2O3.* Journal of the American Ceramic Society, 1996. **79**(11): p. 2989-2992.

39. Selvam, P. and K. Yvon, *Synthesis of Mg2FeH6, Mg2CoH5 and Mg2NiH4 by high-pressure sintering of the elements.* International Journal of Hydrogen Energy, 1991. **16**(9): p. 615-617.

40. Rong, X.-Z., et al., *High-pressure sintering of cBN-TiN-Al composite for cutting tool application.* Diamond and Related Materials, 2002. **11**(2): p. 280-286.

41. Takano, Y., et al., *Superconducting properties of MgB2 bulk materials prepared by high pressure sintering.* arXiv preprint cond-mat/0102167, 2001.

42. Liao, S.-C., et al., *High pressure/low temperature sintering of nanocrystalline alumina.* Nanostructured Materials, 1998. **10**(6): p. 1063-1079.

43. Moriyoshi, Y. and W. Komatsu, *Kinetics of initial combined sintering.* Yogyo Kyokai Shi, 1973. **81**(3): p. 102-107.

44. Filipović, S., et al., *Advantages of combined sintering compared to conventional sintering of mechanically activated magnesium titanate.* Science of Sintering, 2014. **46**(3): p. 283-290.

45. Polotai, A.V., A.V. Ragulya, and C.A. Randall, *Preparation and size effect in pure nanocrystalline barium titanate ceramics.* Ferroelectrics, 2003. **288**(1): p. 93-102.

46. Chen, I.-W. and X.-H. Wang, *Sintering dense nanocrystalline ceramics without final-stage grain growth.* Nature, 2000. **404**(6774): p. 168-171.

47. Wang, X.H., P.L. Chen, and I.W. Chen, *Two‐step sintering of ceramics with constant grain‐size, I. Y2O3.* Journal of the American Ceramic Society, 2006. **89**(2): p. 431-437.

48. Wang, C.-J., C.-Y. Huang, and Y.-C. Wu, *Two-step sintering of fine alumina–zirconia ceramics.* Ceramics International, 2009. **35**(4): p. 1467-1472.

49. Mazaheri, M., A. Zahedi, and S. Sadrnezhaad, *Two‐step sintering of nanocrystalline ZnO compacts: Effect of temperature on densification and grain growth.* Journal of the American Ceramic Society, 2008. **91**(1): p. 56-63.

50. Lee, Y.I., et al., *Fabrication of dense nanostructured silicon carbide ceramics through two‐step sintering.* Journal of the American Ceramic Society, 2003. **86**(10): p. 1803-1805.

51. Karaki, T., et al., *Lead-free piezoelectric ceramics with large dielectric and piezoelectric constants manufactured from BaTiO3 nano-powder.* Japanese Journal of Applied Physics, 2007. **46**(2L): p. L97- L98.

52. Polotai, A., et al., *A novel approach to sintering nanocrystalline barium titanate ceramics.* Journal of the American Ceramic Society, 2005. **88**(11): p. 3008-3012.

53. Wang, X.H., et al., *Two‐step sintering of ceramics with constant grain‐size, II: BaTiO3 and Ni–Cu–Zn ferrite.* Journal of the American Ceramic Society, 2006. **89**(2): p. 438-443.

54. Zhou, L., et al., *Preparation and properties of lead zirconate stannate titanate sintered by spark plasma sintering.* Journal of the American Ceramic Society, 2004. **87**(4): p. 606-611.

55. Yucheng, W. and F. Zhengyi, *Study of temperature field in spark plasma sintering.* Materials Science and Engineering: B, 2002. **90**(1): p. 34-37.

56. Tiwari, D., B. Basu, and K. Biswas, *Simulation of thermal and electric field evolution during spark plasma sintering.* Ceramics International, 2009. **35**(2): p. 699-708.

57. Chen, W., et al., *Fundamental investigations on the spark plasma sintering/synthesis process: I. Effect of dc pulsing on reactivity.* Materials Science and Engineering: A, 2005. **394**(1): p. 132-138.

58. Anselmi-Tamburini, U., J. Garay, and Z. Munir, *Fundamental investigations on the spark plasma sintering/synthesis process: III. Current effect on reactivity.* Materials Science and Engineering: A, 2005. **407**(1): p. 24-30.

59. Omori, M., *Sintering, consolidation, reaction and crystal growth by the spark plasma system (SPS).* Materials Science and Engineering: A, 2000. **287**(2): p. 183-188.

60. Munir, Z., U. Anselmi-Tamburini, and M. Ohyanagi, *The effect of electric field and pressure on the synthesis and consolidation of materials: a review of the spark plasma sintering method.* Journal of Materials Science, 2006. **41**(3): p. 763-777.

61. Chaim, R., *Densification mechanisms in spark plasma sintering of nanocrystalline ceramics.* Materials Science and Engineering: A, 2007. **443**(1): p. 25-32.

62. Zhao, Z., et al. *Spark plasma sintering of nano-crystalline ceramics*. In *Key Engineering Materials*, vol. 264, p. 2297-2300. Trans Tech Publications, 2004.

63. Li, B., et al., *Densification of uniformly small-grained BaTiO3 using spark-plasma-sintering.* Materials Chemistry and Physics, 2003. **82**(1): p. 173-180.

64. Li, B., et al., *Dielectric properties of fine-grained BaTiO3 prepared by spark-plasma-sintering.* Materials Chemistry and Physics, 2004. **83**(1): p. 23-28.

65. Deng, X., et al., *Phase transitions in nanocrystalline barium titanate ceramics prepared by spark plasma sintering.* Journal of the American Ceramic Society, 2006. **89**(3): p. 1059-1064.

66. Zhao, Z., et al., *Grain-size effects on the ferroelectric behavior of dense nanocrystalline BaTiO 3 ceramics.* Physical Review B, 2004. **70**(2): p. 024107 1-8.

67. Chen, C.Y. and W.H. Tuan, *Evaporation of silver during cofiring with barium titanate.* Journal of the American Ceramic Society, 2000. **83**(7): p. 1693-1698.
68. George, S., N.I. Santha, and M.T. Sebastian, *Percolation phenomenon in barium samarium titanate–silver composite.* Journal of Physics and Chemistry of Solids, 2009. **70**(1): p. 107-111.
69. Chou, W. and W. Tuan, *Toughening and strengthening of alumina with silver inclusions.* Journal of the European Ceramic Society, 1995. **15**(4): p. 291-295.
70. MAHER, G.H., *Effect of silver doping on the physical and electrical properties of PLZT ceramics.* Journal of the American Ceramic Society, 1983. **66**(6): p. 408-413.
71. Hwang, H.J., et al., *Curie temperature anomaly in lead zirconate titanate/silver composites.* Journal of the American Ceramic Society, 1998. **81**(3): p. 709-712.
72. Panteny, S., C. Bowen, and R. Stevens, *Characterisation of barium titanate-silver composites part II: Electrical properties.* Journal of Materials Science, 2006. **41**(12): p. 3845-3851.
73. Speyer, R., *Thermal analysis of materials*. 1993: CRC Press.
74. Cahill, D.G., *Thermal conductivity measurement from 30 to 750 K: the 3ω method.* Review of Scientific Instruments, 1990. **61**(2): p. 802-808.
75. Cahill, D.G., M. Katiyar, and J. Abelson, *Thermal conductivity of a-Si: H thin films.* Physical Review B, 1994. **50**(9): p. 6077-6081.
76. Govorkov, S., et al., *A new method for measuring thermal conductivity of thin films.* Review of Scientific Instruments, 1997. **68**(10): p. 3828-3834.

77. Calzona, V., et al., *Fully automated apparatus for thermal diffusivity measurements on HTSC in high magnetic field.* Review of Scientific Instruments, 1993. **64**(3): p. 766-773.

78. Sawada, S. and G. Shirane, *Specific heat and thermal expansion of BaTiO3.* Journal of the Physical Society of Japan, 1949. **4**(1): p. 52-56.

79. Shirane, G. and A. Takeda, *Transition energy and volume change at three transitions in barium titanate.* Journal of the Physical Society of Japan, 1952. **7**(1): p. 1-4.

80. Rao, M.R. and A. Umarji, *Thermal expansion studies on ferroelectric materials.* Bulletin of Materials Science, 1997. **20**(7): p. 1023-1028.

81. He, Y., *Heat capacity, thermal conductivity, and thermal expansion of barium titanate-based ceramics.* Thermochimica Acta, 2004. **419**(1): p. 135-141.

82. Radovic, M., E. Lara-Curzio, and L. Riester, *Comparison of different experimental techniques for determination of elastic properties of solids.* Materials Science and Engineering: A, 2004. **368**(1): p. 56-70.

83. Bechmann, R., *Elastic, piezoelectric, and dielectric constants of polarized barium titanate ceramics and some applications of the piezoelectric equations.* The Journal of the Acoustical Society of America, 1956. **28**(3): p. 347-350.

84. Berlincourt, D. and H. Jaffe, *Elastic and piezoelectric coefficients of single-crystal barium titanate.* Physical Review, 1958. **111**(1): p. 143-148.

85. Dunn, M.L., *Effects of grain shape anisotropy, porosity, and microcracks on the elastic and dielectric constants of polycrystalline piezoelectric ceramics.* Journal of Applied Physics, 1995. **78**(3): p. 1533-1541.

86. Rödel, J. and W. Kreher, *Effective properties of polycrystalline piezoelectric ceramics.* Le Journal de Physique IV, 1999. **9**(PR9): p. 239-247.

87. Den Toonder, J., J. Van Dommelen, and F. Baaijens, *The relation between single crystal elasticity and the effective elastic behaviour of polycrystalline materials: theory, measurement and computation.* Modelling and Simulation in Materials Science and Engineering, 1999. **7**(6): p. 909-928.

88. Froehlich, A., A. Brueckner-Foit, and S. Weyer. *Effective properties of piezoelectric polycrystals*. In *SPIE's 7th Annual International Symposium on Smart Structures and Materials*. International Society for Optics and Photonics, 2000. p. 279-287.

89. Dent, A., et al., *Effective elastic properties for unpoled barium titanate.* Journal of the European Ceramic Society, 2007. **27**(13): p. 3739-3743.

90. Duran, P., et al., *Densification behaviour, microstructure development and dielectric properties of pure BaTiO 3 prepared by thermal decomposition of (Ba, Ti)-citrate polyester resins.* Ceramics International, 2002. **28**(3): p. 283-292.

91. Arya, P.R., et al., *Polymeric citrate precursor route to the synthesis of nano-sized barium lead titanates.* Materials Research Bulletin, 2003. **38**(4): p. 617-628.

92. Buscaglia, V., et al., *Nanostructured barium titanate ceramics.* Powder Technology, 2004. **148**(1): p. 24-27.

93. Boulos, M., et al., *Hydrothermal synthesis of nanosized BaTiO 3 powders and dielectric properties of corresponding ceramics.* Solid State Ionics, 2005. **176**(13): p. 1301-1309.

94. Stojanovic, B., et al., *Ferroelectric properties of mechanically synthesized nanosized barium titanate.* Ferroelectrics, 2005. **319**(1): p. 65-73.

95. Vinothini, V., P. Singh, and M. Balasubramanian, *Synthesis of barium titanate nanopowder using polymeric precursor method.* Ceramics International, 2006. **32**(2): p. 99-103.

96. Simon-Seveyrat, L., et al., *Re-investigation of synthesis of BaTiO 3 by conventional solid-state reaction and oxalate coprecipitation route for piezoelectric applications.* Ceramics International, 2007. **33**(1): p. 35-40.

97. Zgonik, M., et al., *Dielectric, elastic, piezoelectric, electro-optic, and elasto-optic tensors of BaTiO 3 crystals.* Physical Review B, 1994. **50**(9): p. 5941-5949.

98. Guo, L., et al., *Microwave hydrothermal synthesis of barium titanate powders.* Materials Letters, 2006. **60**(24): p. 3011-3014.

99. Kim, H.T. and Y.H. Han, *Sintering of nanocrystalline BaTiO 3.* Ceramics International, 2004. **30**(7): p. 1719-1723.

100. Ren, P., et al., *Effects of silver addition on microstructure and electrical properties of barium titanate ceramics.* Journal of Alloys and Compounds, 2011. **509**(22): p. 6423-6426.

101. Böhm, H.J., *A short introduction to basic aspects of continuum micromechanics.* Cdl-fmd Report, 2013. **3**.

102. Eshelby, J.D. *The determination of the elastic field of an ellipsoidal inclusion, and related problems*. In *Proceedings of the Royal Society of London A: Mathematical, Physical and Engineering Sciences*. The Royal Society, 1957. p. 376-396.

103. Mori, T. and K. Tanaka, *Average stress in matrix and average elastic energy of materials with misfitting inclusions.* Acta Metallurgica, 1973. **21**(5): p. 571-574.

104. Hill, R., *A self-consistent mechanics of composite materials.* Journal of the Mechanics and Physics of Solids, 1965. **13**(4): p. 213-222.

105. Turner, P.S., *The problem of thermal-expansion stresses in reinforced plastics*. 1942: National Advisory Committee for Aeronautics.

106. Kerner, E., *The elastic and thermo-elastic properties of composite media.* Proceedings of the Physical Society. Section B, 1956. **69**(8): p. 808-813.

107. Schapery, R.A., *Thermal expansion coefficients of composite materials based on energy principles.* Journal of Composite Materials, 1968. **2**(3): p. 380-404.

108. Fahmy, A. and A. Ragai, *Thermal ‐ expansion behavior of two ‐ phase solids.* Journal of Applied Physics, 1970. **41**(13): p. 5108-5111.

109. Rosen, B.W. and Z. Hashin, *Effective thermal expansion coefficients and specific heats of composite materials.* International Journal of Engineering Science, 1970. **8**(2): p. 157-173.

110. Cheng, S. and R. Vachon, *The prediction of the thermal conductivity of two and three phase solid heterogeneous mixtures.* International Journal of Heat and Mass Transfer, 1969. **12**(3): p. 249-264.

111. Davis, R., *The effective thermal conductivity of a composite material with spherical inclusions.* International Journal of Thermophysics, 1986. **7**(3): p. 609-620.

112. Sangani, A. and C. Yao, *Bulk thermal conductivity of composites with spherical inclusions.* Journal of Applied Physics, 1988. **63**(5): p. 1334-1341.

113. Verma, L., et al., *Thermal conduction in two-phase materials with spherical and non-spherical inclusions.* Journal of Physics D: Applied Physics, 1991. **24**(10): p. 1729-1737.

114. Klemens, P., *Thermal conductivity of composites.* International Journal of Thermophysics, 1990. **11**(5): p. 971-976.

115. Andrianov, I.V., A.L. Kalamkarov, and G.A. Starushenko, *Analytical expressions for effective thermal conductivity of composite materials with inclusions of square cross-section.* Composites Part B: Engineering, 2013. **50**: p. 44-53.

116. Yu, J., et al., *Micromechanically-based effective thermal conductivity estimates for polymer nanocomposites.* Composites Part B: Engineering, 2013. **53**: p. 267-273.

117. Benveniste, Y. and T. Miloh, *The effective conductivity of composites with imperfect thermal contact at constituent interfaces.* International Journal of Engineering Science, 1986. **24**(9): p. 1537-1552.

118. Hasselman, D. and L.F. Johnson, *Effective thermal conductivity of composites with interfacial thermal barrier resistance.* Journal of Composite Materials, 1987. **21**(6): p. 508-515.

119. Böhm, H.J., A. Eckschlager, and W. Han, *Multi-inclusion unit cell models for metal matrix composites with randomly oriented discontinuous reinforcements.* Computational Materials Science, 2002. **25**(1): p. 42-53.

120. Segurado, J. and J. Llorca, *A numerical approximation to the elastic properties of sphere-reinforced composites.* Journal of the Mechanics and Physics of Solids, 2002. **50**(10): p. 2107-2121.

121. González, C., J. Segurado, and J. LLorca, *Numerical simulation of elasto-plastic deformation of composites: evolution of stress microfields and implications for homogenization models.* Journal of the Mechanics and Physics of Solids, 2004. **52**(7): p. 1573-1593.

122. Lévesque, M., et al., *A micromechanical model for nonlinear viscoelastic particle reinforced polymeric composite materials—undamaged state.* Composites Part A: Applied Science and Manufacturing, 2004. **35**(7): p. 905-913.

123. Bakshi, S.R., R.R. Patel, and A. Agarwal, *Thermal conductivity of carbon nanotube reinforced aluminum composites: a multi-scale study using object oriented finite element method.* Computational Materials Science, 2010. **50**(2): p. 419-428.

124. Chawla, N., et al., *Microstructure-based simulation of thermomechanical behavior of composite materials by object-oriented finite element analysis.* Materials Characterization, 2002. **49**(5): p. 395-407.

125. Langer, S.A., E.R. Fuller Jr, and W.C. Carter, *OOF: Image‐based finite‐element analysis of material microstructures.* Computing in Science & Engineering, 2001. **3**(3): p. 15-23.

126. Wang, Z., et al., *Effects of pores and interfaces on effective properties of plasma sprayed zirconia coatings.* Acta Materialia, 2003. **51**(18): p. 5319-5334.

127. Gudlur, P., A. Muliana, and M. Radovic, *The effect of microstructural morphology on the elastic, inelastic, and degradation behaviors of aluminum–alumina composites.* Mechanics Research Communications, 2014. **57**: p. 49-56.

128. Gudlur, P., A. Muliana, and M. Radovic, *Effective thermo-mechanical properties of aluminum–alumina composites using numerical approach.* Composites Part B: Engineering, 2014. **58**: p. 534-543.

129. Gudlur, P., et al., *On characterizing the mechanical properties of aluminum–alumina composites.* Materials Science and Engineering: A, 2014. **590**: p. 352-359.

130. Haj-Ali, R.M. and A.H. Muliana, *A multi-scale constitutive formulation for the nonlinear viscoelastic analysis of laminated composite materials and structures.* International Journal of Solids and Structures, 2004. **41**(13): p. 3461-3490.

131. Muliana, A.H. and J.S. Kim, *A concurrent micromechanical model for predicting nonlinear viscoelastic responses of composites reinforced with solid spherical*

particles. International Journal of Solids and Structures, 2007. **44**(21): p. 6891-6913.

132. Khan, K.A. and A.H. Muliana, *A multi-scale model for coupled heat conduction and deformations of viscoelastic functionally graded materials.* Composites Part B: Engineering, 2009. **40**(6): p. 511-521.

133. Khan, K.A. and A.H. Muliana, *Effective thermal properties of viscoelastic composites having field-dependent constituent properties.* Acta Mechanica, 2010. **209**(1-2): p. 153-178.

134. Khan, K.A., et al., *Coupled heat conduction and thermal stress analyses in particulate composites.* Mechanics of Materials, 2011. **43**(10): p. 608-625.

135. Agari, Y. and T. Uno, *Thermal conductivity of polymer filled with carbon materials: effect of conductive particle chains on thermal conductivity.* Journal of Applied Polymer Science, 1985. **30**(5): p. 2225-2235.

136. Agari, Y. and T. Uno, *Estimation on thermal conductivities of filled polymers.* Journal of Applied Polymer Science, 1986. **32**(7): p. 5705-5712.

137. Zhang, H., X. Ge, and H. Ye, *Effectiveness of the heat conduction reinforcement of particle filled composites.* Modelling and Simulation in Materials Science and Engineering, 2005. **13**(3): p. 401-412.

138. Zhou, H., S. Zhang, and M. Yang, *The effect of heat-transfer passages on the effective thermal conductivity of high filler loading composite materials.* Composites Science and Technology, 2007. **67**(6): p. 1035-1040.

139. Torquato, S., *Random heterogeneous materials: microstructure and macroscopic properties*. Vol. 16. 2013: Springer Science & Business Media.

140. Rao, Y., et al., *A precise numerical prediction of effective dielectric constant for polymer-ceramic composite based on effective-medium theory.* IEEE Transactions on Components and Packaging Technologies, 2000. **23**(4): p. 680-683.

141. Bergman, D.J. and K.-J. Dunn, *Bulk effective dielectric constant of a composite with a periodic microgeometry.* Physical Review B, 1992. **45**(23): p. 13262-13271.

142. Subbarao, E., M. McQuarrie, and W. Buessem, *Domain effects in polycrystalline barium titanate.* Journal of Applied Physics, 1957. **28**(10): p. 1194-1200.

143. Munoz-Saldana, J., G. Schneider, and L. Eng, *Stress induced movement of ferroelastic domain walls in BaTiO 3 single crystals evaluated by scanning force microscopy.* Surface Science, 2001. **480**(1): p. L402-L410.

144. Calderon-Moreno, J.M., *Stress induced domain switching of PZT in compression tests.* Materials Science and Engineering: A, 2001. **315**(1): p. 227-230.

145. Fett, T., et al., *Nonsymmetry in the deformation behaviour of PZT.* Journal of Materials Science Letters, 1998. **17**(4): p. 261-265.

146. Fett, T., D. Munz, and G. Thun, *Nonsymmetric deformation behavior of lead zirconate titanate determined in bending tests.* Journal of the American Ceramic Society, 1998. **81**(1): p. 269-272.

147. Moreno, J.C., et al., *Anisotropic and cyclic mechanical properties of piezoelectrics—compression testing.* Journal of the European Ceramic Society, 1999. **19**(6): p. 1321-1324.

148. Fröhlich, A., *Mikromechanisches modell zur ermittlung effektiver materialeigenschaften von piezoelektrischen polykristallen*. 2001: Forschungszentrum Karlsruhe.

149. Cao, H. and A.G. Evans, *Nonlinear deformation of ferroelectric ceramics.* Journal of the American Ceramic Society, 1993. **76**(4): p. 890-896.

150. Bassiouny, E., A. Ghaleb, and G. Maugin, *Thermodynamical formulation for coupled electromechanical hysteresis effects—I. Basic equations.* International Journal of Engineering Science, 1988. **26**(12): p. 1279-1295.

151. Bassiouny, E., A. Ghaleb, and G. Maugin, *Thermodynamical formulation for coupled electromechanical hysteresis effects—II. Poling of ceramics.* International Journal of Engineering Science, 1988. **26**(12): p. 1297-1306.

152. Bassiouny, E. and G. Maugin, *Thermodynamical formulation for coupled electromechanical hysteresis effects—III. Parameter identification.* International Journal of Engineering Science, 1989. **27**(8): p. 975-987.

153. Bassiouny, E. and G. Maugin, *Thermodynamical formulation for coupled electromechanical hysteresis effects—IV. Combined electromechanical loading.* International Journal of Engineering Science, 1989. **27**(8): p. 989-1000.

154. Landis, C.M., *Fully coupled, multi-axial, symmetric constitutive laws for polycrystalline ferroelectric ceramics.* Journal of the Mechanics and Physics of Solids, 2002. **50**(1): p. 127-152.

155. McMeeking, R.M. and C.M. Landis, *A phenomenological multi-axial constitutive law for switching in polycrystalline ferroelectric ceramics.* International Journal of Engineering Science, 2002. **40**(14): p. 1553-1577.

156. Kamlah, M. and C. Tsakmakis, *Phenomenological modeling of the non-linear electro-mechanical coupling in ferroelectrics.* International Journal of Solids and Structures, 1999. **36**(5): p. 669-695.

157. Lu, W., et al., *Nonlinear electric–mechanical behavior and micromechanics modelling of ferroelectric domain evolution.* Acta Materialia, 1999. **47**(10): p. 2913-2926.

158. Huber, J., et al., *A constitutive model for ferroelectric polycrystals.* Journal of the Mechanics and Physics of Solids, 1999. **47**(8): p. 1663-1697.

159. Hughes, D.C. and J.T. Wen. *Preisach modeling and compensation for smart material hysteresis*. In *Symposium on Active Materials and Smart Structures: Society of Engineering Science 31st Annual Meeting*. International Society for Optics and Photonics, 1995. p. 50-64.

160. Robert, G., et al., *Preisach modeling of piezoelectric nonlinearity in ferroelectric ceramics.* Journal of Applied Physics, 2001. **89**(9): p. 5067-5074.

161. Smith, R.C., et al. *A unified model for hysteresis in ferroic materials*. In *Smart Structures and Materials*. International Society for Optics and Photonics, 2003. p. 88-99.

162. Wang, F., et al., *BaTiO 3–polyethersulfone nanocomposites with high dielectric constant and excellent thermal stability.* Composites Part B: Engineering, 2011. **42**(1): p. 87-91.

163. Goyal, R., S. Katkade, and D. Mule, *Dielectric, mechanical and thermal properties of polymer/BaTiO 3 composites for embedded capacitor.* Composites Part B: Engineering, 2013. **44**(1): p. 128-132.

164. Setter, N. and R. Waser, *Electroceramic materials.* Acta Materialia, 2000. **48**(1): p. 151-178.

165. ASTM E831-14, *Standard test method for linear thermal expansion of solid materials by thermomechanical analysis.* ASTM International, West Conshohocken, PA, 2014.

166. ASTM E1269-11, *Standard test method for determining specific heat capacity by differential scanning calorimetry.* ASTM International, West Conshohocken, PA, 2011.

167. Gustafsson, S.E., *Transient plane source techniques for thermal conductivity and thermal diffusivity measurements of solid materials.* Review of Scientific Instruments, 1991. **62**(3): p. 797-804.

168. He, Y., *Rapid thermal conductivity measurement with a hot disk sensor: Part 1. Theoretical considerations.* Thermochimica Acta, 2005. **436**(1): p. 122-129.

169. Gustafsson, S.E., E. Karawacki, and M.A. Chohan, *Thermal transport studies of electrically conducting materials using the transient hot-strip technique.* Journal of Physics D: Applied Physics, 1986. **19**(5): p. 727-735.

170. Touloukian, Y. and E. Buyco, *Thermophysical properties of matter-the TPRC data series. Volume 5. Specific heat-nonmetallic solids*. 1970, DTIC Document.

171. Böhm, H.J. and W. Han, *Comparisons between three-dimensional and two-dimensional multi-particle unit cell models for particle reinforced metal matrix composites.* Modelling and Simulation in Materials Science and Engineering, 2001. **9**(2): p. 47-65.

172. Eberly, D., *Intersection of convex objects: The method of separating axes.* www. magic-software. com, 2001.

173. Nguyen, V.-D., et al., *Imposing periodic boundary condition on arbitrary meshes by polynomial interpolation.* Computational Materials Science, 2012. **55**: p. 390-406.

174. Jiang, M., I. Jasiuk, and M. Ostoja-Starzewski, *Apparent thermal conductivity of periodic two-dimensional composites.* Computational Materials Science, 2002. **25**(3): p. 329-338.

175. Andrews, J.P., *The variation of Young's Modulus at high temperatures.* Proceedings of the Physical Society of London, 1924. **37**(1): p. 169-177.

176. Powell, R., C.Y. Ho, and P.E. Liley, *Thermal conductivity of selected materials*. 1966, DTIC Document.

177. Ross, R.B., *Metallic materials specification handbook*. 2013: Springer Science & Business Media.

178. Cheng, B., et al., *Mechanical loss and Young's modulus associated with phase transitions in barium titanate based ceramics.* Journal of Materials Science, 1996. **31**(18): p. 4951-4955.

179. Price, C., *On the creep behavior of silver—I. The oxygen free metal.* Acta Metallurgica, 1966. **14**(12): p. 1781-1786.

180. Fletcher, L., *Recent developments in contact conductance heat transfer.* Journal of Heat Transfer, 1988. **110**(4b): p. 1059-1070.

181. Bohac, V., et al., *Parameter estimations for measurements of thermal transport properties with the hot disk thermal constants analyzer.* Review of Scientific Instruments, 2000. **71**(6): p. 2452-2455.

182. Xing, J., M. Radovic, and A. Muliana, *Thermal properties of BaTiO 3/Ag composites at different temperatures.* Composites Part B: Engineering, 2016. **90**: p. 287-301.

183. Carslaw, H.S. and J.C. Jaeger, *Conduction of heat in solids.* Oxford: Clarendon Press, 1959, 2nd ed., 1959.

184. Weigand, B., *Analytical methods for heat transfer and fluid flow problems*. Vol. 263. 2004: Springer.

185. Nocedal, J. and S. Wright, *Numerical optimization*. 2006: Springer Science & Business Media.

186. Baldick, R., *Applied optimization: formulation and algorithms for engineering systems*. 2006: Cambridge University Press.

187. Gudlur, P., et al., *Thermal and mechanical properties of Al/Al< sub> 2</sub> O< sub> 3</sub> composites at elevated temperatures.* Materials Science and Engineering: A, 2012. **531**: p. 18-27.

188. Flynn, K. and M. Radovic, *Evaluation of defects in materials using resonant ultrasound spectroscopy.* Journal of Materials Science, 2011. **46**(8): p. 2548-2556.

189. Marutake, M., *A calculation of physical constants of ceramic barium titanate.* Journal of the Physical Society of Japan, 1956. **11**(8): p. 807-814.

190. Roberts, S., *Dielectric and piezoelectric properties of barium titanate.* Physical Review, 1947. **71**(12): p. 890.

191. Sharer, T., *The designer's guide to Tungsten Carbide*. 2012.

192. Rajagopal, K. and A. Srinivasa, *On the thermomechanics of shape memory wires.* Zeitschrift für angewandte Mathematik und Physik ZAMP, 1999. **50**(3): p. 459-496.

193. Rajagopal, K. and A. Srinivasa, *Modeling anisotropic fluids within the framework of bodies with multiple natural configurations.* Journal of Non-Newtonian Fluid Mechanics, 2001. **99**(2): p. 109-124.

194. Doraiswamy, S., A. Rao, and A. Srinivasa, *Combining thermodynamic principles with preisach models for superelastic shape memory alloy wires.* Smart Materials and Structures, 2011. **20**(8): p. 085032.

195. Fechner, M., S. Ostanin, and I. Mertig, *Effect of the surface polarization in polar perovskites studied from first principles.* Physical Review B, 2008. **77**(9): p. 094112 1-4.

196. Mayergoyz, I.D., *Mathematical models of hysteresis and their applications*. 2003: Academic Press.

197. Smith, R.C., *Smart material systems: model development*. Vol. 32. 2005: SIAM.

198. Grant, M., Boyd, S. and Cvx, Y.Y., *Matlab software for disciplined convex programming, version 1.0 beta 3*. Recent Advances in Learning and Control, 2006. p.95-110.